Coordination Chemistry Reviews 438 (2021) 213906

Contents lists available at ScienceDirect

Coordination Chemistry Reviews

journal homepage: www.elsevier.com/locate/ccr

Review

Recent progress and perspectives in heterogeneous photocatalytic CO_2 reduction through a solid–gas mode

Hai-Ning Wang [a,b], Yan-Hong Zou [b], Hong-Xu Sun [b], Yifa Chen [a,*], Shun-Li Li [a,*], Ya-Qian Lan [a,*]

[a] Jiangsu Collaborative Innovation Centre of Biomedical Functional Materials, Jiangsu Key Laboratory of New Power Batteries, College of Chemistry and Materials Science, Nanjing Normal University, Nanjing 210023, PR China
[b] School of Chemistry and Chemical Engineering, Shandong University of Technology, Zibo, Shandong 255049, PR China

ARTICLE INFO

Article history:
Received 24 January 2021
Accepted 6 March 2021
Available online 24 March 2021

Keywords:
Photocatalysts
CO_2
Solid–gas mode
Photocatalytic mechanism

ABSTRACT

The conversion of CO_2 into valuable chemical feedstock through photocatalysis is considered as an effective strategy to mitigate global warming and energy-supply problems. The key challenge in CO_2 photoreduction is to design and synthesize powerful photocatalysts with superior advantages in absorbing visible-light, CO_2 enrichment/activation, and electron-coupled proton transition ability to facilitate the photoreduction process. During the past decades, various kinds of photocatalysts have been designed and explored for CO_2 photoreduction, and more and more achievements about CO_2 photoreduction have been made. However, the exploration of CO_2 photoreduction in the solid–gas mode is still in its infancy and the performance of reported photocatalysts are far from meeting the demand of practical applications. This review will summarize the reported literatures about CO_2 photoreduction via the solid–gas mode including the summary of their performances, reaction conditions and mechanistic pathway, etc. Besides, multiple strategies like experimental evidences and theoretical studies reported for the enhancement of CO_2 photoreduction performance have also been outlined and discussed. Moreover, we have proposed a brief perspective on the challenges about further development of CO_2 photoreduction in the solid–gas mode and hope to provide new insights for scientists in this field.

Contents

* Corresponding authors.
E-mail addresses: chyf927821@163.com (Y. Chen), slli@njnu.edu.cn (S.-L. Li), yqlan@njnu.edu.cn (Y.-Q. Lan).

https://doi.org/10.1016/j.ccr.2021.213906
0010-8545/

1. Introduction

The excessive release of CO_2, resulting from human activities involving combustion of fossil fuels for electricity, heat and transportation, has led to exponential elevation of CO_2 concentration [1]. As a kind of greenhouse gas, CO_2 could cause global warming coupling with abnormal climate, ocean storms and increased desertification area, etc. [2]. Reducing the emission and rational utilization of CO_2 become the main guiding ideology to address the environmental problems. To this end, two main strategies have been proposed to solve these problems: i) reducing the consumption of fossil fuels and replacing them with new energy sources, for example, solar and biomass [3]; ii) converting CO_2 into useful chemical materials.[4,5] Although humans consciously increase the practical proportion of new energy sources (e.g., wind or solar energy, etc.) applicable in social production or life consumption, fossil fuels will still be the main source of energy for the next few decades. In contrast, converting CO_2 into valuable chemicals has thus far been regarded as the most promising way and various strategies such as elctroreduction/photoreduction of CO_2 [6–11], chemical fixation of CO_2 [12] and metal-CO_2 batteries [13] have been proposed. Among them, photoreduction of CO_2, as an elegant solution for photoreduction of CO_2 into fuels (e.g., CO and hydrocarbons, etc.) and utilization of clean solar energy, has evoked an immerse of interest around the world and many endeavors have been made [1,2,14,15]. However, significant hurdles regarding energy efficiency, reaction selectivity, and higher value products (e.g., C_{2+} products) and overall conversion rate need to be overcome if CO_2 photoreduction is to become a viable option for solar energy storage and simultaneous CO_2 utilization. Despite these ongoing challenges of CO_2 photoreduction, recent advances in this field offer untapped potential for the realization of CO_2 transformation and relative progress especially for the reactions in solid–gas mode will be discussed below.

During past decades, the development of photocatalysts has seen great progress. Since 1972, titanium dioxide (TiO_2) has been firstly employed as a photocatalyst [16]. TiO_2 has been extensively studied owing to its following advantages: low cost, high chemical stability and ease of scalable synthesis, etc. Then, a variety of new photocatalysts has been synthesized and investigated [17–45]. Generally, an ideal photocatalyst should possess the following features: i) efficient electrons transfer from photocatalyst to reactive substrates; ii) appropriate conduction band (CB) and valence band (VB) in efficient light absorbance; iii) high efficiency in the adsorption and high-rate decomposition of reactive substrates (e.g., H_2O, CO_2 etc.) as well as desorption of product molecules. Unfortunately, most of reported photocatalysts are far from satisfying all of these requirements. Most of photocatalysts suffer from low visible light utilization efficiency and inefficient separation of photo-generated electrons-holes, for example, TiO_2 has inherent drawbacks like wide band gap that is only responsible for UV light and a high electron-hole pair recombination rate.

Guided by the above-mentioned features, various approaches, such as element doping, band heterojunction and combination with others semiconductors have been employed to overcome the shortcomings of photocatalysts. These approaches can be mainly classified into four kinds of strategies [46,47]: i) structure and morphology modification; ii) defect engineering; iii) elemental doping and iv) incorporation photocatalysts with other functional materials. Sometimes, it is difficult to adopt a single strategy to achieve the desired reduction efficiency, thus two or more strategies might be combined together to achieve desired reduction efficiency.

Until now, two types of pathways (homogeneous and heterogeneous process) have been developed by researchers to realize the photoreduction of CO_2 based on the form of photocatalysts. For the homogeneous process [48], some metal compounds like ruthenium or rhenium complexes are commonly used as the photocatalysts. The facing problems of this pathway may lie in the activity or stability of the photocatalysts and the efficient separation of products especially for the liquid ones. Compared with the homogeneous process, heterogeneous process might be more promising in the photoreduction of CO_2, where the reduction process of CO_2 directly occurs on the interface of heterogeneous photocatalysts. Various materials have been studied as heterogeneous photocatalysts, such as metal oxide (e.g., TiO_2 and ZnO, etc.), metal sulphide (e.g., CdS etc.), transition metal (e.g., Cu, Ni and Fe, etc.), noble metal (Pt and Au, etc.) or alloy (e.g., PtCu and AuCu, etc.) doped semiconductors and carbon based materials (C_3N_4 etc.), crystalline porous materials (MOFs etc.) etc.. Generally, the CO_2 photoreduction reaction can be achieved through the solid–liquid or solid–gas modes based on the substrates (Scheme 1). For the solid–liquid mode, the photocatalyst powder is distributed in the solution and high purity CO_2 gas is introduced into the system to generate saturate CO_2 solution. The reaction systems are commonly complicated, which contain various components like photocatalysts, solvent, photosensitizers (e.g., ruthenium or cobalt coordination complexes, etc.), co-photocatalysts and sacrificial agents (ascorbic acid, alcohols and amines etc.). Many types of solvents like H_2O, CH_3CN, CH_2Cl_2 and C_2H_7NO have been employed for CO_2 photoreduction. Among them, H_2O as the low cost and naturally abundant source is very suitable for the photocatalytic reduction of CO_2. Recently, the trend of researches has focused on employing water as the dispersant, and many outstanding achievements have been obtained. Until now, the majority of reported achievements prefer to employ the solid–liquid mode for CO_2 photoreduction [49–56]. However, there are some inevitable problems needed to be solved: i) the ground powder of photocatalysts needs to be dispersed in mixed reaction system full of CO_2 and the stability of photocatalysts in the catalysis system remains a challenge

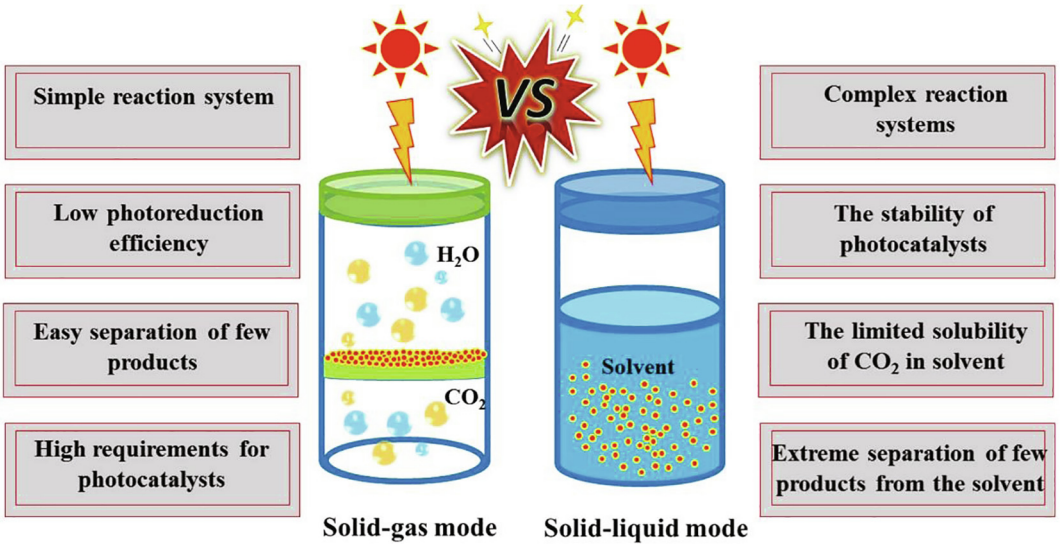

Scheme 1. The comparison of the solid–gas mode and solid–liquid mode.

especially that containing acidic or base sacrificial agents; ii) the limited solubility of CO_2 in the solvent or weak CO_2 adsorption ability might lead to low photocatalytic activity and iii) it is hard to separate very few products from the mixed system, especially liquid products. For these reasons, the appearence of the solid–gas mode may overcome these limitations, which may be more attractive for CO_2 photoreduction. For the solid–gas mode, photocatalysts particles evenly distribute on a matrix and a mixture of CO_2 and H_2O vapor are directly contact with them. Besides, the concentration of CO_2 can be adjusted freely and small amount of H_2O as the additive provides protons and electrons as sacrificial agents. There exist several factors that might possibly determine the performance of CO_2 photoreduction, which are listed below: i) the CO_2 adsorption ability, which is crucial to initiate the reaction of photocatalysis; ii) the morphology and particle size of photocatalysts, which determines the photocatalytic activity; iii) the energy band location, light absorption capacity and the transferring of photo-generated carriers. Commonly, the generation rate of H_2 is lower than that obtained through the solid–liquid mode owing to the exposed CO_2 atmosphere, which can avoid the formation of H_2. Naturally, the selectivity is higher. However, the photoreduction efficiency of the solid–gas mode reported is relative lower, which is far from meeting the practical industrial demand and still in its fancy due to that water is an extreme weaker reducing agent and CO_2 is harder to be activated. The summary and discussion of current materials in CO_2 photoreduction through the solid–gas mode are necessary to conclude the bottlenecks and challenges remained in this area, which might pose high promise in the development of CO_2 photoreduction to mitigate the CO_2 problem.

In this review, we will focus on discussing recent advances, in which photocatalyst reduce CO_2 in a gas–solid mode under light irradiation from 2016 to now. Up to now, various types of photocatalysts have been covered [57–212], such as metal oxide based photocatalysts, C_3N_4 based photocatalysts and MOFs dervied photocatalysts, and so on (Scheme 2). Furthermore, most of final products focus on CH_4 and CO irradiated by simulated light, and other products containing CH_3OH, C_2H_6, CH_3CHO, C_2H_5OH as well as HCOOH are rarely reported (Scheme 2). A basic summary of the achievements about photoreduction of CO_2 will be proposed (Table 1). Besides, the relationships between structure and activity will be provided in subsequent design and synthesis of photocatalysts. Moreover, a perspective towards opportunities, future development directions, and challenges for the photoreduction of CO_2 will be described in the last section.

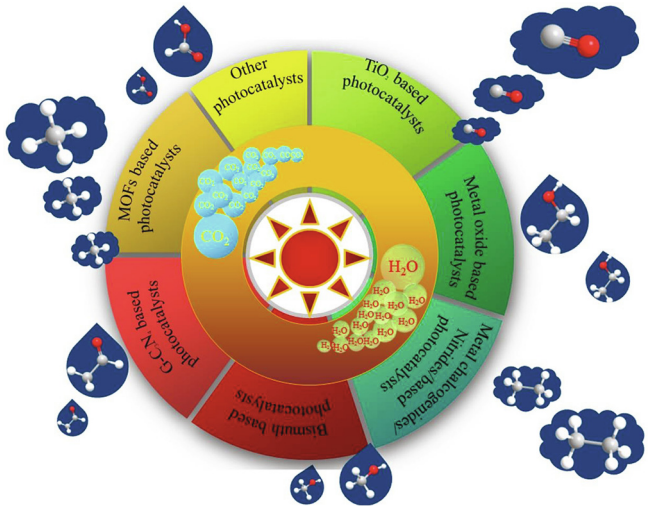

Scheme 2. Various kinds of photocatalysts and a variety of final products.

2. Fundamentals of photocatalytic CO_2 reduction

2.1. Basic principles of CO_2 photoreduction

CO_2 is a linear molecule, and exhibits thermodynamically stability due to the strong bond energy of C=O (750 kJ/mol), which makes the activation of CO_2 very difficult and more energy needs to be introduced to break C=O bonds in the process of photoreduction. Solar energy (1.3×10^5 TW) is an inexhaustible and clean energy source, and can be used to reduce CO_2 into valuable products. However, CO_2 possesses a high tolerance to either UV or visible light in the wavelengths of 200–900 nm. Therefore, photocatalysts with suitable band structures which prefer to transfer photo-generated electrons to CO_2 are needed to facilitate CO_2 conversion and complete the CO_2 reduction process.

Table 1
The list of various photocatalysts for CO_2 conversion with water vapor.

Number	Light source	photocatalyst	co-photocatalyst	condition	Main products	Refs.
1	A 400-W Hg lamp	Pd-Au/TiO_2-WO_3	Pd-Au	CO_2 flow passed through a saturator filledwith water at 308 ± 2 K	$CH_4$39.1 μmol g^{-1} h^{-1},CO 271.3 μmol g^{-1} h^{-1}	[57]
2	A 300 W Xe lamp λ = 320–780 nm	Pt_x/PC-TiO_2	Pt	mg, CO_2 and water vapor	CH_4 2.416 μmol	[58]
3	A 300 W Xe arc lamp without a filter	carbon@TiO_2		50 mg, CO_2 resulting from the reaction between HCl (0.25 mL, 4 M) and $NaHCO_3$ (0.12 g)	CH_4 4.2 μmol g^{-1} h^{-1}, CH_3OH 9.1 μmol g^{-1} h^{-1}	[59]
4	A xenon arc lamp with a UV cut-off filter	Graphene Oxide-Supported Oxygen-Rich TiO_2 5GO-OTiO_2		at ambient condition (298 ± 5 K, 1 bar)	CH_4 3.450 μmol g^{-1}	[60]
5	Two 20 W bulbs	Ag and Cu co-doped TiO_2 deposited on polyurethane (Ag@Cu-TiO_2/PU)	Ag and Cu	mg, CO_2 with a flow rate of 50 mL min^{-1} passing through water at 303 K	CH_4 880 μmol g^{-1}, CO 550 μmol g^{-1}	[61]
6	A 500 W Hg lamp	Cu-promoted In_2O_3/TiO_2	Cu	25 mg, mixture of gases (CO_2, He and H_2O) at 1.2 bar	CH_4 181 μmol g^{-1} h^{-1}, CO 12 μmol g^{-1} h^{-1}, CH_3OH 4 μmol g^{-1} h^{-1}	[62]
7	A 500 W Hg lamp	Ni-promoted In_2O_3/TiO_2	Ni	25 mg, CO_2 with different flow rates of 20, 20 and 60 mL min^{-1} and H_2	CH_4 240 μmol g^{-1} h^{-1}, CO 60 μmol g^{-1} h^{-1}	[62]
8	An Oriel Xe (Hg) 250 W lamp with an AM 1.5G filter	TiO_2/Ti_4O_9/Cu_2O		50 mg, 0.5 mL deionized water at 343 K and 0.69 bar	CH_3OH 2.93 μmol g^{-1} after 5 h	[63]
9	A 100 W Xenon solar simulator	Cu_xO-TiO_2		50 mg, A mixture fo CO_2 (1000 ppm in He) and H_2O vapors	CH_4 221.63 ppm $g^{-1}h^{-1}$	[64]
10	A 300w Xe lamp with 420 nm cut-off filter	C_5H_5-RuH complex bound to anatase (C_5H_5-RuH-O-TiO_2) hybrid		10 mg, CO_2 (101 kPa) and 20 μL water	CH_4 44 μL $g^{-1}h^{-1}$	[65]
11	A 8 W UV-C lamp	Cu-NPs loaded on TiO_2 NPs to form Cu/TiO_2	Cu	a thin layer of 250 mg, water saturated by CO_2 with three different flow rates at 298 K	CO 334 μmol g^{-1} h^{-1}	[66]
12	A Xenon solar simulator with an AM 1.5 filter	Cu_2ZnSnS_4 (CZTS)–TiO_2		50 mg, CO_2 gas (1000 ppm in He) passing through water, forming a mixture of CO_2 and H_2O vapors	CH_4 118.75 ppm $g^{-1}h^{-1}$	[67]
13	15-W energy-saving daylight bulbs	oxygen-rich TiO_2		CO_2 and water vapor at atmospheric pressure with a flow rate of 5 mL min^{-1}	CH_4 1.03 μmol g^{-1}	[68]
14	A 300 W Xe lamp	Mesoporous TiO_2		50 mg, CO_2 resulting from the reaction between H_2SO_4 (0.3 mL, 2 M) and $NaHCO_3$ (0.1 g)	CH_4 14.75 μmol g^{-1} h^{-1}	[69]
15	A 50 W LED lamp (maximum intensity around 510 nm)	flame annealed TiO_2 nanotube with an active area of 1 cm × 2 cm		a few drops of water and mixed gases (He and CO_2) with a flow rate of 25 mL min^{-1}	CH_4 156.5 μmol g^{-1} h^{-1}	[70]
16	Four UV lamps (6 W, λ max = 365 nm)	TiO_2-sputtered GF wafers		at 2 bar and 323 K a CO_2 and H_2O molar ratio of 7.25	C1 products (CO, CH_3OH, CH_4) 185.5 μmol g^{-1}	[71]
17	A 2 W LED (365 nm) light	P_{25}-TiO_2 film		6.5 mg	CH_4 2.227 μmol g^{-1} h^{-1}	[72]
18	A solar simulator	TiO_2-Au nanoparticle based aerogels	Au	TiO_2-Au aerogels with cylindrical shape (1.4 cm × 1.4 cm), humidified CO_2 with a flow rate of 5 mL min^{-1}	CH_3OH 2.58 μmol g^{-1} h^{-1}	[73]
19	A 100 W xenon solar simulator with an AM 1.5G filter	Pt-x-RT	Pt	70 mg, CO_2 (1000 ppm in He) passing through water forming a mixture of CO_2 and water vapor	CH_4 1.13 μmol g^{-1} h^{-1}	[74]
20	A 300-W Xe arc lamp	N-self-doped anatase TiO_2 (NT) microsheets	Ag and MnO_X nanoparticles	100 mg, CO_2 resulting from the reaction between HCl (0.3 mL, 4 M) and $NaHCO_3$ (0.12 g)	CH_3OH 0.53 μmol g^{-1} h^{-1}	[75]
21	A 300 W Xe arc lamp with a 400 nm cut-on filter attached in front of AM 1.5G filter	HN-TiO_2	Cu	HN-TiO_2 films, CO_2 and water vapor at 343 K	CO 12.67 μmol g^{-1}, CH_3OH 1.79 μmol g^{-1}	[76]

Table 1 (*continued*)

Number	Light source	photocatalyst	co-photocatalyst	condition	Main products	Refs.
22	A halogen lamp (300 W)	Ni-nanocluster loaded black TiO_2 (Ni/TiO_2[Vo])	Ni	100 mg, CO_2 with a flow rate of 4 sccm through water	CH_3CHO 10 μmol g^{-1}	[77]
23	A 300 W Xe-lamp	Cu-loaded brookite TiO_2	Cu	60 mg, CO_2 resulting from the reaction between H_2SO_4 (5 mL, 5 M) and $NaHCO_3$ (1.6 g)	CO 4.23 μmol g^{-1} h^{-1}, CH_4 17.81 μmol g^{-1} h^{-1}	[78]
24	A 300 W simulated solar Xe arc lamp	Cu-TiO_2	Cu	50 mg, CO_2 resulting from the reaction between H_2SO_4 (0.3 mL, 2 M) and $NaHCO_3$ (0.1 g)	CH_4 8.04 μmol g^{-1} h^{-1}	[79]
25	A pen-ray UV lamp	CuO/TiO_2		100 mg, 5 mL deionized water and H_2 gas (0.01 atm) at 363 K	CH_4 28.72 μmol g^{-1}	[80]
26	A 100 W mercury vapor lamp	Cu/TiO_2	Cu	40 mg, a CO_2 and H_2O gas mixture with a flow rate of 4.0 sccm	CO 7.5 μmol g^{-1} h^{-1} after 1.5 h	[81]
27	Two white light bulbs	Cu and V co-doped TiO_2 deposited on polyurethane (Cu@V-TiO_2/PU)	Cu and V	mg, CO_2 at a rate of 50 mL min^{-1} passing through water at 303 K	CH_4 933 μmol g^{-1} h^{-1}, CO 588 μmol g^{-1} h^{-1}	[82]
28	A UV-LED with the wavelength of 365 nm	Cu^{2+}-TiO_2 nanorod thin films	Cu^{2+}	TiO_2 nanorods thin film, H_2O and CO_2 with a ratio of 1:10 at 333 K	CH_3OH 36.18 μmol g^{-1} h^{-1} μmol g^{-1} h^{-1}, C_2H_5OH 79.13 μmol g^{-1} h^{-1}	[83]
29	A 300 W of Xenon-arc lamp	N-rich carbon quantum dots decorated two-phase TiONCQDs/P_{25}		50 mg, CO_2 and water vapor	CO 1.838 μmol, CH_4 1.195 μmol	[84]
30	A 450 W Xe lamp	Au/Al_2O_3/TiO_2	Au	10 mg, mixed CO_2 and H_2O vapor (2.3 vol% of H_2O) with a flow rate of 3 mL min^{-1}	CO about 40 μmol g^{-1}, CH_4 about 2 μmol g^{-1}	[85]
31	A 300 W xenon arc lamp	TiO_2 (OMT) composite	Au	mg, deionized H_2O (3 mL) and pure CO_2	CO 1.83 μmol g^{-1} h^{-1}, CH_4 0.33 μmol g^{-1} h^{-1}	[86]
32	A 100 W Xe solar simulator with an AM1.5 filter	blue-colored reduced titania	Pt	40 mg, moist CO_2 with a flow rate of 1 mL min^{-1}	CH_4 80.35 μmol g^{-1} h^{-1}	[87]
33	A 150-W mercury lamp	TiO_2	Pd	mg, H_2 and CO_2 in a ratio of 4:1 at 2.5 MPa	CH_4 355.62 μmol g^{-1}, CO 46.35 μmol g^{-1}, C_2H_6 39.69 μmol g^{-1}	[88]
34	Four 6 W lamps with a maximum wavelength at 365 nm	0.5Pt/TiO_2-COK-12	Pt	100 mg, CO_2:H_2O molar ratio of 7.25 at 2 bar and 323 K	CH_4/ CO/	[89]
35	Two LED lamps emitting monochromatic 365 nm and 530 nm light	Pt/TiO_2/Au@ SiO_2	Au@ SiO_2	32 mg, water saturated CO_2 gas at 780 Torr	CH_4 5.96 μmol g^{-1} in 2 h co-irradiation of 365 nm and 530 nm LED lamps	[90]
36	A 300 W Xe arc lamp with full spectrum (320–780 nm)	TiO_2 hollow microspheres	Au	30 mg, CO_2 resulting from the reaction between H_2 SO_4 solution (2 M, 0.3 mL) and $NaHCO_3$ (0.084 g)	CO 1 μmol g^{-1} h^{-1}, CH_4 6 μmol g^{-1} h^{-1} under AM 1.5 G irradiation, CO 2 μmol g^{-1} h^{-1}, CH_4 1.2 μmol g^{-1} h^{-1} under full spectrum light	[91]
37	A Xenon arc lamp	Cu on TiO_2 film grown in CO_2	Cu	metal/TiO_2 film saturated water vapor and CO_2	CH_4 32.0 μmol g^{-1} h^{-1}, CO 24.8 μmol g^{-1} h^{-1}	[92]
38	A Xenon arc lamp	TiO_2 film grown in CO_2	Pt	metal/TiO_2 film saturated water vapor and CO_2	CH_4 38.8 μmol g^{-1} h^{-1}	[92]
39	A 300 W Xe lamp with a 400 nm short-wave-pass cutoff filter	Pd_7Cu_1-TiO_2	Pd, Cu	5 mg of TiO_2 loaded with 0.01 mmol of metal atoms 1 mL water in a quartz tube and 0.2 MPa CO_2	CH_4 19.6 μmol g^{-1} h^{-1}	[93]

(*continued on next page*)

Table 1 (*continued*)

Number	Light source	photocatalyst	co-photocatalyst	condition	Main products	Refs.
40	A 300 W Xe lamp (I = 320–780 nm)	3DOM-TiO_2	Au, Pd	certain amount on a watch-glass with the basal diameter of 6.5 cm 2 mL water	CH_4 18.5 μmol g^{-1} h^{-1}, CO 1.2 μmol g^{-1} h^{-1}	[94]
41	A 300 W Xe lamp with wavelength of 320–780 nm	PtRu/TiO_2	PtRu	100 mg, CO_2 and distilled water with saturated vapor pressure at 30 °C	CH_4 38.7 μmol g^{-1} h^{-1}	[95]
42	1 kW high-pressure Hg (Xe) arc lamp with a water filter and a cut-off filter (λ > 305 nm)	Cu_2O/TiO_2 heterostructures		30 mg, 1 atm CO_2 saturated with water vapor	CO 2.11 μmol g^{-1} h^{-1}	[96]
43	A 300 W Xe lamp with a 200- to 1700-nm cutoff filter	TiO_2/ZnO		100 mg, 4 mL deionized water	CH_4 2.56 μmol g^{-1} h^{-1}	[97]
44	A 150 W UV lamp	TiO_{2-x}/CoO_X		50 mg, 1.33 bar CO_2 at 393 ± 5 K	CO 16.4 μmol g^{-1} h^{-1}, CH_4 10.1 μmol g^{-1} h^{-1}	[98]
45	A 350 W xenon lamp	TiO_2-MnO_x-Pt		nanosheets, CO_2 resulting from the reaction between H_2SO_4 solution (2 M, 0.3 mL) and $NaHCO_3$ (0.084 g)	CH_4 28 μmol m^{-2}, CH_3OH 31 μmol m^{-2} after 3 h	[99]
46	A 300 W Xenon lamp	CdS-Cu^{2+}/TiO_2		H_2O and CO_2 with a ratio of 1:10 and at 333 K	C_2H_5OH 109.12 μmol g^{-1} h^{-1}	[100]
47	A 300-W Xenon arc lamp	Z-Scheme TiO_2/CdS		4 cm^2 pieces CO_2 resulting from the reaction between HCl solution (0.3 mL, 4 M) and $NaHCO_3$ (0.084 g)	CH_4 11.9 μmol h^{-1} m^{-2}	[101]
48	A 350 W Xe arc lamp	TiO_2/$CuInS_2$ hybrid nanofibers		50 mg, CO_2 resulting from the reaction between H_2SO_4 solution (0.25 mL, 2 M) and $NaHCO_3$ (0.12 g)	CH_4 2.5 μmol g^{-1} h^{-1}, CH_3OH 0.86 μmol g^{-1} h^{-1}	[102]
49	A 350 W Xe arc lamp	carbon nanofibers@TiO_2		50 mg, CO_2 resulting from the reaction between HCl (0.25 mL, 4 M) and $NaHCO_3$ (0.12 g)	CH_4 13.52 μmol g^{-1} h^{-1}	[103]
50	A 300 W Xe lamp (320–780 nm)	(Pt/TiO_2)@rGO		certain amount photocatalysts on a watch-glass with 6.5 cm basal diameter deionized water (2 mL)	CH_4 41.3 μmol g^{-1} h^{-1}	[104]
51	A 100 W Xenon solar simulator	a reduced graphene oxide-TiO_2 nanoparticles (rGO-TiO_2 NP)		a 2.0 × 2.0 cm^2 film, a mixture of CO_2 and H_2O vapor	CH_4 5.67 ppm $cm^{-2}h^{-1}$	[105]
52	A 100 W solar Simulator with an AM 1.5 filter	Pt-sensitized graphene-wrapped defect-induced blue-coloured titania X-G/RBT		40 mg, moist CO_2 1 mL min^{-1}	C_2H_6 77 μmol g^{-1}, CH_4 259 μmol g^{-1}	[106]
53	A 300 W Xe lamp	TiO_2-graphene multiple-layered MoS_2		4 mL water	CO 92.33 μmol g^{-1} h^{-1}	[107]
54	A 400 W Xenon lamp with a UV cut-filter (λ > 400 nm)	TiO_2/nitrogen (N) doped reduced graphene oxide (TiO_2/NrGO)		10 mg, Mixed gases CO_2 and H_2O with a flow rate of 3.0 mL min^{-1}	CO 356.5 μmol g^{-1}	[108]
55	Lumen dynamics 200 W Hg lamp with wavelength at 320–390 nm	Pd 2%/TiO_2	Pd	250 mg, CO_2 and water vapor with a flow rate of 8 mL min^{-1}	CH_4 801.9 nmoles $g^{-1}h^{-1}$	[109]
56	Lumen dynamics 200 W Hg lamp with wavelength at 320–390 nm	Ag1%Pd1%/TiO_2	Ag, Pd	250 mg, CO_2 and water vapor with a flow rate of 8 mL min^{-1}	CH_4 1787 nmoles $g^{-1}h^{-1}$, C_2H_6 212 nmoles $g^{-1}h^{-1}$	[109]
57	Lumen dynamics 200 W Hg lamp with wavelength at 320–390 nm	Au2%/TiO_2	Au	250 mg, CO_2 and water vapor with a flow rate of 8 mL min^{-1}	CO 1153.171 nmoles $g^{-1}h^{-1}$, CH_4 131.205 nmoles $g^{-1}h^{-1}$	[109]
58	A 450 W Xe lamp (I = 320–780 nm)	ZnO_2-promoted ZnO		50 mg, a mixture of CO_2 and H_2O at 423 K	CH_4 47.4 μmol g^{-1}, CH_3OH 26.1 μmol g^{-1}	[110]
59	A 300 W Xe lamp	Ce doped $ZnFe_2O$	Ce	100 mg, 0.3 mL deionized water at 473 K	CO 1.7 μmol g^{-1} h^{-1}, CH_4 9.9 μmol g^{-1} h^{-1}	[111]

Table 1 (*continued*)

Number	Light source	photocatalyst	co-photocatalyst	condition	Main products	Refs.
60	Two 4 W 254 nm light	Two-dimensional (2D) SAPO-5 nanosheet		10 mg, CO_2 (1 bar) and 6 μL liquid water at 298 K	CH_4 8.96 μmol g^{-1} h^{-1}	[112]
61	A mercury lamp with a wavelength of 365 nm	basalt fiber (BF) core–shells coated $PbTiO_3$ (BF@TiO_2 and BF@$PbTiO_3$		200 mg, CO_2:H_2O with a ratio of 1:2 at 303 K and 1.0 atm	CH_4 290 μmol g^{-1} after 6 h	[113]
62	A 300 W full-spectrum Xe lamp	bimodal carbon modified ZnO		100 mg, CO_2 resulting from the reaction between H_2SO_4 solution (2 M, 0.3 mL) and $NaHCO_3$ (0.084 g)	CH_3OH 0.83 μmol g^{-1} h^{-1}	[114]
63	A 300 W high pressure xenon lamp	Au/BiOI/MnO_x	Au	100 mg, CO_2 resulting from the reaction between H_2SO_4 solution (4 M, 5 mL) and $NaHCO_3$ (1 g) To achieve 1 atm CO_2 gas.	CO 42.9 μmol g^{-1} h^{-1}, CH_4 1.36 μmol g^{-1} h^{-1}	[115]
64	A high-pressure mercury lamp (125 W)	porous ZnO nanosheets		50 mg, 0.5 mL deionized water at 473 K	CO 406.77 μmol g^{-1} h^{-1}, CH_4 20.16 μmol g^{-1} h^{-1}	[116]
65	A 350 W Xe lamp,	PDA-modified ZnO hierarchical microsphere		CO_2 resulting from the reaction between a small amount of H_2SO_4 and $NaHCO_3$ (0.05 g)	CH_4 < 0.3 μmol g^{-1} h^{-1}, CH_3OH < 1.0 μmol g^{-1} h^{-1}	[117]
66	A 500 W Xenon arc lamp	$ZnMn_2O_4$ flower-like microspheres		100 mg, 1 mL deionized water	CO 19.19 μmol	[118]
67	A 35 W HID Xe lamp	VO_2/ZnV_2O_4 microsphere		100 mg, CO_2 with a flow rate of 20 mL min^{-1} passing through water saturator	CO 378 μmol g^{-1} h^{-1}, CH_3OH 202 μmol g^{-1} h^{-1}	[119]
68	A 300 W Xe lamp	$SrCO_3$/HPJs		60 mg, CO_2 resulting from the reaction between H_2SO_4 solution (5.0 mL, (40%)) and $NaHCO_3$ (1.60 g)	CH_4 19.66 μmol g^{-1} h^{-1}, CO2.64 μmol g^{-1} h^{-1}	[120]
69	A 300 W Xe lamp (λ > 200 nm)	Ag doped layered perovskite $H_2SrTa_2O_7$ Ag/HST	Ag	300 mg powder with 2 cm × 1 cm area	CO 0.39 μmol g^{-1} h^{-1}	[121]
70	A 300 W Xe lamp (λ = 420–780 nm)	2D $SnNb_2O_6$ nanosheets		20 mg, CO_2 (1 bar) and 6 μL liquid water 298 K	CH_4 110.9 μL h^{-1} mol^{-1}	[122]
71	A 1000 W Hortilux Blue metal halide bulb	$In_2O_{3-x}(OH)_y$		20 mg, H_2 and CO_2 mixed gas at a total pressure of 2 atm at 423 K	CO 1.38 μmol g^{-1} h^{-1}	[123]
72	A 130 W Xe lamp	rhombohedral $In_2O_{3-x}(OH)_y$ nanocrystals		20 mg, CO_2 and H_2 with a ratio of 1: 3 (2 mL min^{-1} and 6 mL min^{-1})	CH_3OH 170 μmol g^{-1} h^{-1}, CO 1150 μmol g^{-1} h^{-1}	[124]
73	A 300 W xenon lamp with fitted IR blocking filter	NiMgGaAl		Thin film formed by 15 μL of 25 mg mL^{-1} aqueous solution on 1 cm by 1 cm glass, 54 μL of the deionized water	CO about 55 μmol g^{-1}	[125]
74	A 300 W Xe lamp	Layered zinc silicate grown on silica		5 mg powder	CO 126.7 μmol g^{-1} h^{-1}	[126]
75	A 300 W high pressure xenon lamp	MoO_{3-X} nanosheets		50 mg, 5 mL deionized water and 1 mL of CO_2	CO 10.3 μmol g^{-1} h^{-1}, CH_4 2.08 μmol g^{-1} h^{-1}	[127]
76	A 300 W Xenon arc lamp	$CoGeO_{2-x}(OH)_y$		100 mg, 0.4 mL deionized water	CH_4 6.65 μmol g^{-1} CO < 1.0 μmol g^{-1}	[128]
77	A 300 W Xe arc lamp with a UV-cutoff filter (λ > 420 nm)	N-doped graphene-functionalized $Zn_{1.231}Ge_{0.689}N_{1.218}O_{0.782}$N-graphene/ZnGEON		20 mg, 2 mL deionized water	CH_4 57 ppm $g^{-1}h^{-1}$	[129]
78	A 300 W Xe lamp	Cu_2O/graphene		mixed H_2 and CO_2 gas with a 4:1 M ratio at 1.3 bar	CH_4 14.93 μmol g^{-1} h^{-1}	[130]
79	A 300 W Xe lamp	NiO/Ni nanoparticles (NPs) supported on defective graphene (NiO/Ni-G)		40 mg, Mixed H_2 and CO_2 gas at 1.3 bar. and 473 K	CH_4 642 μmol g^{-1} h^{-1}	[131]
80	A 150 W Xe lamp with an AM1.5G and 420 nm optical filter	α-Fe_2O_3/Amine-RGO/ $CsPbBr_3$		CO_2 and saturated H_2O vapor	CH_4 469.16 μmol g^{-1}	[132]

(*continued on next page*)

Table 1 (*continued*)

Number	Light source	photocatalyst	co-photocatalyst	condition	Main products	Refs.
81	A Xe arc lamp (450 W)	SnO_2/eo-GO		20 mg, 0.05 mL water and CO_2 with a flow rate of 3 mL min^{-1}	CH_4 85 nmol $g^{-1}h^{-1}$	[133]
82	A 500 W Xe arc lamp ($\lambda > 400$ nm)	Rh(PD)-Au coloaded $SrTiO_3$		75 mg, 3 mL deionized water and CO_2 at about 70 kPa	CO 369.2 μmol g^{-1} h^{-1}	[134]
83	A 300-W Xe arc lamp	$Zn_2Ti_{1-x}Ge_xO_4$ ($0 < x < 0.15$)		50 mg, 20 μL deionized water and CO_2 (1 bar)	CO 11.9 μmol g^{-1} h^{-1}, CH_4 0.38 μmol g^{-1} h^{-1}	[135]
84	A 300 W xenonar clamp	Cu/CeO_{2-x}-0.1	Cu	50 mg	CO 8.25 μmol g^{-1}	[136]
85	visible-light	chromium doped CeO_2		100 mg	CO 16.2 μmol g^{-1}, CH_4 10.1 μmol g^{-1} under 8 h	[137]
86	A 300 W Xe arc lamp with 420 nm cut-off filters	single-atom silver-manganese photocatalysts (Ag-HMO)	Ag	100 mg	CH_4 0.61 mol mol^{-1}	[138]
87	A 300 W Xenon arc lamp	GaN:ZnO		0.4 mL deionized water	CH_4about 1.1 μmol g^{-1} in 10 h	[139]
88	Sunlight	CdS/Mn_2O_3 nanocomposites supported on porous anodic alumnia support		25 cm^2 photocatalyst film, CO_2 and H_2O vapor	C_2H_5OH 52.2 μmol g^{-1} h^{-1}, HCOOH 1392.3 μmol g^{-1} h^{-1}	[140]
89	A 300 W Xenon arc lamp with a cutoff filter ($\lambda > 420$ nm)	La_2O_3/$LaTiO_2N$		40 mg, 0.4 mL deionized water	CH_4 0.98 μmol g^{-1} h^{-1}	[141]
90	A 300 W xenon arc lamp with a cutoff filter ($\lambda > 420$ nm)	Ta_3N_5/$LaTiO_2N$		40 mg, deionized water (0.4 mL)	CH_4 2.32 μmol g^{-1}, CO 11.53 μmol g^{-1}	[142]
91	A 300 W Xenon arc lamp fitted with a cutoff filter ($\lambda > 420$ nm)	Ni/$LaTiO_2N$	Ni	40 mg	CH_4 49.69 μmol g^{-1}, CO 0.31 μmol g^{-1}	[143]
92	sunlight	RGO/CdS on porous anodic Alumina (PAA)/Aluminum Support		100 cm^2 photocatalyst film	CH_3OH 153.8 μmol g^{-1} h^{-1}	[144]
93	A 300 W Xe arc lamp	$Cu_2In_2ZnS_5$/Gd_2O_2S:Tb		100 mg, CO_2 resulting from the reaction between H_2SO_4 solution (5 mL aqueous solution) and $NaHCO_3$ (1 g)	CH_4 57.73 μmol g^{-1} h^{-1}	[145]
94	A 300 W Xe arc lamp (with a UV light cutoff filter ($\lambda \geq 420$ nm)	$Zn_XCa_{1-X}In_2S_4$		100 mg, CO_2 resulting from the reaction between H_2SO_4 (15 mL, 4 M) and $NaHCO_3$ (1.7 g)	CH_4 0.877 μmol g^{-1} h^{-1},CO 0.224 μmol g^{-1} h^{-1}	[146]
95	A 300 W Xe lamp with a standard AM 1.5 filter and a 420 nm cut-off filter	Partially Oxidized SnS_2		100 mg, 2 mL deionized water at 283 K	CO 12.28 μmol g^{-1} h^{-1}	[147]
96	A 100 W xenon solar simulator with an AM 1.5 filter	Cu_2ZnSnS_4 (CZTS)-ZnO		50 mg, CO_2 and water vapor	CH_4 138.90 ppm $g^{-1}h^{-1}$	[148]
97	A 300 W Xe lamp with a 420 nm cut-off filter	amine-functionalized graphene/CdS composite (AG/CdS)		50 mg, water (4 mL) at 313 K	CH_4 2.84 μmol g^{-1} h^{-1} at 1 bar and 1.62 μmol g^{-1} h^{-1} at 0.1 bar respectively	[149]
98	A 300 W Xe lamp	Z-scheme porous g-C_3N_4/Sn_2S_3-DETA		100 mg, CO_2 resulting from the reaction between HCl solution (0.5 mL, 4 M) and $NaHCO_3$ (0.12 g)	CH_4 4.84 μmol g^{-1} h^{-1}, CH_3OH 1.35 μmol g^{-1} h^{-1}	[150]
99	Two 20 W white bulbs with ultraviolet cutoff filters ($\lambda > 400$ nm)	V-doped Ta_3N_5 (V–Ta_3N_5)		100 mg, CO_2/H_2O vapor with the flow rate of 30 mL min^{-1} and the relative humidity of 60%	CH_4 425 μmol g^{-1} h^{-1}, CO 236 μmol g^{-1} h^{-1}	[151]
100	A 300 W Xenon arc lamp	Ta_3N_5/Bi		100 mg, 0.4 mL deionized water	CH_4 0.57 μmol g^{-1} h^{-1}	[152]
101	A PLS-SXE300 Xe lamp with a 420 nm cut-off filter	C-$Cu_{2-x}S$ Nanotube/g-C_3N_4		1 mg, 1 atm pressure CO_2 and 0.1 mL H_2O	CO 1062.6 μmol g^{-1}	[153]

Table 1 (*continued*)

Number	Light source	photocatalyst	co-photocatalyst	condition	Main products	Refs.
102	A 300 W Xe lamp	thiourea derived g-C_3N_4 (TCN)		40 mg, CO_2 with the flow rate of 3.0 mL min^{-1}	CO 10.50 μmol g^{-1}, CH_4 1.20 μmol g^{-1}	[154]
103	A 300 W Hg lamp	Mo-doped g-C_3N_4		100 mg, 5.0 g deionized water at 303 K and 110 KPa	CO 887 μmol g^{-1}, CH_4 123 μmol g^{-1} after 8 h	[155]
104	visible light	C_3N_4 nanosheets	Pd	a mixed gas of CO_2 and H_2O vapor	CO 4.3 μmol g^{-1} h^{-1}, CH_4 0.45 μmol g^{-1} h^{-1}	[156]
105	A Xe lamp	K-incorporated amino-rich carbon nitride, K-AUCN		20 mg, 20 mL deionized water at 298 K	CH_4 about 50 μmol g^{-1}, CO about 45 μmol g^{-1}	[157]
106	A 100 W Xe lamp	Oxygen Chemically Modified g-C_3N_4 Powder		8 mg powder on borosilicate glass, 1 mL water at 343 K 20% CO_2 in Ar at a pressure of 2.5 bar	CO/	[158]
107	A 300 W Xenon lamp with a 420 nm light cut filter	30-Bi-decorated g-C_3N_4		40 mg, CO_2 passing through water with a flow rate of 3 mL min^{-1}	CO 13.25 μmol g^{-1}, CH_4 1.03 μmol g^{-1},	[159]
108	A 350 W Xe lamp with a 420 nm cutoff filter	O-doped graphitic carbon nitride (g-C_3N_4) nanotubes (OCN-Tube)		50 mg, CO_2 resulting from the reaction between H_2SO_4 (0.25 mL, 2 M) and $NaHCO_3$ (0.12 g)	CH_3OH 0.88 μmol g^{-1} h^{-1}	[160]
109	A 300 W high pressure xenon lamp	Mesoporous phosphorylated g-C_3N_4 (MPCN)		200 mg MPCN, CO_2 resulting from the reaction between H_2SO_4 (5 mL, 4 M) and $NaHCO_3$ (1.0 g) to achieve 1 atm CO_2 gas at 283 K	CO 7.91 μmol, CH_4 15.6 μmol	[161]
110	A 300 W Xe lamp	NH_3-mediated thermal exfoliation of dicyandiamide-derived g-C_3N_4 NS-CN		100 mg of degassed nanosheets, CO_2 resulting from the reaction between H_2SO_4 (0.3 mL, 2 M) and $NaHCO_3$ (0.084 g)	CH_4 1.39 μmol g^{-1} h^{-1}, CH_3OH 1.87 μmol g^{-1} h^{-1}	[162]
111	A 300 W Xe lamp	g-C_3N_4 (Au-CN)	Au	50 mg, CO_2 passing through water with a flow rate of 3 mL min^{-1}	CO 13.17 μmol g^{-1}, CH_4 3.1 μmol g^{-1}	[163]
112	A 300 W Xe lamp	g-C_3N_4/Ag-TiO_2 (CN/AgTi)		50 mg, CO_2 with a flow rate of 3 mL min^{-1} passed through a water bubbler	CH_4 28 μmol g^{-1}, CO 19 μmol g^{-1} within 3 h	[164]
113	Two 30 W white bulbs	Nb doped TiO_2/g-C_3N_4		100 mg, CO_2 with a flow rate of 20 mL min^{-1} passing through water at 303 K	CH_4 562 μmol g^{-1} h^{-1}, CO 420 μmol g^{-1} h^{-1}, HCOOH 698 μmol g^{-1} h^{-1}	[165]
114	A 300 W Xe-lamp	Brookite TiO_2/g-C_3N_4 nanocomposites BTN-CNDs		60 mg, CO_2 resulting from the reaction between H_2SO_4 (5 mL, 4 M) and $NaHCO_3$ (1.5 g)	CO 0.84 μmol g^{-1}, CH_4 5.21 μmol g^{-1} under visible light, CO 1.27 μmol g^{-1}, CH_4 6.94 μmol g^{-1} under UV–vis light	[166]
115	A PLS-SXE300 Xe lamp with a 420 nm cutoff filter	C-TiO_{2-x}@g-C_3N_4		1 mg, 0.1 mL deionized water	CO 12.30 mmol g^{-1}	[167]
116	A 300 W Xenon-arc lamp	m-CeO_2/g-C_3N_4		50 mg on 1.5 cm × 1.5 cm a flat glass plate, a mixture of CO_2 and water vapor at 298 K	CO 0.590 μmol, CH_4 0.694 μmol	[168]
117	A 300 W Xenon-arc lamp	$LaPO_4$/g-C_3N_4		30 mg, a mixture gases of CO_2 and water vapor at 298 K	CO 0.433 μmol	[169]
118	A 300 W Xe lamp	MnO_2/g-C_3N_4		50 mg, CO_2 and water vapor at 298 K	CO 9.6 μmol g^{-1}	[170]

(*continued on next page*)

Table 1 (*continued*)

Number	Light source	photocatalyst	co-photocatalyst	condition	Main products	Refs.
119	A 300-W Xe arc lamp full spectrum light	Ag_2CrO_4/g-C_3N_4	graphene oxide	100 mg, CO_2 resulting from the reaction between HCl solution (0.25 mL, 4 M) and $NaHCO_3$ (0.12 g)	C1 products (CH_3OH and CH_4) 1.03 μmol g^{-1}	[171]
120	A 300 W Xe light with a cutoff filter (λ > 420 nm)	Z-scheme g-C $_3N_4$/SnS_2		50 mg, CO_2 resulting from the reaction between H_2SO_4 (0.3 mL, 2 M) and $NaHCO_3$ (0.084 g)	CH_3OH 2.3 μmol g^{-1}, CH_4 0.64 μmol g^{-1}	[172]
121	A Xe lamp with a 420 nm optical filter	Au@g-C_3N_4/SnS	Au	5.3 mg, 10 μL water with CO_2 to 1 bar	CH_4 3.8 μmol g^{-1}, CH_3OH 5.3 μmol g^{-1}, CO 17.1 μmol g^{-1}	[173]
122	A 300 W Xenon short arc lamp with UV/IR filters	Pt loaded Boron carbide/graphitic carbon nitride (B_4C/g-C_3N_4)	Pt	6 cm^2 multi-layer photocatalyst film (6 mg) at 295 K a mixed gas of 1 vol% CO_2, 4 vol% H_2, and 95 vol% Ar	CH_4 0.84 μmol g^{-1} h^{-1}	[174]
123	A 300 W Xe lamp	Pd-embedded g-C_3N_4/ reduced graphene oxide aerogel (Pd-g-C_3N_4/RGOA)	Pd	100 mg	CH_4 6.4 μmol g^{-1} h^{-1}	[175]
124	A Xe arc lamp (500 W)	graphitic carbon nitride and carbon (H-g-C_3N_4/C)		100 mg, at 110 KPa and 303 K	CO 22.60 μmol g^{-1}, CH_4 12.5 μmol g^{-1} under 9 h	[176]
125	A Xe arc lamp (500 W)	3D porous graphitic carbon nitride/carbon 3D g-C_3N_4/C-NS		mg, a mixture of CO_2 and H_2O at about 20 mL min^{-1} at 30 °C and 110 KPa	CO 229 μmol g^{-1}, CH_4 112 μmol g^{-1}	[177]
126	A xenon arc lamp with various filters (including a UV cut-off filter (λ > 400 nm)	carbon nanodot (CND)-hybridized protonated g-C_3N_4 (pCN) (CND/pCN)		50 mg, CO_2 with a flow rate of 5 mL min^{-1}	CH_4 29.23 μmol g^{-1}, CO 58.82 μmol g^{-1} under visible light, CH_4 37.06 μmol g^{-1}, CO 68.80 μmol g^{-1} under simulated solar light	[178]
127	A 300 W Xenon-arc lamp (λ > 400 nm)	CQDs/g-C_3N_4		20 mg, a mixture of CO_2 saturated with water vapor	CO 23.38 μmol g^{-1} h^{-1}, CH_4 20.78 μmol g^{-1} h^{-1}	[179]
128	A medium – high mercury vapor pressure lamp with emittance from 360 nm (UV – vis) to 600	C_3N_4 embedded in a Nafion dense matrix flat sheet membrane		sheet membrane	Alcohol (MeOH + EtOH) 32.8 μmol g^{-1} h^{-1}	[180]
129	A 500 W xenon lamp with a 420 nm filter	a graphitic carbon nitride (g-C_3N_4) photocatalyst with transparent paper		100 mg, at 298 K and 110 KPa, a mixture of CO_2 (95.5%) and H_2O (4.5%)	CO about 4 μmol g^{-1}	[181]
130	A 300 W high pressure xenon lamp	$Bi_4O_5Br_2$		150 mg, CO_2 resulting from the reaction between H_2SO_4 (5 mL, 4 M) and $NaHCO_3$ (1.3 g) at 293 K	CO 2.73 μmol g^{-1} h^{-1}, CH_4 2.04 μmol g^{-1} h^{-1}	[182]
131	A 500 W Xenon arc lamp with an AM 1.5 filter and UV cut-off filter	(BiOBr) with oxygen-deficient defects		CO_2 and water vapor with a flow rate of 5 mL min^{-1}	CH_4 4.86 μmol g^{-1}	[183]
132	A 300 W high-pressure xenon lamp	$Bi_{24}O_{31}Cl_{10}$-OV		50 mg, 5 mL of distilled water and 1 mL CO_2	CO 0.9 μmol g^{-1} h^{-1}	[184]
133	A 300 W Xe lamp	$Sr_2Bi_2Nb_2TiO_{12}$ nanosheets		100 mg, CO_2 resulting from the reaction between H_2SO_4 solution (4 M, 5 mL) and $NaHCO_3$ (1.3 g) to get 1 atm CO 2 gas at 293 K	CO 17.11 μmol g^{-1} h^{-1}	[185]
134	A xenon lamp (PLS-SXE 300D)	BiOBr		10 mg CO_2 and 10 μL H_2O	CO 21.6 μmol g^{-1} h^{-1}, CH_4 1.2 μmol g^{-1} h^{-1}	[186]

Table 1 (*continued*)

Number	Light source	photocatalyst	co-photocatalyst	condition	Main products	Refs.
135	A 300 W Xenon arc lamp	BiOI/g-C_3N_4		100 mg, a mixture of CO_2 and H_2O vapor	CO 17.9 μmol g^{-1}, CH_4 < 1.5 μmol g^{-1}	[187]
136	A 300 W high pressure xenon lamp	g-C_3N_4/$Bi_4O_5I_2$		100 mg, CO_2 resulting from the reaction between H_2SO_4 (5 mL, 4 M) and $NaHCO_3$ to achieve 1 atm CO_2 gas at 288 K	CO 45.6 μmol g^{-1} h^{-1}	[188]
137	A 300 W xenon arc lamp with a UV cutoff filter (λ > 400 nm)	Z-scheme CdS/$BiVO_4$		20 mg, CO_2 at 0.3 MPa.	CH_4 8.73 μmol g^{-1}, CO 1.95 μmol g^{-1}	[189]
138	A 500-W xenon arc lamp with different cut-off filters	CQDs-decorated ultrathin Bi_2 WO_6 nanosheets (UBW)		as-synthesized samples coated on glass rods, CO_2/H_2O with a flow rate of 50 mL min^{-1}	CH_4 7.19 μmol g^{-1} under visible light (λ > 400 nm), CH_4 0.41 μmol g^{-1} under NIR light (λ > 700 nm)	[190]
139	A Xe lamp (300 W)	BON-X (X = Cl, Br, and I)		20 mg, CO_2 resulting from the reaction between H_2SO_4 solution (15 mL, 1.33 M) and $NaHCO_3$	CO 8.12 μmol g^{-1} h^{-1}	[191]
140	A 300 W Xe lamp with a UV-cut filter (420 nm)	$CsPbBr_3$ QDs/UiO-66(NH_2)		10 mg, at 278 K	CO 98.57 μmol g^{-1}	[192]
141	A 300 W high pressure mercury lamp	Zn/PMOF		300 mg, CO_2 at 20 psia of absolute total pressure, and 0.6 mL distilled water at 373 K	CH_4 10.43 μmol	[193]
142	A Xe lamp with a AM 1.5G filter	PCN-601		5 mg 80 kPa CO_2 and 3 mL water	CH_4 92 μmol g^{-1} h^{-1}	[194]
143	A 300 W full-spectrum Xe lamp	g-C_3N_4/ZIF-8		100 mg, CO_2 resulting from the reaction between H_2SO_4 (0.3 mL, 2 M) and $NaHCO_3$ (0.084 g)	CH_3OH 0.75 μmol g^{-1} h^{-1}	[195]
144	A 100 W Xe lamp with a AM 1.5G filter	$CsPbBr_3$@ZIF-67		films (mass of about 4.5 mg)	CH_4 29.630 μmol g^{-1} h^{-1}	[196]
145	A 300 W xenon arc lamp with a 400 nm short-wave-pass cut-off filter	$Cu_3(BTC)_2$ @TiO_2		300 mg, H_2O vapor resulting from 5 mL water at 313 K and CO_2	CH_4 2.64 μmol g^{-1} h^{-1}	[197]
146	A 450 W Xe lamp with an AM 1.5G filter	HKUST-1/TiO_2		CO_2/H_2O vapor mixture with a flow rate of 4 mL min^{-1}	CO 256.35 μmol g^{-1} h^{-1}	[198]
147	A 300 W xenon lamp	TiO_2/UiO-66		50 mg CO_2 and saturated water vapor	CH_4 17.9 μmol g^{-1} h^{-1}	[199]
148	The PLS-SXE300 Xe lamp	Bi_2S_3/UiO-66		40 mg humid CO_2 gas (5 vol% H_2O)	CO 25.6 μmol g^{-1} h^{-1}	[200]
149	A xenon lamp	g-C_3N_4/CuO@MIL-125(Ti)		1.0 MPa CO_2 and 1 mL H_2O	CO 180.1 μmol g^{-1}, CH_3OH 997.2 μmol g^{-1}, CH_3CHO 531.5 μmol g^{-1}, C_2H_5OH 1505.7 μmol g^{-1}	[201]
150	A 300 W Xe lamp with a 400 nm cut-off filter	Au@NENU-10		100 mg, water and CO_2 vapor at 313 K	CO 12.8 μmol g^{-1} h^{-1}, CH_4 2.1 μmol g^{-1} h^{-1}	[202]
151	Four 4 W UV lamps with a wavelength centered at 365 nm	CPO-27-Mg/TiO_2		10 mg, CO_2 atmosphere in the presence of saturated water vapor	CO 40.9 μmol g^{-1}, CH_4 23.5 μmol g^{-1}	[203]
152	A 200 W Hg/Xe (200–750 nm) lamp	gold/titania nano composites, GNP/TiO_2	gold	50 mg, 1.5% of CO_2 and 0.6% of H_2O in He at room temperature and a pressure of 1.1 to 1.5 bar	CH_4 about 60 ppm	[204]
153	A 450 W Xe lamp	ALD modified MgO/TiO		10 mg, a CO_2/H_2O gas mixture (water vapor concentration ≈ 2.3% by volume)	CO 54.0 μmol g^{-1}	[205]
154	A 300 W full-spectrum Xe lamp	ZnO/NiO porous hollow spheres		50 mg, CO_2 resulting from the reaction between H_2SO_4 (0.2 mL, 2 M) and $NaHCO_3$ (0.084 g)	CH_3OH 1.57 μmol g^{-1} h^{-1}	[206]
155	A 350 W Xe lamp	Carbon fibers (CFs) decorated with Ag nanoparticles (Ag NPs), hereafter denoted as Ag NPs/CFs,	Ag	10 mg, CO_2 with a flow rate of 20 mL min^{-1} and H_2O at 353 K	CH_3OH 0.475 μmol g^{-1} h^{-1}	[207]
156	A 300 W commercial Xe lamp	hollow spherical SiC	Pt	10 mg, atmospheric pressure at ambient temperature (298 K)	CH_4 16.8 μmol g^{-1} h^{-1}	[208]

(*continued on next page*)

Table 1 (*continued*)

Number	Light source	photocatalyst	co-photocatalyst	condition	Main products	Refs.
157	A 300 W Xe lamp	Boron carbide (B_4C)		10 mg	CO 1.71 μmol g^{-1} h^{-1}	[209]
158	A xenon lamp ($200 \leq \lambda \leq 1000$ nm)	TAPBB-COF		3 mg 1 mL water at 353 K	CO 24.6 μmol g^{-1} h^{-1}	[210]
159	A 300 W Xe lamp (λ = 380–800 nm)	COF-318-TiO_2		2 mg	CO 69.67 μmol g^{-1} h^{-1}	[211]
160	A 300 W high pressure xenon lamp (420 nm cut off)	CT-COF		50 mg 1 atm Ar with 1 mL CO_2 and 5 mL water	CO 102.7 μmol g^{-1} h^{-1}	[212]

In the CO_2 photoreduction process, the anchor of CO_2 on the surface of photocatalyst can lead to the change of CO_2 configuration from linear to bend with a lower LUMO level. Then one-electron transfer takes place, generating active $CO_2^{\cdot-}$ (redox potential of 1.85 V (versus NHE)). This process is very difficult to happen, but it can trigger a series of chemical reactions. Naturally, the relative reactions in CO_2 reduction process have been listed below:

$$CO_2 + e^- \rightarrow CO_2^{\cdot-} \quad E^0_{redox} = -1.85\ V \tag{1}$$

$$CO_2 + 2H^+ + 2e^- \rightarrow HCOOH \quad E^0_{redox} = -0.61\ V \tag{2}$$

$$CO_2 + 2H^+ + 2e^- \rightarrow CO + H_2O \quad E^0_{redox} = -0.53\ V \tag{3}$$

$$CO_2 + 4H^+ + 4e^- \rightarrow HCHO + H_2O \quad E^0_{redox} = -0.48\ V \tag{4}$$

$$CO_2 + 4H^+ + 4e^- \rightarrow C + 2H_2O \quad E^0_{redox} = -0.20\ V \tag{5}$$

$$CO_2 + 6H^+ + 6e^- \rightarrow CH_3OH + H_2O \quad E^0_{redox} = -0.38\ V \tag{6}$$

$$CO_2 + 8H^+ + 8e^- \rightarrow CH_4 + 2H_2O \quad E^0_{redox} = -0.24\ V \tag{7}$$

$$2CO_2 + 12H^+ + 12e^- \rightarrow C_2H_4 + 4H_2O \quad E^0_{redox} = -0.34\ V \tag{8}$$

$$2CO_2 + 12H^+ + 12e^- \rightarrow C_2H_5OH + 3H_2O \quad E^0_{redox} = -0.33\ V \tag{9}$$

$$2CO_2 + 14H^+ + 2e^- \rightarrow C_2H_6 + 4H_2O \quad E^0_{redox} = -0.27\ V \tag{10}$$

$$3CO_2 + 11H^+ + 18e^- \rightarrow C_3H_7OH + 5H_2O \quad E^0_{redox} = -0.32\ V \tag{11}$$

$$2H^+ + 2e^- \rightarrow H_2 \quad E^0_{redox} = -0.42\ V \tag{12}$$

2.2. Oxidation half-reactions

Most of researchers focus on the investigation of reduction reactions in the CO_2 photoconversion process, leading to oxidation reaction hardly attracts researcher's interest. Photoreduction of CO_2 in the solid–liquid and solid–gas mode are different in some aspects. Generally speaking, in solid–liquid mode, sacrificial agent, such as, organic amines and alcohols are oxidized by photo-generated holes (h^+) to accomplish this process. While, in solid–gas mode, holes (h^+) on the surface can react with adsorbed water, leading to the generation of O_2 or hydroxyl radicals **·**OH [Eqs. (13) and (14); potentials versus NHE at pH = 7.

$$H_2O + 4h^+ \rightarrow O_2 + 4H^+ \quad E^0_{redox} = 0.81\ V \tag{13}$$

$$H_2O + h^+ \rightarrow \cdot OH + H^+ \quad E^0_{redox} = 2.32\ V \tag{14}$$

The oxidation of water is feasible, because the potential of water oxidation is more negative than valence bands of most photocatalysts from a thermodynamic point of view.

2.3. Possible reaction pathways of CO_2 reduction

CO_2 reduction process is a complicated and multi-step process, which includes transferring abundant electrons and protons, destroying C═O bonds and creating C─H bonds. The completion of the whole reduction process may require the participation of several radical intermediates, which involves in different stages. Varied experimental conditions would lead to different products. Additionally, various radical intermediates make CO_2 reduction process more complicated. A number of factors, such as light, photocatalyst, etc. also influence the final products remarkably.

Many reported mechanisms reveal that there exist several competitive pathways to produce the final identical products from generated $CO_2^{\cdot-}$ radicals, but more importantly, the reduction of water is a competitive reaction in CO_2 reduction process. When H_2O is introduced in the process of photoreduction CO_2, it provides protons, and acts as electron donors. Its oxidation will generate protons and O_2 as well as electrons. The reduction of water ($2H^+ + 2e^- \rightarrow H_2$) is easy to happen, because this reduction requires only two electrons. Naturally, the photo-generated electrons and H^+ are consumed by water reduction, which decrease the CO_2 reduction rate, ultimately affecting reduction efficiency. Therefore, the high selectivity and yield of products remain a challenge. According to the reported literatures, C_1 compounds (CO, CH_4 etc.) appear frequently, while $C_n \geq 2$ (more than two carbons) compounds usually occur as minor products.

Density functional theory (DFT) theoretical calculation has been considered as a very effective tool to investigate CO_2 photoreduction mechanisms. It is well known that DFT results can give the thermodynamic and kinetic properties of a photocatalyst. DFT calculation can deeply present the peak shift of optical absorption and electronic performance of a photocatalyst, reveal its band structure, and understand the possible reaction pathways determined by transient states of CO_2.

Direct experimental evidences of possible reaction pathways are supported by several analytical methods, which include electron paramagnetic resonance (EPR) and in-situ diffuse reflectance infrared Fourier transform spectroscopy (DRIFTS), etc. Both of them can accurately identify the generated intermediates during reaction process, assisting in confirming reaction pathway. However, some critical intermediates appearing in the photoreduction process cannot be detected and in-depth study of possible reduction mechanism puts forward higher requirements for operands and time-resolved characterization techniques used in these analytical

methods. Despite EPR and in-situ DRIFTS, other in-situ approaches (e.g., in-situ X-ray diffraction, in-situ Raman spectroscopy, in-situ angle resolved X-ray photoelectron spectroscopy and so on) are still in their exploratory stage and are potential measurements in the mechanism investigation of CO_2 photoreduction.

2.4. Confirmation of the product formation from CO_2

Carbon residues introduced through various routes will take part in the generation of primary products during the CO_2 photoreduction process and affect the overall product yield. For example, Frei etc. have found that carbon residues indeed influence the category and yield of final products in the photocatalytic CO_2 reduction. It is necessary to demonstrate that the generated products indeed result from CO_2 rather than carbon residues. To confirm it, isotope labeling ($^{13}CO_2$) combining with gas chromatography/mass spectrometry (GC–MS) should be conducted to detect the ^{13}C products. If ^{12}C products appear, the experimental results demonstrate the carbon residues resulting from the photocatalyst actually participate in the reduction process. Additionally, there is another method to check the actual reduction of CO_2. Under the same condition, contrast experiments performed under other gas (e.g., N_2 or Ar etc.) atmosphere coupling with blank experiment results can also prove the resource of products.

2.5. Performance evaluation of photocatalytic CO_2 reduction

Up to now, several experimental parameters, such as activity, long-term stability etc., have been proposed to evaluate the performance of various photocatalysts. Activity is usually evaluated by the formation rate of final products under designed experimental conditions and defined as $\mu mol\, g^{-1}$ (or $\mu mol\, g^{-1}\, h^{-1}$). However, the overall rates of products are closely related with experimental conditions such as light source, light intensity and so on. Therefore, it is not very meaningful that activity is used to evaluate the catalytic performance, because experimental conditions as well as product types are different. Considering the relationship of product formation rate and yield, the product yield extremely depends on experimental conditions. Therefore, it is better to use CO_2 reduction efficiency to evaluate the catalytic activity.

Apparent quantum efficiency (AQE) has been defined to evaluate CO_2 reduction efficiency, and is calculated by product amount and the incident photon number. The equation is listed below:

$$AQE(\%) = \frac{Number\ of\ reacted\ electrons}{Number\ of\ incident\ electrons} \times 100\%$$

What's more, total consumed electron number (TCEN) per unit reaction time and unit mass of photocatalyst is also used to evaluate the CO_2 reduction efficiency. It can be calculated by using the product amount and the incident photon number as shown in the following equation.

$$TCEN = \frac{\sum(cproduct \times nelectrons) \times Vreactor}{mcat. \times tirr.}$$

TCEN: the total number of consumed electrons; $V_{reactor}$: the volume of reactors; t_{irr}: the irradiation time; m_{cat}: the mass of photocatalysts; $c_{product}$: the concentration of certain products, and $n_{electrons}$: the corresponding consumed electrons number per mole of certain products. In addition, H_2 is not included in the statistical process of TCEN, because it does not come from CO_2 directly

The long-term stability (durability) is another important factor to measure the performance of photocatalyst. A very common experimental phenomenon is that decreased photocatalytic CO_2 performance is often observed with prolonged irradiation time. Usually, the appearance of this experimental phenomenon is caused by the deactivation of photocatalyst, which might be attributed to the occupation of active sites or instability of photocatalysts.

3. Photocatalysts

3.1. TiO_2 based photocatalysts

In the 1970s, TiO_2 is firstly used to evaluate its photocatalytic activity [10]. After that, a large number of attentions have been paid on the design and syntheses of various TiO_2 based photocatalysts to investigate their photocatalytic activities as well as corresponding reaction kinetics. TiO_2 has the advantages of rich abundance in earth, high chemical stability, low cost and corrosion resistance, etc.[18,213]. However, TiO_2 with a wide band gap (~3.2 eV) only absorbs UV light, which limits its utilization efficiency of solar light [214]. An ideal TiO_2 based photocatalysts would possess the following main features: i) narrow band gaps and good light absorbing abilities; ii) reasonable CB and VB boundaries for driving reduction of CO_2 as well as oxidation of H_2O; iii) effective charge separation capability; iv) proper morphology and suitable surface and v) large surface area with accessible channels. Therefore, many strategies have been proposed to improve their activity and various components such as metal oxides, metals or carbon based materials have been applied to incorporate with TiO_2, resulting in various TiO_2 based photocatalysts.

3.1.1. TiO_2 microstructure construction

In the past few years, TiO_2 with low dimensional structures is a kind of most popular photocatalysts and has been widely explored

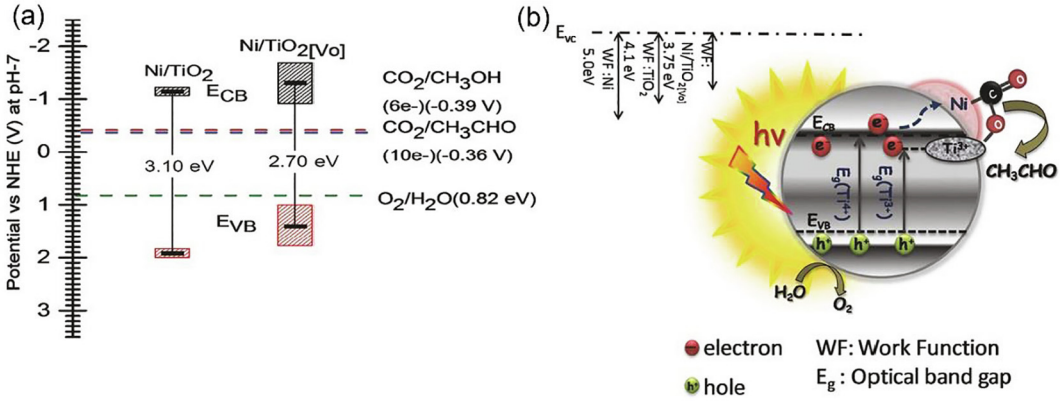

Fig. 1. (a) Band Boundaries of used photocatalysts. (b) Representative diagram of reduction mechanism for $Ni/TiO_{2[Vo]}$ (cited from Ref. [77]).

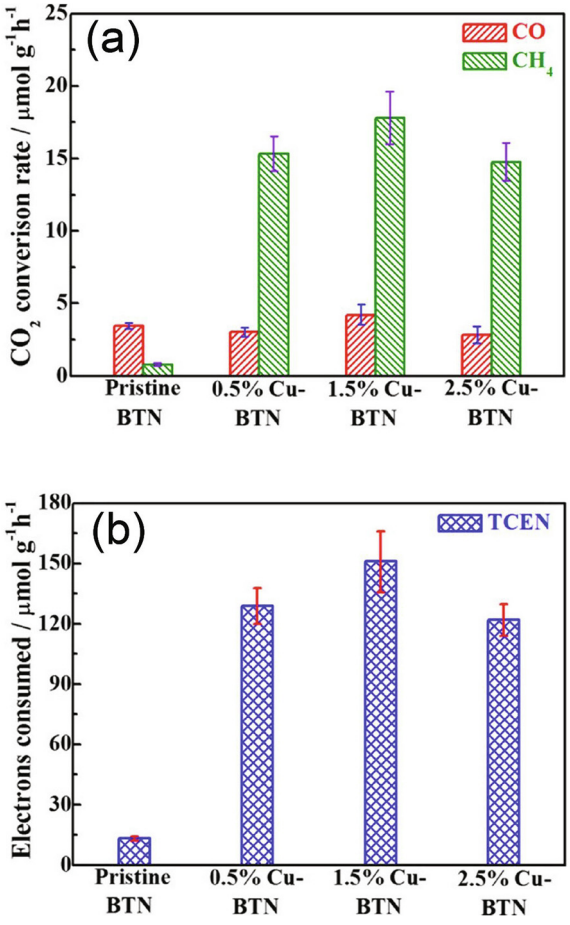

Fig. 2. CO/CH_4 generation rates (a) and the corresponding TCENs (b) of BTN and different Cu-BTN samples within the initial 2 h of irradiation (cited from Ref. [78]).

in the photocatalytic reduction of CO_2. Recently, TiO_2 with architectures like 1D Nanowires and 2D nanosheets/films have drawn more and more attentions owing to their higher electron transfer efficiency, larger surface areas and enhanced light harvesting or utilization efficiency. Therefore, this section will discuss the design and construction of individual TiO_2 with 1D, 2D and porous structures and their photocatalytic activity.

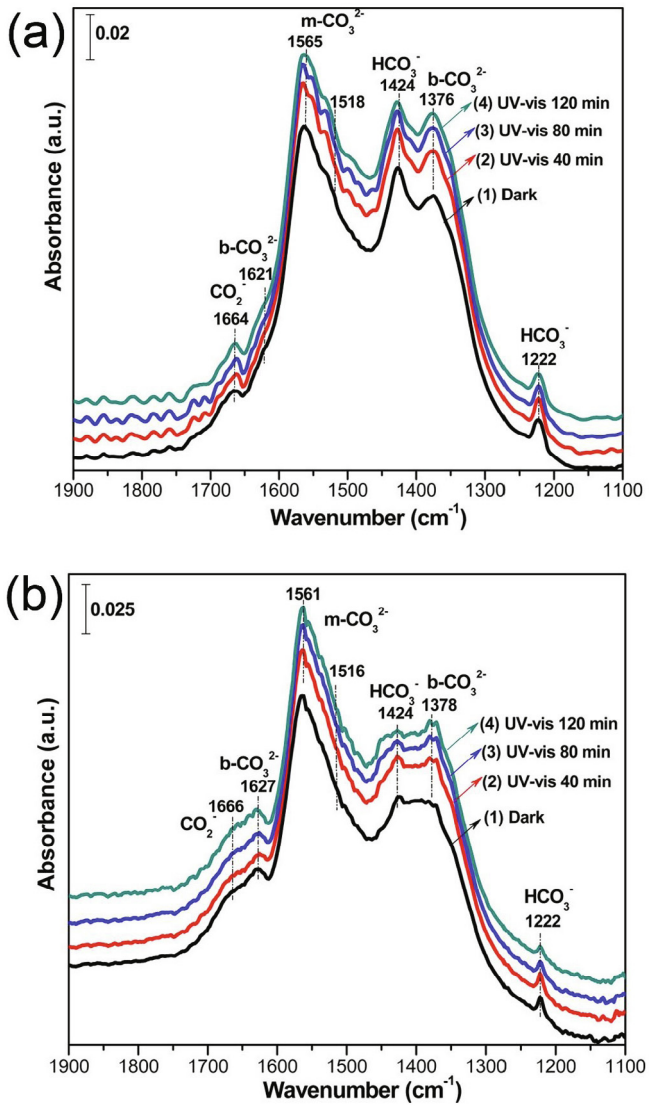

Fig. 4. In situ DRIFTS spectra of (a) Cu/Ti(air) and (b) Cu/Ti(H_2) after CO_2 and H_2O vapor adsorption in the dark and under UV – vis irradiation (cited from Ref. [81]).

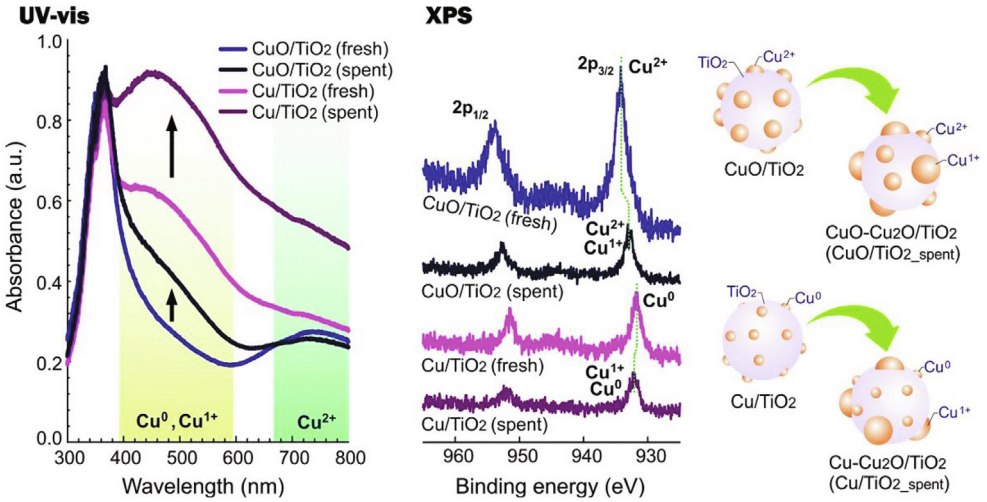

Fig. 3. Constantly varied Cu species in the photoreduction process (cited from Ref. [80]).

Porous TiO_2 with more CO_2 adsorption and surface active sites as well as larger number of available spaces generally shows better activity than nonporous ones. For instance, a simple, template-free hydrolysis-calcination synthetic route has been developed by Asefa et al. to prepare mesoporous TiO_2 photocatalysts [61]. The synthetic route includes the preparation of titanium glycolate microspheres (TGMs), hydrolysis step of TGMs and calcination step in air. They systematically study the effects of these experimental steps on the final structure of TiO_2 and find that the hydrolysis step is the key factor that might determine the formation of TiO_2 microspheres and small anatase grains. The generated materials with porous morphology possess good crystallinity, large specific surface area, and rich accessible active sites. These unique structural features endow these materials with much better performances (the formation rate of CH_4 is 14.75 μmol g^{-1} h^{-1}) than commercial TiO_2 (P25) (0.38 μmol g^{-1} h^{-1}).

1D TiO_2 nanotubes (TNTs) are good photocatalysts for CO_2 reduction by themselves. The modification of TiO_2 nanotubes might be able to further enhance their catalytic performances. A flame annealing method has been applied to modify TiO_2 nanotubes reported by Kar et al. [70]. After treatment, flame annealed TiO_2 nanotubes become square shaped, and its band gap changes from 3 to 2 eV, indicating that it could be sensitive to visible photons. Specially, flame annealed TiO_2 nanotubes exhibit an excellent activity toward photoreduction of CO_2 into CH_4 (CH_4 production rate, 156.5 μmol g^{-1} h^{-1}), standing on the upper level of reported values using TiO_2 as a photocatalyst lonely. Isotope labeled measurements demonstrate that the products indeed come from CO_2 substrate. Additionally, the visible light activity of flame annealed TiO_2 nanotubes may origin from defects located on the surface after treatment.

TiO_2 with more complicated structures have also been synthesized and tested their photocatalytic activities. For example, DC magnetron sputtering may be an efficient technique to prepare TiO_2 coatings for CO_2 reduction from a point of view on process scalability [71]. Varying the coating conditions has produced a series of different TiO_2 coatings such as crystalline TiO_2 coatings with different surface densities, amorphous TiO_2 coatings and quasi-amorphous TiO_2 coatings with very low densities. The experimental results reveal that the UV light absorption ability is related with surface defects and grain boundaries tuned by the crystal size and/or amorphicity of TiO_2 coatings. Furthermore, the product selectivity of different TiO_2 coatings varies greatly. TiO_2 coatings with amorphous or quasi-amorphous are in favor of methanol formation, while crystalline one prefers to produce CO. Similarly, three films based on TiO_2 (P25) with different loading mass have been synthesized to evaluate the effect of the film mass on CO_2 photoreduction by mean of doctor blading (DB) or airbrush techniques (AB: air brush; TAB: thick air brush) [72]. Naturally, different masses (1.5 mg for DB, 3.5 mg for AB and 6.5 mg for TAB) of deposited TiO_2 (P25) lead to different average film thicknesses (TAB > AB > DB). The photoreduction activity of each film is evaluated in batch mode. Although trace of ethane appears in the case of AB and TAB films, CH_4 is still the main product. A linear relationship is established between the deposited mass and the product yield. The linear correlation implies that all deposited TiO_2 (P25) in three films take part in the photocatalytic reaction. According to the observed experimental results, authors speculate that the critical mass of a film for optimum catalytic performance is approximately 10 mg.

3.1.2. TiO_2 doped with non-metal or transient metal ions

The modification toward structures and surfaces of TiO_2 can improve charge separation efficiency and enhance adsorption or activation of CO_2. However, these methods are still hard in changing the band structures of TiO_2 remarkably, which is critical for the ability of adsorbing solar light. To conquer it, doping TiO_2 with materials such as nonmetal components (e.g., nitrogen, carbon or transient metal ions (e.g., Cu, Ni, and V, etc.) have regarded as promising alternatives to narrow band gap and enhance light adsorption ability of TiO_2.

Employing HF and TiN as reactive substrates, a kind of N doped TiO_2 (NT) microsheets with exposed [101] and [001] facets have been prepared [75]. Then, N doped TiO_2 (NT) microsheets with exposed [101] and [001] facets are further hybridized with Ag and MnO_x nanoparticles, respectively. The Ag and MnO_x doped TiO_2 microsheets (Ag-NT-Mn) can absorb visible light, separate and utilize charges efficiently, and convert CO_2 into methanol with a formation rate of 0.53 μmol g^{-1} h^{-1}. The combination of facet design with co-photocatalysts (Ag and MnO_x) endows TiO_2 to be superior photocatalyst and the possible mechanism is proposed. The photo-excited electrons firstly transfer and accumulate on the surface of exposed [101] facets, and then transfer to Ag nanoparticles, taking part in the reduction reaction. At the same time, the photo-generated holes transfer to [001] facets and MnO_x in sequence, participating in the oxidation reaction. Naturally, spatial separation of photo-generated electron-hole pairs easily occurs. It is worth mentioning that the near field effect induced

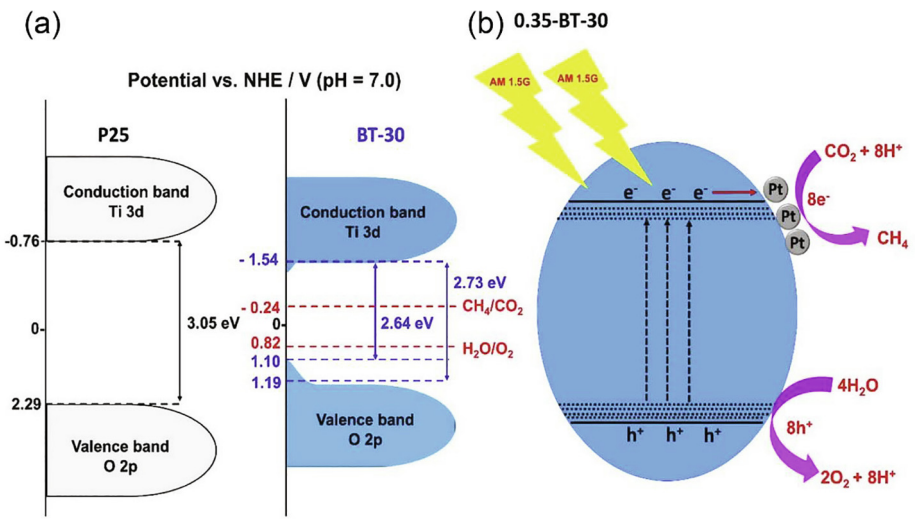

Fig. 5. (a) The band gap positions of P25 and BT-30. (b) Possible electrons transfer pathway in 0.35-BT-30 under AM 1.5G irradiation (cited from Ref. [87]).

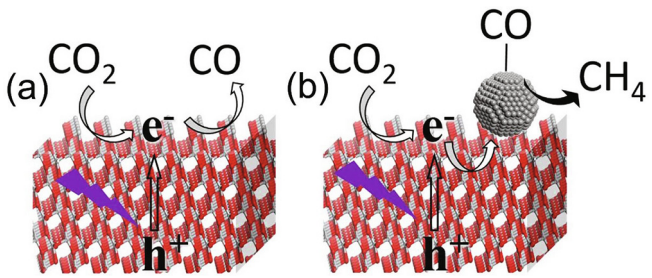

Fig. 6. Possible reaction paths of (a) TiO_2 and (b) Pt/TiO_2 photocatalysts (cited from Ref. [81]).

by surface plasmon resonance (SPR) of Ag can further facilitate the separation of electron-holes. In addition, the existence of Ag and MnO_x can also help to activate and dissociate H_2O and CO_2. To sum up, all factors enhance the performance of Ag-NT-Mn.

TiO_2 nanoparticles (25 nm) anchored on Ni foils are treated using microwave method in the presence of H_2/N_2 mixed gas, giving birth to a core–shell TiO_2 photocatalyst (HN-TiO_2) with highly active N, H and NH radicals [76]. After treatment, nitrogen species (NH groups) within the photocatalyst enhance the ability of absorbing visible light, verified by both experiments and DFT calculations. In addition, the V_o and Ti-N_s mid-gap states also facilitate efficient separation of electron-hole pairs. It should be mentioned that N and H atoms produce more electron-hole pairs and transfer separated electron-holes pairs to the external surface. Naturally, the photocatalyst can efficiently convert CO_2 to C_1 fuels. Additionally, Cu and Pt as the co-photocatalyst are introduced into HN-TiO_2, generating HN-TiO_2:Cu and HN-TiO_2:Pt, respectively, and their photoreduction CO_2 activities are evaluated. In this work, the photocatalytic activity promoted by Cu co-photocatalyst (producing methanol) is about eight folds higher than that of Pt co-photocatalyst.

A Ni nanoparticles doped black TiO_2 (Ni/$TiO_{2[Vo]}$) is used to study its photocatalytic CO_2 property by means of both experimental and computational methods, where dual active sites (Ni and oxygen vacancies) exist [77]. The results show that the cooperation between Ni nanoparticles and oxygen vacancies brings the following advantages: reduced activation energy for dissociating adsorbed CO_2 molecules addressed by the computational method; increased light harvesting through reducing the band gap and faster electron transfer. Hence, after modification, the photocatalyst can successfully reduce CO_2 to single product acetaldehyde (10 μmol g^{-1}, exhibiting better performance than the commercial TiO_2 (0.56 μmol g^{-1}) as well as Ni/TiO_2 (4.25 μmol g^{-1}). The photoreduction CO_2 pathway are proposed as follows (Fig. 1):

$$TiO_2 + h\upsilon \rightarrow TiO_2(e^- + h^+)$$

$$H_2O + 2h^+ \rightarrow 2H^+ + 1/2O_2 \quad E^0 = +0.82\ V$$

$$CO_2 + 6H^+ + 6e^- \rightarrow CH_3OH + H_2O \quad E^0 = -0.38\ V$$

$$2CO_2 + 10H^+ + 10e^- \rightarrow CH_3CHO + 3H_2O \quad E^0 = -0.36\ V$$

Due to the low cost, transition metals are regarded as more attractive co-photocatalysts than noble metals (such as Pt, Ag and Au). Specially, abundant TiO_2 based photocatalysts with Cu as the co-photocatalyst have been investigated to improve the photoactivity of TiO_2 and most of them produce CH_4. For example, in 2017, Cu nanoclusters (1–3 nm) have been successfully anchored on the surface of brookite TiO_2 quasi-nanocubes (BTN) via a one-pot hydrothermal reaction [78]. The decoration of Cu nanoclusters make VB of Cu-BTN rise slightly, resulting in the red-shift of absorption-edge, efficient separation of charges and the enhancement of electron utilization efficiency. Naturally, the resulted Cu-BTN prefers to facilitate the selective generation of CH_4, because it possesses rich surface oxygen vacancies and its CO_2/H_2O adsorption behaviors are different from that of pristine BTN (tends to produce CO). Remarkably, 1.5% Cu-BTN (17.81 μmol g^{-1} h^{-1}) exhibits much higher CH_4 production rate than that of pristine BTN (0.79 μmol g^{-1} h^{-1}) (Fig. 2).

At the same year, another series of Cu doped nanoporous TiO_2 photocatalysts with different Cu loadings have been synthesized and defined as Cu-TiO_2 [79]. The obtained Cu-TiO_2 materials could act as effective photocatalysts for CO_2 reduction. When the loading amount of Cu is 0.4 wt%, the best formation rate of CH_4 can reach up to 8.04 μmol g^{-1} h^{-1}, 21 times higher than that of commercial TiO_2 photocatalyst.

The above examples prove the decoration of Cu in TiO_2 could influence their photoreduction CO_2 activity and selectivity. Moreover, other Cu species (Cu^{2+}, Cu^+, or Cu^0) may also affect this photoreduction reaction. The following two examples provide a detailed assessment about effects of Cu species on the photocatalytic properties. Chen et al. have designed and synthesized different Cu species loaded TiO_2 to investigate their photocatalytic activity [80]. Two kinds of Cu species (Cu and CuO) are successfully introduced into TiO_2 hosts, generating Cu/TiO_2 and CuO/TiO_2 respectively, which are applied to evaluate their photocatalytic activities. Compared to TiO_2 photocatalysts, the interactions between Cu species and TiO_2 hosts in Cu species loaded TiO_2 photocatalysts increase the amount of Ti^{3+}, which promote the generation of intermediate

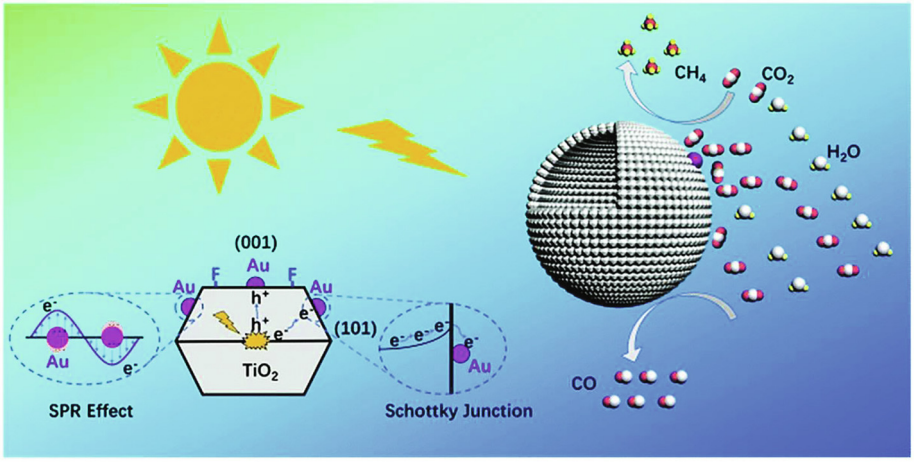

Fig. 7. The synergetic effect of as-synthesized Au-modified TiO_2 hollow microspheres (cited from Ref. [91]).

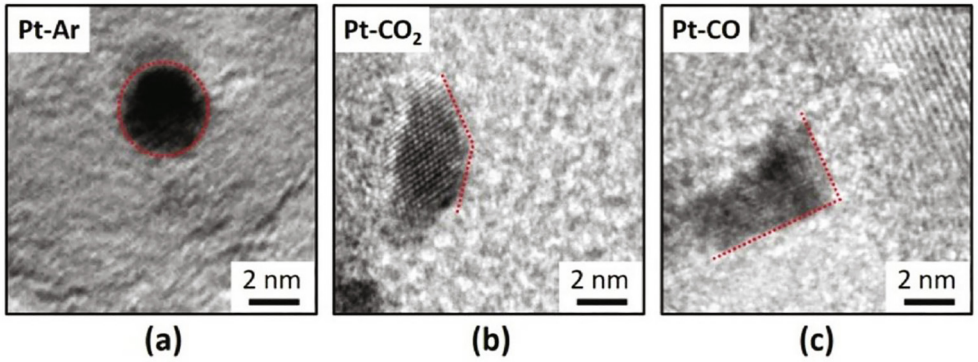

Fig. 8. TEM images of Pt nanoparticles synthesized under (a) Ar, (b) CO and (c) CO_2 atmospheres. Red dot lines represent surfaces of Pt nanoparticles (cited from Ref. [92]).

$CO_2^{\bullet-}$ species, enhancing photocatalytic activity of CO_2 hydrogenation (CH_4). In intermediate photocatalysts CuO-Cu_2O/TiO_2 and Cu-Cu_2O/TiO_2 formed under UV light irradiation, the coexistence of different Cu species prefer to extend the life of photoelectrons and enhance the photocatalytic activity of CO_2 hydrogenation (Fig. 3). However, if excess amount of Cu is decorated into the system, it also hinders the photoreaction performance of TiO_2. A large number of experimental results show that low concentration ($\leq$1 wt%) of Cu species can facilitate the photoreaction process, and the best yield of CH_4 reaches up to 28.72 μmol g^{-1}.

Obviously, Cu/TiO_2 composites have been widely investigated in photocatalytic reduction of CO_2. However, the deactivation mechanism of this kind of photocatalyst is not clear. In situ techniques, such as X-ray absorption spectroscopy (XAS) and DRIFTS have been used to detect the change of surface chemistry in the experiment process, to find the experimental evidences of photocatalyst deactivation [81]. Surfaces of oxidized sample (Cu/Ti (air)) are full of isolated Cu^{2+} sites, and reduced sample (Cu/Ti (H_2)) have rich Cu^+ sites and OH groups bonded by Ti^{3+} as well as oxygen vacancies (V_o). The performance of Cu/Ti(H_2) is better than that of Cu/Ti(air) due to the synergy of Cu^+ sites, OH groups and V_o. In-situ characterizations indicate that the consumption of Ti^{3+}–OH, the oxidation of Cu^+ sites into Cu^{2+} ones by holes and the changed coordination environment of Cu lead to the deactivation of Cu/Ti(H_2) (Fig. 4). Thermal treatment of Cu/Ti(H_2) in the presence of H_2 cannot restore to the original states, but hole scavengers (for example, methanol) do work, because photo-excited electrons can reduce Cu^{2+} sites to Cu^+ ones under light excitation. This study reveals that in situ techniques can provide clear experimental evidences to clarify the roles of photocatalysts during the photocatalytic process.

In this study, combining Cu and V co-doped TiO_2 with polyurethane (PU) gives birth to a composite photocatalyst (Cu@V-TiO_2/PU) [82]. The decoration of Cu and V introduces defects into TiO_2 lattice, causing the emergence of Ti^{3+} and oxygen vacancies. An intermediate band created by Ti^{3+} enhances the separation efficiency of electron-hole pairs as well as light absorption of Cu@V-TiO_2/PU. Besides, oxygen vacancies promote the adsorption of CO_2. The cooperation of Ti^{3+} and oxygen vacancies indeed improves the reduction efficiency. When Cu/TiO_2 and V/TiO_2 ratios (wt%) are 2 and 4 respectively, 2Cu@4V-TiO_2/PU exhibits the highest reduction efficiency. The production rates of CH_4 and CO under visible light are 933 and 588 μmol g^{-1} h^{-1}, respectively.

Different from the previously reported examples, in this study, as-synthesized Cu^{2+} doped TiO_2 nanorod based thin films can reduce CO_2 into methanol and ethanol as major products, owing to Cu^{2+} ions can capture electrons and separate the electron-hole pairs [83]. Besides, the increased concentrations of Cu^{2+} ions can decrease the band gap energy of TiO_2, making absorption spectra become broadened and extend to visible light range. The synergistic combination of Cu^{2+} deposition and TiO_2 nanorods promotes the generation of methanol and ethanol in high yields. Finally, the best formation rates of methanol and ethanol are 36.18 μmol g^{-1} h^{-1} and 79.13 μmol g^{-1} h^{-1} under the optimal experimental conditions, respectively.

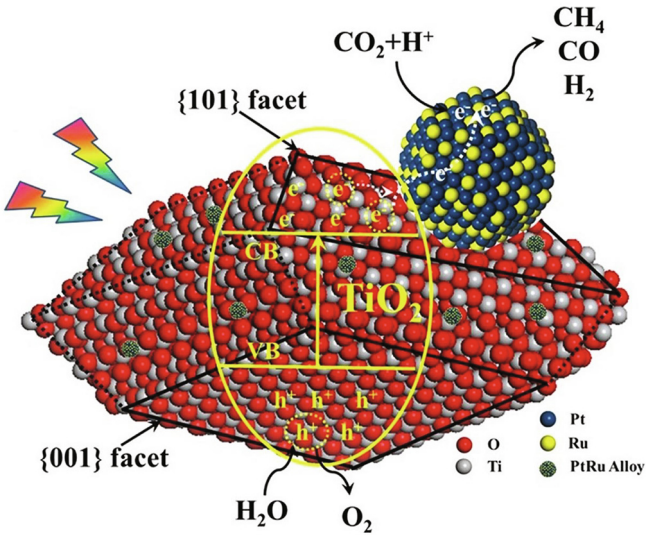

Fig. 9. Representative diagram of photocatalytic CO_2 reduction for PtRu/TiO_2 photocatalyst (cited from Ref. [95]).

3.1.3. TiO_2 doped with noble metals

Because of their unique electronic structures, noble metals (such as Pt, Au) and/or their alloys (Au/Cu, Cu/Pt, Cu/Pd, and Au/Pt) dispersed on surface of TiO_2 can serve as promising co-photocatalysts, and exhibit positive effects on the photoreduction of CO_2. The effects are listed below: i) the generation of Schottky barriers improving electron-hole pairs separation efficiency; ii) expanding the range of light absorption to the visible range; iii) modification of surface morphology through decoration; and iv) enhancing the charge separation and electron transfer. Benefiting from these advantages, many achievements have been obtained. In 2017, In et al. employ a simple and low-temperature technique to reduce titania using $NaBH_4$ as the reducing agent [87]. The generated blue titania (BT-X, X stands for the mass of used $NaBH_4$, in mg) possesses surface defects, narrow band gap, reasonable band position, and efficient charge separation. Furthermore, Pt with different amounts is also introduced into the BT-30 samples, which enhances the ability in photoreduction of CO_2 obviously, higher

than the pristine blue titania (Fig. 5a). Additionally, the effects about size and quantity of Pt nanoparticles on photoreduction CO_2 are also investigated. The maximum formation rate of CH_4 can reach up to 80.35 μmol g^{-1} h^{-1} under simulated solar light (Fig. 5b), which is superior to most of reported values. It should be mentioned that the photocatalyst maintains stable performances for at least five cycles. The ^{13}C isotopic labeling experiment demonstrates that CO_2 is the only carbon source.

Similarly, a family of Pd/TiO_2 have been synthesized via a simple glucose reduction method [88], where Pd nanoparticles distribute uniformly on the surface of TiO_2. A synergistic effect between Pd and TiO_2 enhances the photocatalytic activity. TiO_2 produces photo-excited electrons under light irradiation. Pd plays dual roles: capturing electrons to avoid the recombination of electron-hole pairs, adsorbing and activating CO_2 molecules for CH_4 generation. When 1.0 wt% Pd is loaded, the best yields of CH_4, CO, and C_2H_6 are 355.62, 46.35, and 39.69 μmol g^{-1}, respectively. Lately, a similar work is also covered, where Pt replaces Pd as the co-photocatalyst. A series of photocatalysts based on Pt/TiO_2 have been synthesized by means of a deposition–precipitation method [89]. All as-synthesized photocatalysts are used to test their photocatalytic reduction of CO_2. In the absence of Pt, CO is the main product using TiO_2 as the photocatalyst. The introduction of Pt leads to the emergence of CH_4, and the product selectivity of the best sample can reach up to 100%. Loading Pt/TiO_2 on mesoporous silica COK-12 can maintain the activity of photocatalytic reduction CO_2 as well as a high selectivity toward CH_4. At the end of the experiment, after-reaction attenuated total reflection infrared spectroscopy (ATR-IR) and in-situ near ambient pressure XPS have been performed to find the reaction intermediates and reveal the mechanism of selectivity. The results reveal that a strong adsorption between CO and Pt sites can promote the photocatalytic reduction of CO_2 into CH_4 (Fig. 6).

Noble metal nanoparticles usually possess localized surface plasmon resonance (LSPR) irradiated by a suitable light source, depending on the size, shape, and surface charge of nanoparticles. In order to understand the role of plasmonic effect on photocatalytic reaction process, Lee group carries out an attempt. A series of core–shell Au@SiO_2 nanoparticles based on Au with different sizes (4, 8, 18 and 26 nm) have been synthesized [90]. The as-prepared nanoparticles are introduced into Pt/TiO_2 in order to study the influence of their size-dependent plasmonic effect on photocatalytic reduction of CO_2. Different light resources are also employed to investigate the influence of plasmonic effect on photocatalytic activities. Irradiated by 365 and 530 nm LED lamps, photocatalytic activities of composite photocatalysts are remarkably enhanced, demonstrating that the LSPR effect of Au nanoparticles and Au@SiO_2 really works. In contrast, the photocatalytic activity remains unchanged under 365 nm LED lamp irradiation. Besides, various experiments show that LSPR effect of Au nanoparticles and Au@SiO_2 nanoparticles reaches their best levels when the sizes of them are 18 nm.

Two years later, a kind of porous TiO_2 hollow microspheres have been prepared [91], which possess rich [0 0 1] facets and surface defects (Ti^{3+} and oxygen vacancies (V_o)) through a fluoride-mediated self-transformation pathway. Then TiO_2 hollow microspheres are doped with Au nanoparticles (average size, 14 nm) by means of a photochemical deposition method. In this structure, multiple synergetic effects between TiO_2 and Au nanoparticles are used to improve the ability of light harvesting, charge separation, CO_2 adsorption and activation. The possible synergetic effects of these counterparts are presented as follows (Fig. 7): firstly, the light trapping effect of hollow cavities and SPR effect of Au nanoparticles enhance the ability of light harvesting; secondly, Schottky junctions between Au nanoparticles and TiO_2 as well as its [0 0 1]/[1 0 1] facet junctions can promote the charge transfer efficiency significantly and finally, the strong interactions among Au nanoparticles, CO_2 molecules and rich surface defects (Ti^{3+} and V_o sites) might facilitate the adsorption and activation of CO_2. All of the above factors indeed improve the photocatalytic CO_2 reduction activity.

The example reported by Cho et al. reveals that controlling the shape of metal co-photocatalyst may be an effective approach to enhance the catalytic efficiency of photocatalysts [92]. They have designed and carried out a series of experiments, where many factors related to photocatalytic CO_2 reduction, such as particle shape of metal co-photocatalysts tuned by gas ligands (Ar, CO_2 and CO), the types of metal co-photocatalyst (Au, Ag, Cu and Pt) or gas ligands are considered. The experimental results demonstrate that the performances (activity and selectivity) of photocatalytic CO_2 reduction reaction can be changed significantly through tuning the types (Ar, CO_2 and CO) of gas ligands and metal co-photocatalysts. Different weak interactions between these gas ligands and metal co-photocatalysts lead to different particle shapes of metal co-photocatalysts (Fig. 8), which promote the formation of various exposed facets. Furthermore, the various exposed facets of metal co-photocatalysts can lead to different photocatalytic CO_2 reduction activities. For instance, metal co-photocatalysts grown in CO_2, Pt and Cu, possessing strong interactions with CO, can exhibit better performance in photocatalytic CO_2 conversion activity than those of Au and Ag. While, when these metal co-photocatalysts are grown in CO, Au and Ag show the enhanced photocatalytic CO_2 conversion activity because of their relatively weak interactions with CO. In summary, the proper

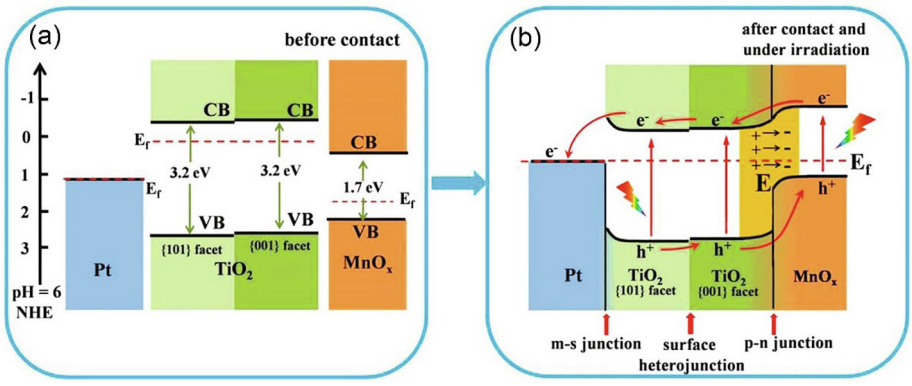

Fig. 10. Schematic representation of proposed reduction mechanism of sample TMP. The band edges of TiO_2, Pt, and MnO_x before (a) and after (b) combination under irradiation (cited from Ref. [99]).

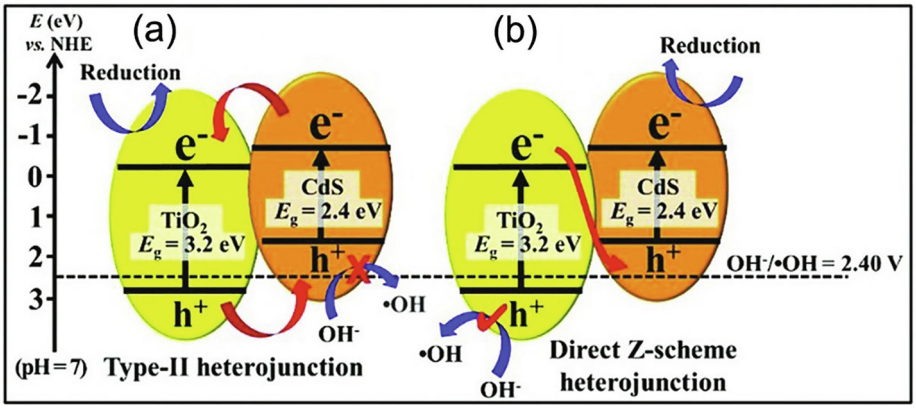

Fig. 11. Schematic diagram of charge-carrier transfer pathway according to the type-II (a) and direct Z-scheme (b) heterojunction in TiO_2/CdS composites (cited from Ref. [101]).

interactions between the gas ligands and metal co-photocatalyst surface reveal that it plays a key role in improving the CO_2 conversion activity.

Compared with single noble metal co-photocatalyst, the alloying strategy would overcome the shortcomings of each component, and provide an opportunity for enhancing the performances of photocatalysts [93]. Xiong group employs TiO_2 nanosheets as the host framework to loads Pd_xCu_1 alloys (Cu atoms isolated in Pd lattice), giving birth to a hybrid photocatalyst Pd_xCu_1-TiO_2 with highly selective sites. The hybrid photocatalyst can efficiently convert CO_2 into CH_4 (19.6 μmol g^{-1} h^{-1}). The synchrotron-radiation characterizations as well as theoretical simulations find that combination of Cu and Pd provides the couple Cu-Pd sites that can facilitate CO_2 adsorption and restrain H_2 evolution. Additionally, the d-band center of Cu sites can activate CO_2 efficiently. Summarily, Pd_7Cu_1-TiO_2 photocatalyst displays a formation rate of 19.6 μmol g^{-1} h^{-1} for CH_4, and the selectivity of CH_4 can reach up to 96%. It provides a new idea to design photocatalysts with active sites at atomic level to enhance the catalytic performance.

A series of AuPd nanoparticles doped three-dimensionally ordered macroporous (3DOM) TiO_2 (AuPd/3DOM-TiO_2) with core–shell structure have been successfully synthesized through a facile gas bubbling-assisted membrane reduction (GBMR) method [94]. In this structure, 3DOM TiO_2 shows a uniform 3D ordered macroporous structure, and acts as the host framework to load AuPd nanoparticles. AuPd nanoparticles with average sizes of about 3.7 nm can be uniformly distributed on the surface the host framework. Thus-obtained 3DOM-TiO_2 possesses slow photon effect, which can improve the light-harvesting efficiency together with SPR effect of Au nanoparticles. Besides, AuPd nanoparticles can capture photoelectrons from TiO_2, and enhance the separation efficiency of photo-generated charges. Specially, this photocatalyst exhibits an excellent photocatalytic activity, and can efficiently convert CO_2 into CH_4 with a production rate of 18.5 μmol g^{-1} h^{-1} under light irradiation. It should be mentioned that its selectivity toward CH_4 can reach up to 93.9%.

Adopting the same method, Wei et al. successfully deposit two kinds of noble metals and their alloy on the exposed {101}-39% and {001}-61% facets of anatase TiO_2 nanocrystals selectively [95]. This recombination can separate photo-generated electron-hole pairs efficiently, and promote electrons enrichment on {101} facet. Noble metal nanoparticles can trap electrons via the vectorial transfer of TiO_2 to PtRu, and further enrich the electrons. Varied metal co-photocatalysts lead to different products. Pt based photocatalyst shows formation rates of 22.9 and 52.8 μmol g^{-1} h^{-1} for CH_4 and H_2 respectively, while Ru based photocatalyst prefers to produce CO (65.1% selectivity, 18.1 μmol g^{-1} h^{-1}). PtRu alloy based photocatalyst exhibits the best performance (CH_4, 38.7 μmol g^{-1} h^{-1}) due to the synergic effect of Pt and Ru components (Fig. 9), and its AQE is 0.98%. The synergic effect of Pt and Ru makes PtRu/TiO_2 photocatalyst overcome the limitation of generating H-containing intermediates to activate CO_2 and promote the reduction of CO_2 to CH_4.

3.1.4. TiO_2-based heterostructures

Up to now, various light responsive photocatalysts, such as Cu_2O, CdS, and so on have been designed and synthesized. The combination of TiO_2 with various light responsive photocatalysts gives birth to different types of heterojunctions, which can be used to enhance the photoreduction activity of CO_2. Generally speaking,

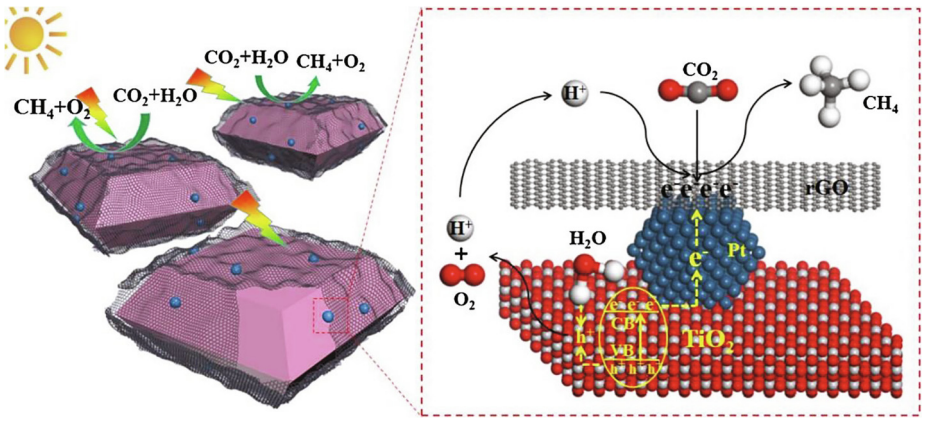

Fig. 12. Proposed reaction mechanism of (Pt/TiO_2)@rGO-n photocatalysts for CO_2 photoreduction with H_2O (cited from Ref. [104]).

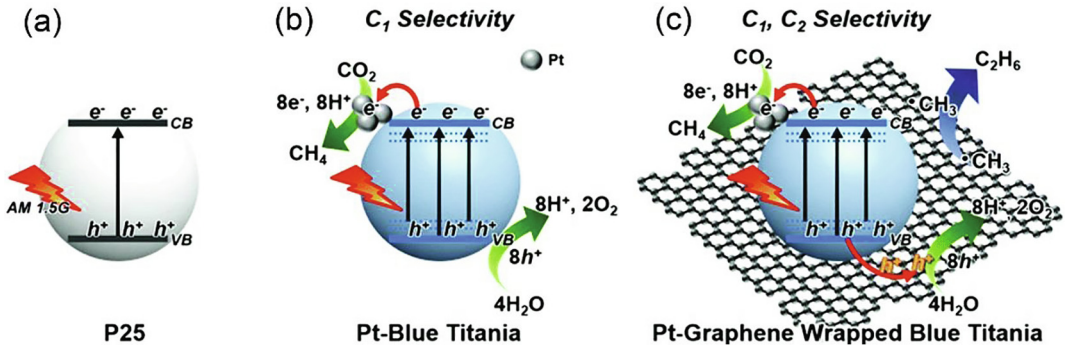

Fig. 13. Representation of photoreduction CO_2 activity. (a) P25 nanoparticles, (b) reduced blue titania (RBT) doped by Pt, and (c) graphene-wrapped RBT (cited from Ref. [106]).

heterojunctions possess rich CO_2 adsorption sites, reasonable CB and VB edges as well as narrow band structures, enhanced separation of photo-generated electron-hole pairs. Naturally, heterojunctions usually exhibit good performances. A kind of Cu_2O/TiO_2 based photocatalyst has been prepared via a simple solvothermal method, which possesses controlled morphology and crystallinity [96]. Various characterizations, including diffuse reflectance UV–visible (DRUV) spectroscopy, ultraviolet photoelectron spectroscopy (UPS), and XPS spectroscopy reveal the generation of a p-n heterojunction and the Type II band alignment in the composite. The product of photoreduction CO_2 is CO, and its production rate is 2.11 $\mu mol\ g^{-1}\ h^{-1}$. It should be noted that XPS spectra of Cu_2O and Cu_2O/TiO_2 before and after the experiments reveal the existence of hydroxyl radicals (·OH), which can also imply that TiO_2 might mitigate the photocorrosion of Cu_2O. These results also confirm the Z-Scheme is the main mechanism during CO_2 photoreduction.

Wu et al. creatively apply celery stalk as the biological template to prepare a kind of TiO_2/ZnO heterostructure (anatase TiO_2 and wurtzite ZnO) through a facile sol–gel and hydrolysis process [97]. The band matching of ZnO and TiO_2 might facilitate the efficient charge transfer and separation of electron-hole pairs. Specially, TiO_2/ZnO heterostructure can successfully convert CO_2 into CH_4 with a production rate of 2.56 $\mu mol\ g^{-1}\ h^{-1}$, 5 times higher than that of pure TiO_2 (0.512 $\mu mol\ g^{-1}\ h^{-1}$). This study provides a promising strategy to apply biotemplates to design powerful CO_2 photocatalysts.

One year later, Li et al. report a modified TiO_2 nanotube with oxygen vacancies and trace CoO_x, defined as TiO_{2-x}/CoO_x [98]. After modification, improved activity for producing CH_4 and CO is observed under ultraviolet irradiation and 393 K, and the yields of CH_4 and CO are 111.3 and 13.2 times higher than the results obtained at 298 K, and 175.1 and 2.9 times higher than the pristine TiO_2. Control experiments reveal the synergistic effect of oxygen vacancies and CoO_x is indispensable on the photothermocatalytic reduction of CO_2 to CH_4. Oxygen vacancies adsorb and activate CO_2, and CoO_x traps holes and releases more protons as well as the oxidation of H_2O. The cooperation of oxygen vacancies and CoO_x on TiO_2 surface improves the separation efficiency of photo-generated electrons-hole pairs, and facilitates the reduction of CO_2 to CH_4. This work provides a different perspective through the comparison of photothemocatalysis and photocatalysis.

The single heterojunction can improve charge separation slightly. Therefore, the formation of multijunctions may be very useful for synergistically improving the charge separation. Naturally, a ternary TiO_2-MnO_x-Pt hybrid photocatalyst (TMP) with multijunctions has been prepared [99]. Both {001} and {101} facets in TiO_2 are exposed, where a surface junction exists, and MnO_x nanosheets and Pt nanoparticles disperse on each facet, causing another two heterojunctions: p-n junction between MnO_x and TiO_2 {001} facet and metal–semiconductor junction between Pt and TiO_2 {101} facet. Summarily, three different junctions exist (Fig. 10), which can separate photo-generated electron-hole pairs efficiently, demonstrated by the photocurrent-time curves and Mott-Schottky plots. The synergistic effect among three compositions makes it be better photocatalyst that exhibits higher yield of CH_4 and CH_3OH than pristine TiO_2 nanosheet film.

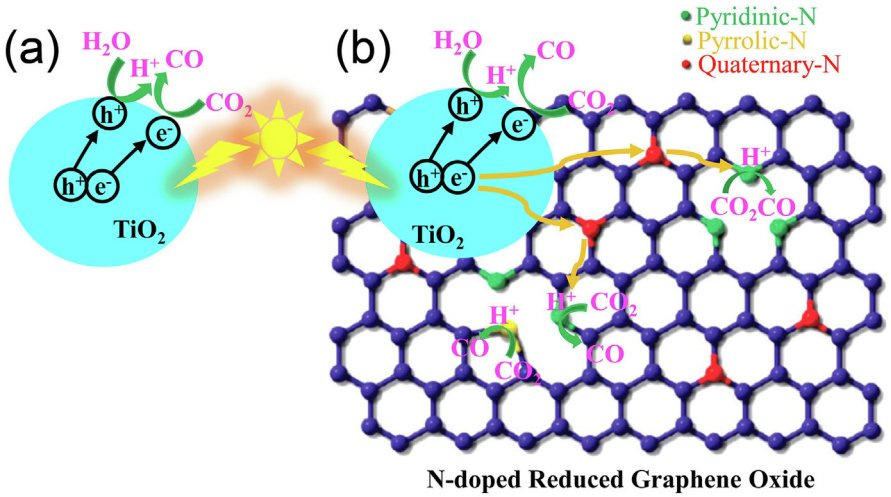

Fig. 14. Possible reaction mechanisms of (a) TiO_2 and (b) TiO_2/NrGO-300 samples (cited from Ref. [108]).

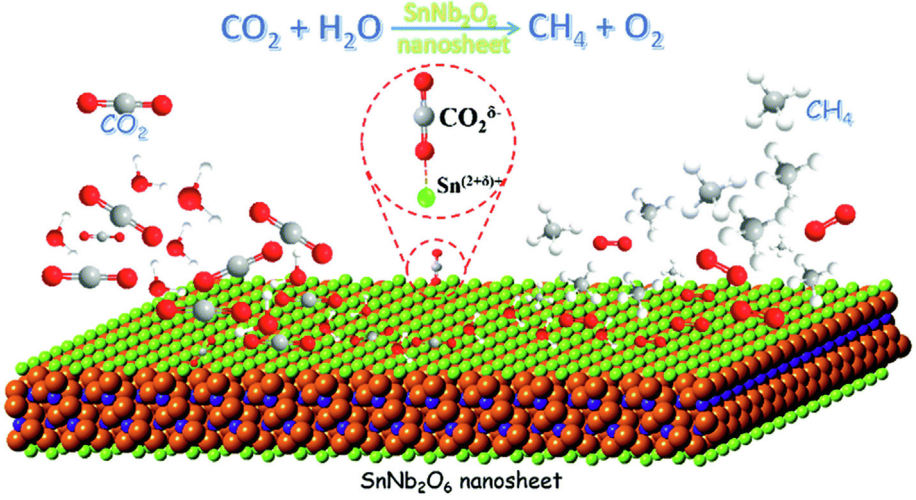

Fig. 15. Schematic diagram of photocatalytic reaction for $SnNb_2O_6$ nanosheets (cited from Ref. [122]).

A hybrid photocatalyst based on TiO_2 nanorod array has been synthesized through depositing Cu^{2+} ions and cadmium sulfide quantum dots (CdS QDs) on its surface [100]. Its photocatalytic behavior is evaluated, and ethanol is the major product. TiO_2 nanorod array provides available spaces for adsorbing CO_2, and Cu^{2+} ions together with CdS QDs expand light absorption, both of which promote the photoreduction process of CO_2. Effects of some factors on photoreduction experiments, such as the amount of CdS and reaction temperatures have been considered. Specially, the band gap energy of this photocatalyst decreases following the increased amount of CdS QDs. Besides, the increased temperature can adsorb more CO_2 and promote the generation of photo-excited species. Under the optimum experimental conditions, this photocatalyst possesses much better performance than conventional photocatalysts, and its maximum yield of ethanol is 109.12 μmol g^{-1} h^{-1}.

Direct Z-scheme photocatalysts have been widely explored, because they could preserve photo-generated electrons-holes with higher redox potentials, which is in favor of producing high photoreduction efficiency. Following previous reports, Yu group has synthesized a kind of Z-scheme photocatalyst (hybrid film based on TiO_2 and CdS (TiO_2/CdS)) to find experimental evidences of the direct Z-scheme charge transfer [101]. Fortunately, in situ irradiated XPS and the successful detection of hydroxyl radical (**.**OH) clearly reveal the existence of direct Z-scheme charge-carrier transfer pathway under the experimental condition (Fig. 11). Furthermore, DFT simulation also reveals the intrinsic formation mechanism of the direct Z-scheme heterojunction. TiO_2/CdS can reduce CO_2 into CH_4 with an optimized CH_4 formation rate of 11.9 μmol h^{-1} m^{-2}. Similarly, $CuInS_2$ nanoplates, as the sensitizer [102], have been coated on TiO_2 nanofibers through a hydrothermal method, generating a TiO_2/$CuInS_2$ hybrid photocatalyst. It exhibits an excellent photocatalytic activity, which might be attributed to the formation of direct Z-scheme heterojunction between TiO_2 and $CuInS_2$, confirmed by XPS measurement, DFT calculation and free radical analysis.

Xu et al. carry out a very meaningful work to investigate whether the carbon based residues from photocatalysts can take part in the photoreduction reaction. They employ Bi_2WO_6-TiO_2 (B-T) as a representative sample [215], and study the performance of B-T samples under N_2 and CO_2 atmosphere. After systematic study, they put forward the following hypothesis: firstly and most importantly, the photocatalysts should not contain too much carbon based reagents, and would be better removed through various approaches like UV-irradiation or themolysis on the premise of retaining the structure and performance; secondly, the activity under inert gas is used to evaluate the contribution of carbon based residues in order to understand the true activity of photocatalysts; thirdly, the selected photocatalyst can convert CO resulting from the generated carbon based residues to CH_4. Despite the Z-scheme charge transfer in B-T that can promote this process, the Z-scheme based photocatalysts should be properly designed and synthesized to avoid the influence of carbon based residues.

3.1.5. The combination of TiO_2 with carbon materials

Carbon based materials are widely explored to improve the performances of hybrid photocatalysts for CO_2 reduction. Commonly used carbon materials (graphene oxide (GO), reduced graphene oxide (rGO), and so on) have been widely employed as co-photocatalysts due to their good conductivity [216,217]. For example, Graphene is one kind of famous layered materials with flexible structures consisting of sp^2 hybridized carbons and exhibits unique electrical properties, for example, the high electron mobility is beneficial for the photoreduction of CO_2 [218]. The combination of carbon based materials with TiO_2 may be an efficient strategy for improving the photocatalytic activity.

Employing pre-synthesized 1D carbon nanofibers as the core to grow TiO_2 on the surface, a kind of 1D carbon nanofibers@TiO_2

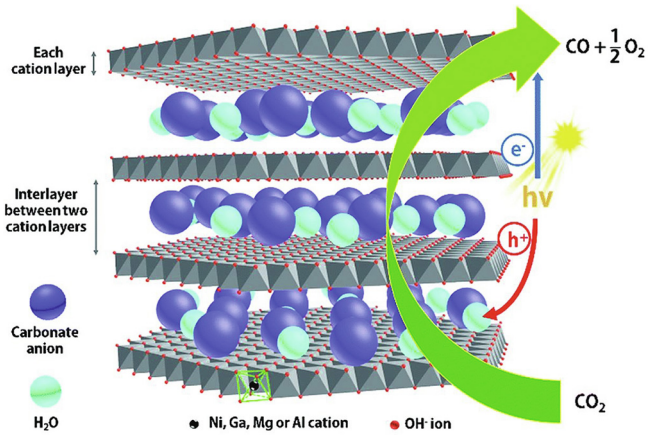

Fig. 16. Representative structures of the quadruple NiMgGaAl (NMGA) structure and its schematic diagram of CO_2 into CO. NMGA, NG, NGA and NMG possess similar structures except metal ions. Metal ions coordinating to OH^- are linked together through edge-share and CO_3^{2-} as well as H_2O molecules are situated in the interlayer regions (cited from Ref. [125]).

core–shell nanocomposite has been prepared [103]. This nanocomposite exhibits much higher performance (13.52 μmol g^{-1} h^{-1}) than that of pure TiO_2 (5.97 μmol g^{-1} h^{-1}). TiO_2 anchored on carbon nanofibers can expose more active sites, and carbon nanofibers can adsorb more light to accelerate the separation of electron-hole pairs and enhance the photocatalytic CO_2 reduction ability.

Recently, GO has been demonstrated to be able to improve photocatalytic performances, and can act as co-photocatalysts, sensitizers, and so on. GO can accept electrons and transfer them efficiently, accelerating the separation of photo-generated electrons-hole pairs. Additionally, rich surface hydroxyls and extended π bonds can enhance the adsorption and activation of CO_2. The combination of GO with other photocatalysts may result in efficient photocatalysts. Naturally, many achievements have been obtained. Pt/TiO_2 nanocrystals have been wrapped by rGO sheets, generating a new core–shell structured photocatalyst ((Pt/TiO_2)@rGO-n) [104], where {001} and {101} facets of TiO_2 nanocrystals are exposed, and TiO_2 nanocrystals, Pt and rGO serve as the core, mediator and shell, respectively. In this photocatalyst, each component has a clear role in photoreduction of CO_2. TiO_2 nanocrystals can separate photo-generated charges, and Pt nanoparticles transfer and collect photo-generated electrons (Fig. 12). rGO sheets play two important roles: on one hand, it can accept and transport electrons; on the other hand, it might adsorb and activate CO_2 by means of rich hydroxyls and extended π bonds. The arrangement of rGO, Pt and TiO_2 is in favor of the vectorial electron transferring with the possible pathway: TiO_2 → Pt → rGO, and might be essential to separate photo-generated charges. Notably, this photocatalyst can selectively reduce CO_2 to CH_4 (closely to 100%) with a production rate of 41.3 μmol g^{-1} h^{-1}. Moreover, this photocatalyst also possesses the remarkable stability for CO_2 photoreduction.

Previous work find that GO can improve photoelectrochemical properties of TiO_2 nanostructures, because GO can not only improve the light absorption ability but also facilitate the charge transfer. Directed by this idea, In group covers a noble metal-free photocatalyst based on TiO_2 nanotubes arrays (TNT) surrounded by a rGO [105]. The prepared nanostructure possesses enhanced photocurrents, and exhibits an enhanced activity toward conversion of CO_2 into CH_4. The dual functions of GO indeed play important roles in the enhancement of photophotocatalytic performances. As a follow-up study, the same group combines reduced blue titania nanoparticles (RBT) as the substrate with GO sheets to generate a core–shell structure (Fig. 13) [106]. Various analytical methods like HR-TEM, Raman, and XPS analysis have demonstrated the successful formation of Ti-O-C bond. Pt nanoparticles as a kind of sensitizer, have been introduced into this system. Interestingly, the main photoreduction products involve ethane (C_2H_6) and CH_4. The UPS study reveals that in the C_2H_6 formation process, band bending between the reduced blue-titania and GO plays a key role. Furthermore, transient absorption spectroscopy implies that photo-generated electrons locate around Ti^{3+} sites, and photo-generated holes transfer to GO, which act as an electron extractor, greatly inconsistent with previous assumptions. The photocatalyst promotes the continuous occurrence of multielectrons transfer, generating $\cdot CH_3$. Through tuning the photocatalyst, the product changes from 100% CH_4 to the mixed product (CH_4: C_2H_6 with a 3:1 ratio). Under a AM 1.5G illumination, 77 μmol g^{-1} C_2H_6 and 259 μmol g^{-1} CH_4 can be produced after 7 h, and the AQY is 7.9%. It should be mentioned that stable photocatalytic performance can last for 42 h, and $^{13}CO_2$ labeling experiments demonstrate CO_2 is the actual carbon source.

The high price and degradation of noble metals limit their further application, layered transition metal disulfide materials (e.g., molybdenum disulfide (MoS_2) and tungsten disulfide (WS_2), etc.) have been used to replace noble metals due to their high stability, low cost and promising catalytic features. A hierarchical porous structure (TGM) combing mesoporous TiO_2 with macroporous 3D graphene aerogel as well as a few MoS_2 has been reported [107]. The existence of meso/macropores, relative amounts and configuration of each component in this hierarchical structure contributes to the high photocatalytic performance. The porous and relative ordered structure offers large surface area, rich reaction sites as well as substrate and products diffusion pathways. The electrons transfer from TiO_2 to MoS_2 via GO lowers the charge recombination and increases the CO_2 reduction potential. The CO production rate is 92.33 μmol g^{-1} h^{-1} with a selectivity of 97%, higher than that of bare TiO_2 (6.4 μmol g^{-1} h^{-1}). The durability of TGM composite is also measured, and its performance can maintain for at least 15 cycles.

Previous reports reveal N dopants in N-graphene materials can capture more CO_2 molecules, and change the electronic properties and local surfaces of GO materials, which leads to that this material may be an effective photocatalyst with excellent performances. The mixture of urea, GO and TiO_2 gives birth to a family of TiO_2/nitrogen doped rGO (TiO_2/NrGO) nanocomposites via a hydrothermal method [108], which possess various concentrations and bonding configurations of nitrogen (Fig. 14). The effect of doping quantity and bonding configuration of nitrogen on the catalytic performance of TiO_2/NrGO is also studied. Among them, TiO_2/NrGO-300, generated in a urea/GO solution (300:1 mass ratio), possesses the best performance (CO yield is 356.5 μmol g^{-1}), higher than those of pure TiO_2 (83.1 μmol g^{-1}) and TiO_2/rGO (162 μmol g^{-1}), respectively. Furthermore, TiO_2/NrGO still possesses a very stable performance with the prolongation of reaction time, while TiO_2 and TiO_2/rGO exhibit lower catalytic activity after a few hours. Owing to the reasonable nitrogen quantity and nitrogen-bonding configurations from NrGO, it can not only adsorb CO_2 onto the surface, but also promote electron-hole pairs separation, finally improving the photocatalytic performance.

3.2. Metal Oxides/Hydroxides based photocatalysts

Although most of efforts focus on improving the CO_2 photocatalytic performance of TiO_2 and its derivatives, exploration of other metal oxides/hydroxides based materials as alternative photocatalysts is also ongoing [219]. Transition metal oxides (Fe_2O_3, Cu_2O, etc.) are inexpensive and plentiful, antioxidant, and visible-light response. As a result, many metal oxides/hydroxides and their composites have been employed for photoreduction of CO_2.

$SnNb_2O_6$, as a classic layered semiconductor, is naturally used for photoreduction of CO_2. Monolayer 2D $SnNb_2O_6$ nanosheets with high crystallinity have been synthesized through a hydrothermal method without any organic additives [122]. $SnNb_2O_6$ nanosheets are firstly used to reduce CO_2 to CH_4 under visible light irradiation. The thickness of the as-synthesized $SnNb_2O_6$ nanosheets is about 1 nm. It exhibits larger surface area, enhanced photoelectrical properties and surface basicity as well as higher CO_2 uptake compared to common layered $SnNb_2O_6$. Therefore, $SnNb_2O_6$ nanosheets exhibit better activity than that of layered ones. In situ FTIR spectrum has been used to detect the intermediate, and suggest that the $CO_2^{\cdot-}$ species may be main intermediate in the CO_2 photoreduction process, which turn into CH_4 combining with protons from water (Fig. 15). The optimum samples show the highest CH_4 formation rate of 110.9 μL g^{-1} h^{-1}.

In this study, Ozin group proposes a hypothesis that the reaction substrates of synthesizing In_2O_3 nanoparticles play a great influence on the photocatalytic activity [123]. The redox property of anion from used substrates influences the defect formation on the surface of the nanoparticles remarkably. In_2O_3 nanoparticles constructed from indium nitrate and indium hydroxide, exhibit different photocatalytic activities. The nanoparticles based on

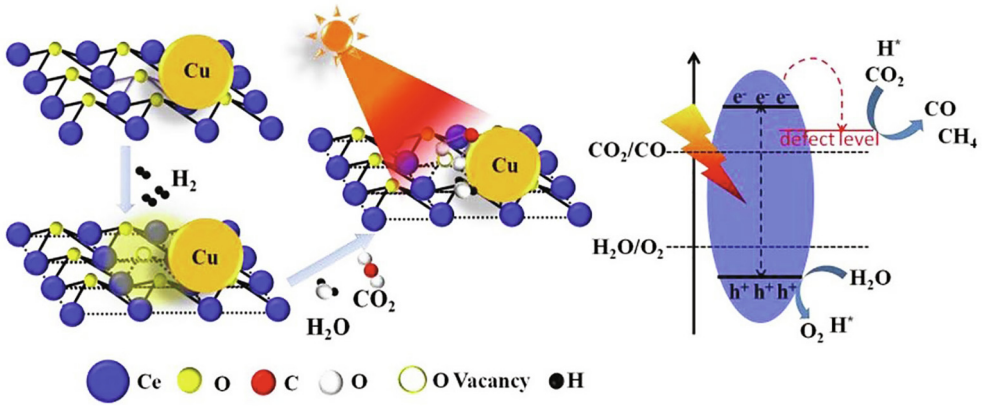

Fig. 17. Possible reduction mechanism of Cu/CeO_{2-x} (cited from Ref. [136]).

indium hydroxide possess more surface oxygen vacancies, and exhibit a better activity, compared to those nanoparticles constructed from indium nitrate. The study demonstrates that reaction substrate can influence the surface morphology of In_2O_3 nanoparticles, further affecting the final photocatalytic activity.

Engineering of polymorphism sheds light on optimizing the photocatalytic activity of a photocatalyst. Metal semiconductor $In_2O_{3-x}(OH)_y$ is selected to investigate the effect of polymorph on the photocatalytic activity [124]. The finding is that the Lewis acidity and basicity of rhombohedral $In_2O_{3-x}(OH)_y$ (rh-$In_2O_{3-x}(OH)_y$) are modified through the change of polymorph, together with its strong tendency of H_2 dissociation, influencing its activity and selectivity. Naturally, rh-$In_2O_{3-x}(OH)_y$ turns into an efficient photocatalyst applicable in the conversion of CO_2 to CH_3OH and CO at atmospheric pressure. An operando DRIFT study and DFT calculation presents clear evidences for the generation of CH_3OH and CO. The excellent performance results from enhanced activity of surface Lewis acid–base pairs. This work demonstrates that optimizing the Lewis acidity and Lewis basicity of heterogeneous photocatalysts may be an efficient strategy for enhancing the photocatalytic performance via polymorph selection.

Mixed metal-based layered structures may be promising photocatalysts for CO_2 conversion. Herein, a quadruple metal-based layered structure based on aluminium (Al), gallium (Ga), magnesium (Mg), and nickel (Ni), denoted as NMGA, is prepared [125], and can convert CO_2 into CO with about 100% selectivity (Fig. 16). Under the condition that the valence state of Ga and Al ions remains unchanged, the shifted oxidation states of Ni and Mg ions enhance electronegativity of their neighboring oxygens (O), which can capture abundant CO_2 molecules. Naturally, NMGA exhibits an enhanced activity. Later on, a new zinc silicate nanosheet $[Mg_{0.1}Zn_6(Si_{7.9}Al_{0.1})O_{20}(OH)_4{\cdot}nH_2O]$ with layered structure has been prepared through a liquid-phase epitaxial growth route [125], where 2D silica serves as the Si source as well as a template with reasonable lattice parameters. 2D silica limits the growth of zinc silicate in the 2D directions, leading to the formation of ultrathin zinc silicate nanosheets with a vermiculite-type structure. The thickness of ultrathin nanosheets ranges from 8 to 15 nm and their lateral sizes are about 200 nm. Experimental results and DFT calculations indicate that zinc silicate possesses 2D ideal structures with rich active sites, high surface area, suitable VB and CB edges, making this material be efficient photocatalysts for the conversion of CO_2 into CO.

In 2019, Li et al. report a photo-thermal photocatalyst for the conversion of CO_2. They prepare a kind of oxygen-deficient MoO_{3-x} and apply it in photo-thermal reduction of CO_2 [127]. The LSPR effect of MoO_{3-x} induced by oxygen vacancies enables it to capture near-infrared photons. Additionally, oxygen vacancies can separate carriers efficiently, enhance CO_2 adsorption and reduce the barrier of CO_2 hydrogenation, confirmed by in situ FTIR and theoretical calculations. As a result, MoO_{3-x} possesses an enhanced photo-thermal synergistic activity for the reduction of CO_2 under simulated sunlight (UV–Vis-IR) irradiation. The best production rates of CO and CH_4 are 10.3 $\mu mol\ g^{-1}\ h^{-1}$ and 2.08 $\mu mol\ g^{-1}\ h^{-1}$, respectively.

A new strategy is developed by Wang et al., and they attempt to utilize the hydroxyls of oxyhydroxide photocatalyst to reduce CO_2 [128]. $CoGeO_2(OH)_2$ is chosen as a model photocatalyst to validate this strategy. It is true that $CoGeO_2(OH)_2$ can convert CO_2 to CH_4. Once irradiated by light, oxygen vacancies (OVs) and protons generate owing to the oxidation of lattice surface hydroxyls from $CoGeO_2(OH)_2$ by photo-generated holes. Both the generated oxygen vacancies (Lewis acid) and its original surface hydroxyls (Lewis base) can adsorb and activate CO_2, and then convert CO_2 into CH_4 with the help of protons. Fortunately, the surface lattice hydroxyls can be reused when exposed to an atmosphere containing water, and a continuous process of CO_2 reduction occurs. The continuous CO_2 reduction by self-repairing surface hydroxyls of photocatalysts may provide a new ideology for CO_2 conversion.

Graphene-included hybrid materials have been considered as promising photocatalysts owing to their unique photophysical properties. N-doped graphene/$Zn_{1.231}Ge_{0.689}N_{1.218}O_{0.782}$ (N-graphene/ZnGeON) hybrid composites have been synthesized using a two-step process [129], and could produce CH_4. The synergistic effect between ZnGeON and N-graphene promotes the photo-generated carriers transferring from ZnGeON to N-graphene, which play three roles: electron acceptor, mediator and co-photocatalyst. In the same year, a hybrid photocatalyst (Cu_2O/G) based on Cu_2O nanoparticles and graphene is employed as photocatalyst to convert CO_2 into CH_4 [130]. The CH_4 formation rate can reach up to 14.93 $mmol\ g^{-1}h^{-1}$ at 250 °C, an excellent yield among reported values below the Sabatier reaction temperature (>350 °C). Experimental evidence reveals that electrons transfer from Cu_2O/G photocatalyst to CO_2, leading to the generation of CH_4, which is the main reaction route. The effect of the temperature has been systematically studied, and the results display that heating is necessary for the releasing of byproduct H_2O. It should be mentioned that Cu_2O nanoparticles turn into Cu metals in the process, hampering its long stability.

A similar work is also reported by Mateo et. al. [131]. Two kinds of photocatalysts have been designed by them, and are constructed from NiO/Ni nanoparticles on defective GO (NiO/Ni-G) and Ni nanoparticles on silica-alumina, respectively. When the loading of Ni is 23 wt% in NiO/Ni-G, CH_4 formation rate can reach up to

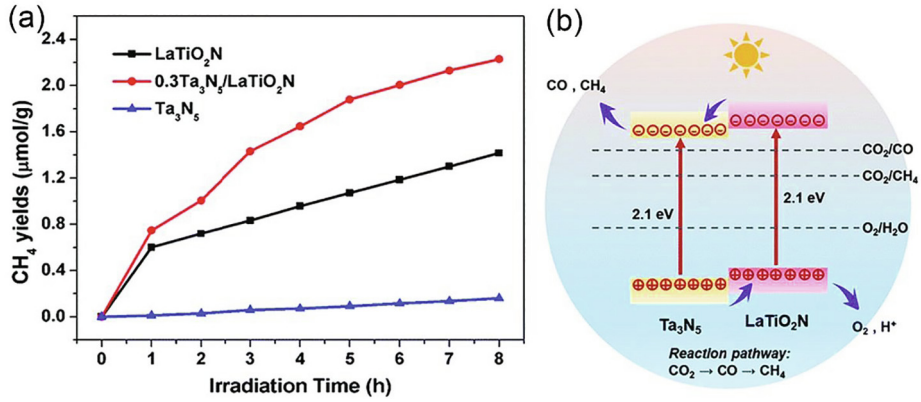

Fig. 18. (a) CH_4 yields of $LaTiO_2N$, Ta_3N_5, and $0.3Ta_3N_5/LaTiO_2N$ under visible light. (b) The possible reduction mechanism of $Ta_3N_5/LaTiO_2N$ (cited from Ref. [142]).

642 μmol g^{-1} h^{-1} at 200 °C, higher than Ni nanoparticles on silica-alumina. The photo-generated electrons transfer from NiO/Ni nanoparticles to GO sheets, which can enhance the charge separation. Electron donors (dimethylaniline, anisole and p-xylene) with different oxidation potentials are used to perform quenching experiments, and the experimental results agree well with the aforementioned mechanism. Temperature is also a key factor to achieve an excellent performance, and the high temperature can promote the release of formed water molecules, avoiding the deactivation of the photocatalyst. In order to prove the hypothesis, a control experiment is carried out. Under continuous flow, the deactivation of the photocatalyst is suppressed because flowing gases can take away the water molecules. Notably, NiO/Ni-G exhibits a CH_4 production rate of 244.8 μL h^{-1}. Later, a ternary halide Z-scheme photocatalyst α-Fe_2O_3/Amine-RGO/$CsPbBr_3$ has been constructed from $CsPbBr_3$ nanocrystals and amine-functionalized reduced graphene oxide-coated α-Fe_2O_3. Due to the rapid photo-generated electrons-holes separation as well as active redox capacity, this ternary photocatalyst has been demonstrated to possess an enhanced conversion of CO_2 to CH_4 (469.16 μmol g^{-1} in 40 h) [132].

Liang et al. have developed a simple, cheap and scalable method to promote the practical application of artificial photocatalysts [133]. Through a simple one-step spray drying, a composite photocatalyst SnO_2/eo-GO based on tin oxide (SnO_2) nanoparticles and edge-oxidized graphene oxide (eo-GO) sheets has been fabricated. As-synthesized photocatalyst possesses suitable electronic band structures and compositions, where SnO_2 colloids and eo-GO sheets pack together orderly. The best sample exhibits 28 times and 5 times enhancement in photocatalytic efficiency compared with SnO_2 and TiO_2 (P25), respectively. This scalable synthesis and simple experimental process are in favor of the practical applications of efficient photocatalysts.

Introducing metal into the lattice of a semiconductor can change its inherent electronic characteristics and band gap, resulting in improved photocatalytic activity. A series of achievements have been published recently. Ye group synthesizes an Rh and Au co-doped $SrTiO_3$ (STO), which produces syngas using low-cost CO_2 and H_2O as raw materials under visible-light irradiation [134]. The syngas yields are 22 and 153 times enhancement due to the synergistic effect between Rh and Au, compared to Au@STO and Rh@STO samples, respectively. In Rh and Au co-doped $SrTiO_3$, Au drives the process of syngas formation via the inter-band transition. Rh not only stores photoelectrons, but also promotes the formation of CH_4. Under the guidance of the above work, a Ge-substituted Zn_2TiO_4 photocatalyst $Zn_2Ti_{1-x}Ge_xO_4$ ($0 < x < 0.15$) is used for the photoreduction of CO_2 [135], and exhibits an excellent photocatalytic activity. $Zn_2Ti_{1-x}Ge_xO_4$ ($0 < x < 0.15$) exhibits a homogeneous inverted cubic spinel structure (Fd3m) and band gaps varying with Ge content. $Zn_2Ti_{1-x}Ge_xO_4$ not only can transfer CO_2 into CH_4 and CO, but also possesses a long stability (>60 h). Experimental evidences and theoretical calculations indicate the introduction of

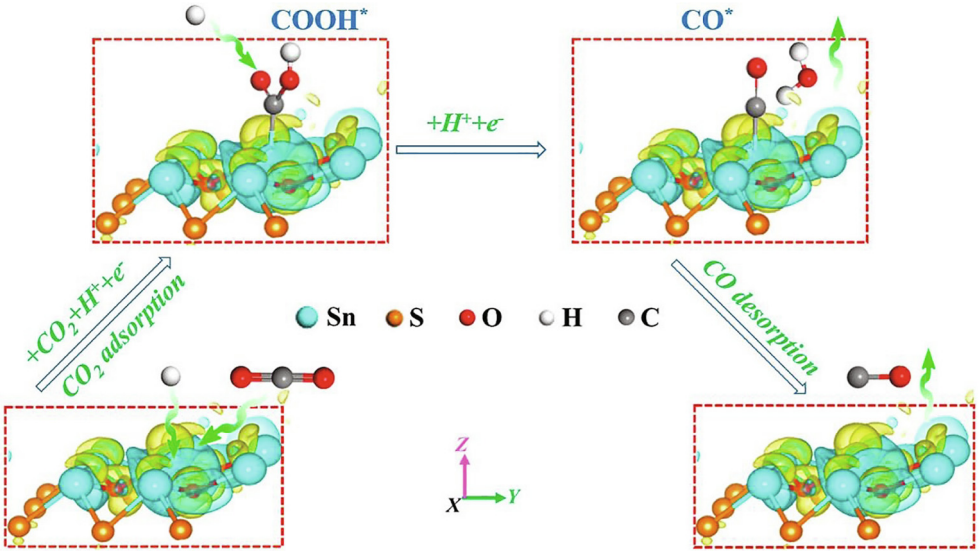

Fig. 19. Proposed photoreduction mechanism of mildly oxidized SnS_2 atomic layers (cited from Ref. [147]).

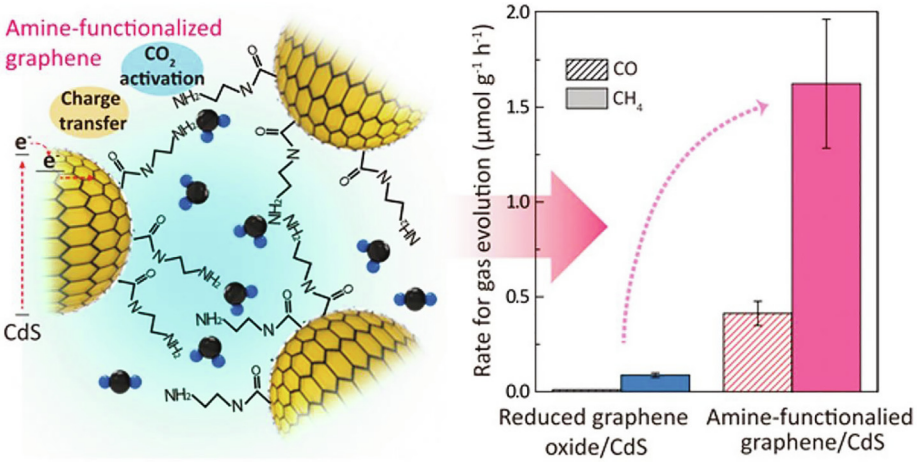

Fig. 20. Schematic representation of photocatalytic CO_2 conversion and the enhanced yield of CO and CH_4 produced by AG/CdS (cited from Ref. [149]).

Ge makes the CB and VB of $Zn_2Ti_{1-x}Ge_xO_4$ positively shifted, which can modulate the band gaps of $Zn_2Ti_{1-x}Ge_xO_4$. As a result, $Zn_2Ti_{1-x}Ge_xO_4$ shows the improved activity and excellent stability.

CeO_2 usually possesses wide band gap and poor light absorption, adverse to its photocatalytic activity [136,137]. The doping of heterogeneous atom may be an effective method to reduce its band gap and improve its photoreductive activity. Introducing Cu into CeO_{2-x} gives birth to Cu/CeO_{2-x} with rich O vacancies (Fig. 17) [136]. Cu/CeO_{2-x} shows a high efficient activity and can reduce CO_2 into CO and CH_4 (trace). The best yield of CO is 8.25 μmol g^{-1} under 5 h irradiation. Cu plays multiple roles: enhanced adsorption of UV–visible light, improved the electron-holes separation/transfer, extending the life of carriers, offering active sites and changed configurations of adsorbed CO_2. The analysis of Raman and XPS spectra reveal Cu can also stabilize O vacancies in CeO_{2-x} in the process of CO_2 reduction, which is closely related with the enhanced photocatalytic activity. Later, a similar work is reported [137]. Cr species are introduced into mesoporous CeO_2 to extend its spectral adsorption range (400–700 nm) and hinder the recombination of photo-induced electron-hole pairs. The optimal sample can produce CO and CH_4 with yields of 16.2 μmol g^{-1} and 10.1 μmol g^{-1} under 8 h irradiation.

Ding etc. carry out an interesting work, and investigate the effect of the distribution of Ag nanoparticles on the photocatalytic activity [138]. Two kinds of hybrid photocatalysts (i.e. Ag doped manganese oxides (Ag/HMO) and single-atom silver manganese photocatalysts (Ag-HMO)) have been synthesized and used to compare their performances. Both of them can produce CH_4, and yield produced by Ag-HMO is 0.61 mol mol^{-1} photocatalyst, 1.53 times higher than that of Ag/HMO. The single-atom Ag chains in Ag-HMO have three roles in improving the performances: driving the electron transferring from Ag to HMO, adsorbing visible light and activating adsorbed CO_2.

The recombination of photo-excited carriers is a great obstacle for efficient conversion of CO_2 [139]. A single crystal based on polar GaN:ZnO solid solution has been fabricated, and its polarization axis is in favor of separating photo-generated carriers efficiently, owing to the crystal lattice polarization. The crystal lattice polarization promotes that photo-generated electrons transfer horizontally to the $\{1\,0\,\bar{1}\,0\}$ facet through a 1D electron transport path along $[2\,\bar{1}\,\bar{1}\,0]$ in the {0001} facets of GaN:ZnO, which prevents recombination efficiently. DFT calculations also reveal the electron

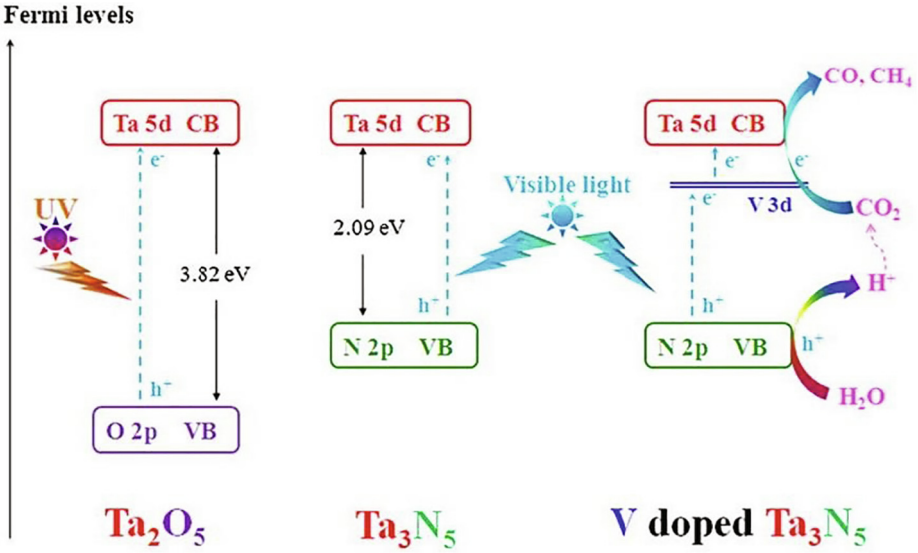

Fig. 21. A schematic diagram of role of V-dopants in enhanced separation of electron-hole pairs (cited from Ref. [151]).

transport1ation along the $\left[1\,0\,\bar{1}\,0\right]$ direction, resulting in carriers transporting to $\left\{1\,0\,\bar{1}\,0\right\}$ facet. The formation of porous nanoplates can shorten the hole-transfer distance, further reduce the recombination under the polarization field and enhance the performance. The finding reveals polarization may provide a new idea for designing new photocatalysts.

CdS is an excellent photocatalyst with a band gap of 2.42 eV. Lots of works have been used to improve its photocatalytic activity. Doping CdS with transition metal ions like Mn etc. may generate composite photocatalysts with improved activity. Gaikar group successfully loads CdS/Mn_2O_3 nanocomposites on porous anodic alumnia supports [140], and make it as a photocatalyst to evaluate the photocatalytic activity. CdS crystals grown on alumina generate a crumpled sheet, which can enhance the ability of light harvesting. The photocatalytic activity of CdS/Mn_2O_3 nanocomposite is carried out under direct sunlight, where various reflectors, such as flat mirrors, compound parabola, and Fresnel lens are used to tune solar radiation on the surface of photocatalysts. With the help of Fresnel lens, CdS/Mn_2O_3 nanocomposite exhibits the best photocatalytic activity. CdS/Mn_2O_3 nanocomposites can reduce CO_2 to C_2H_5OH and HCOOH with formation rates of 52.2 and 1392.3 μmol g^{-1} h^{-1}, respectively.

Employing $LaTiO_2N$ as the main photocatalyst, Yan group has made many pioneering contributions, and attempt to provide some ideas for solving the key problems encountered in photocatalytic CO_2 process. The activation of CO_2 and release of protons are two important half-reaction processes. Yan group plans to use a solid base to modify photocatalyst with defects, speeding up the two reaction processes [141]. Directed by this hypothesis, La_2O_3 is selected to dope $LaTiO_2N$ with oxygen vacancies, and the experimental result reveals that the modified photocatalyst can achieve two times increase in CH_4 yield. Two possible effects are found and listed below: i) basic sites O^{2-} in La_2O_3 enhance the adsorption of CO_2 in the form of CO_3^{2-} species, promoting the bending of O-C-O bond and reducing LUMO energy of CO_2 molecules; ii) the oxygen vacancies on $LaTiO_2N$ can convert H_2O to adsorbed OH, and release protons through reducing the barriers of water oxidation. One year later, they prepare another composite photocatalyst based on $LaTiO_2N$ with exposed (002) facet and Ta_3N_5 with dominant (020) facet [134], and employ it to find the clear mechanism toward photocatalytic product selectivity as well as reaction pathways. The observed intermediates indicate that the reaction pathway is as follows: $CO_2 \rightarrow COOH^* \rightarrow CO \rightarrow CH_x^* \rightarrow CH_4$. The selectivity of products is related to the electronegativity of adsorption sites, which influence the adsorption of CO onto the surface. The result reveals that CO_2 could be reduced to CH_4 and CO by $LaTiO_2N$ and Ta_3N_5, respectively (Fig. 18). The existence of La base metal sites in $LaTiO_2N$ endows it with strong ability for capturing CO, and prefers to carry out the hydrogenation reaction in the generation of CH_4. However, the weak adsorption of (020) surface from Ta_3N_5 toward CO can lead to the generation of main product CO, confirmed by theoretical calculations. In summary, this finding displays that the surface chemistry of a photocatalyst is a critical factor in the selectivity of product formation.

Additionally, the slow reaction kinetics induced by high activation barriers and low electron-hole pairs separation restrains the activity of CO_2 photoreduction. A synergistic strategy is employed to solve the obstacles [143]. Directed by the strategy, Ni/$LaTiO_2N$ photocatalyst is modified by KOH, and exhibits better performance compared with that of $LaTiO_2N$. The yields of CH_4 and CO produced by Ni/$LaTiO_2N$ are calculated to be 9.69 μmol g^{-1} and 0.31 μmol g^{-1}, respectively. The strategy effects are listed below: i) Schottky barrier between Ni and $LaTiO_2N$ accelerates the separation of electron-hole pairs; ii) the modified OH^- promotes the conversion of CO_2 into CO_3^{2-} species, speeding up the reaction kinetics and iii) the OH^- as hole's acceptor can oxidize H_2O and release protons. This study reveals that the design of new photocatalysts with different active sites to simultaneously activate CO_2 and H_2O might be a new strategy for efficient CO_2 conversion.

3.3. Metal chalcogenides and nitrides

Metal chalcogenides and nitrides have proved their applications in photocatalytic hydrogen production through water splitting. In recent years, metal chalcogenides and nitrides have found their roles in photoreduction of CO_2. These kinds of materials are similar to metal oxides, and their properties like crystal facet and surface morphology might also influence the photocatalytic performance.

The photocatalytic ability of a photocatalyst is closely correlated to its CB position. Zeng et al. have designed and synthesized a kind of heterogeneous photocatalyst $Zn_XCa_{1-X}In_2S_4$ based on trigonal $ZnIn_2S_4$ and cubic $CaIn_2S_4$ [146]. The as-synthesized $Zn_XCa_{1-X}In_2S_4$ solid solutions possess a more negative CB and improved charge separation efficiency. Benefiting from these advantages, all solid solutions show much better performances toward photoreduction of CO_2 under visible light (λ > 420 nm) irradiation. $Zn_{0.4}Ca_{0.6}In_2S_4$ with the most negative CB and highest charge-separation efficiency exhibits the highest CH_4 and CO evolution rates, superior to $ZnIn_2S_4$ and $CaIn_2S_4$.

Xie group has selected SnS_2 as a model photocatalyst to evaluate the influence of surface oxidation in the surface of metal disulfide on its photoreduction CO_2 performance [147]. They firstly prepare SnS_2 atomic layers and then oxidize part of their surfaces, creating SnS_2 atomic layers with different degrees of oxidation. In situ FTIR spectra confirm the main intermediate is $COOH^*$ radicals, whose formation is the rate-limiting step, demonstrated by the DFT calculations. The locally oxidized domains can act as active sites, promote the charge-carrier separation, and locate electrons around Sn atoms near O atoms, which can reduce the activation energy barriers via keeping $COOH^*$ intermediates stable (Fig. 19). As a result, the highest CO formation rate is 12.28 μmol g^{-1} h^{-1}. This work presents the relationship between oxidized sulfides and photoreduction CO_2 activity from the atomic level perspective.

A new Z-scheme photocatalyst (CZTS-ZnO) based Cu_2ZnSnS_4 (CZTS) and ZnO is firstly synthesized and applied to reduce CO_2 into CH_4 [148]. The catalytic performance is tuned by loading different amounts of CZTS on ZnO. It should be mentioned that the optimum CZTS-ZnO sample possesses an excellent the cyclic stability (five cycles). Moreover, the existence of Z-scheme heterojunction in CZTS-ZnO is confirmed by photo-luminescence (PL) tests and XPS spectra. Enhanced light absorption as well as effective separation of charges resulting from Z-scheme heterojunction leads to the improved performance.

Moreover, the introduction of amino groups may be an efficient strategy to enhance the efficiency of CO_2 photoreduction. Jung group firstly wraps CdS with rGO via an electrostatic reaction [149], and then integrates ethylenediamine with GO through covalent bonds, giving birth to amine-functionalized GO with few layers wrapped CdS (AG/CdS) (Fig. 20). Under visible light, the photocurrent and CO_2 adsorption ability of AG/CdS enhance remarkably. A CH_4 generation rate of AG/CdS is 2.84 μmol g^{-1} h^{-1} under visible light and CO_2 at 1 bar. It is very interesting that AG/CdS also exhibits the high photocatalytic activity at low pressure of CO_2 (0.1 bar) and the CH_4 formation rate can reach up to 1.62 μmol g^{-1} h^{-1}. It is notable that AG/CdS exhibits an excellent stability with a conversion rate of 87% after 10 cycles. Therefore, rGO functionalized with amino groups enhances the CO_2 adsorption ability and strengthens the absorption of visible light and charge transfer, leading to an enhanced performance.

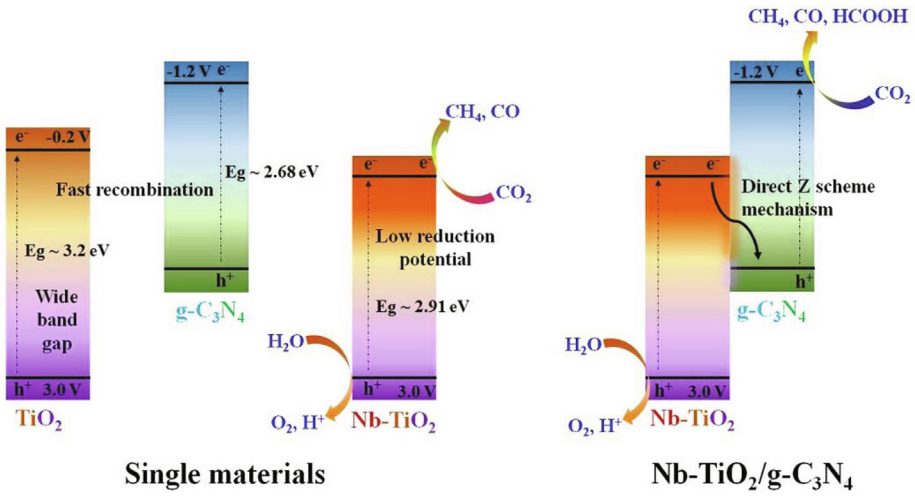

Fig. 22. Direct Z-scheme mechanism of Nb-TiO_2/g-C_3N_4 (cited from Ref. [165]).

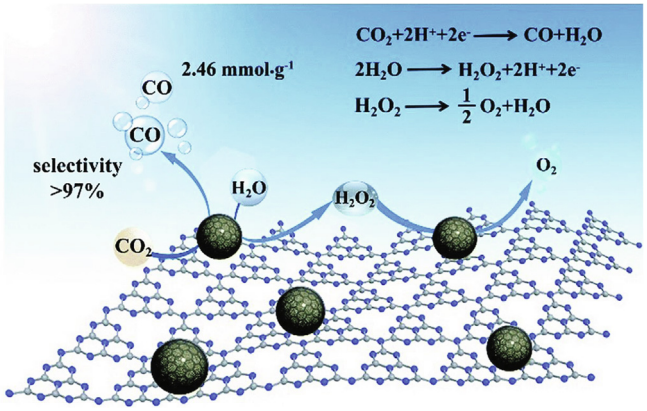

Fig. 23. The possible photocatalytic reduction process in C-TiO_{2-x}@g-C_3N_4 (cited from Ref. [167]).

Here, a Z-scheme g-C_3N_4/Sn_2S_3-diethylenetriamine (g-C_3N_4/Sn_2S_3-DETA) photocatalyst with porous characteristics has been synthesized [150], and can convert CO_2 into CH_4 and CH_3OH. This Z-scheme photocatalyst has a higher activity than bulk g-C_3N_4 or Sn_2S_3-DETA. CH_4 generation rate reaches up to 4.84 μmol g^{-1} h^{-1} and CH_3OH is 1.35 μmol g^{-1} h^{-1}. The enhanced performance is attributed to the Z-scheme structure of g-C_3N_4/Sn_2S_3-DETA, demonstrated by DFT calculation.

Recently, Ta-based materials with narrow band gap have been explored for CO_2 conversion. However, fast recombination of generated electrons and holes limits the improvement of their photocatalytic performance. Modified Ta_3N_5 has been synthesized to overcome the drawback and further enhance the photocatalytic efficiency [151]. So, V-doped Ta_3N_5 (V-Ta_3N_5) is synthesized and used to reduce CO_2 into valuable fuels. V-Ta_3N_5 can enhance visible light adsorption and decrease band gap energy, compared to Ta_2O_5, which can convert CO_2 into CO and CH_4 under visible light. The V dopants could be considered as an intermediate band (V 3d), and bridge the VB of N 2p and the CB of Ta 5d in the Ta_3N_5 (Fig. 21). Therefore, the doping of V hinders the recombination of electron-hole pairs of Ta_3N_5, leading to higher photocatalytic activity than that of Ta_3N_5. However, the formation of VN particles induced by the increase of V ratio also reduces the adsorption ability of light and decreases photocatalytic activity. The optimal ratio of V is 2 wt%. As a result, the highest production rates of CH_4, CO, O_2 and H_2 are 425, 236, 1003, and 56 μmol g^{-1} h^{-1}, respectively. One year later, Yan group employs metal Bi to modify n-type Ta_3N_5 to generate an ohmic junction photocatalyst Ta_3N_5/Bi via the pyrolysis of $BiTaO_4$ in an ammonia atmosphere [152]. Ta_3N_5/Bi can produce CH_4 with a yield of 4.52 μmol g^{-1}, which is about 5 times higher than that of pristine Ta_3N_5 (0.89 μmol g^{-1}). The cooperation of Ta_3N_5 and Bi drives the electrons transferring from Ta_3N_5 to Bi, enhancing the carrier separation efficiency. Ta_3N_5 can serve as the oxidation center and Bi as reduction center. The oxidation and reduction reactions take place simultaneously in two different components, which effectively restrain the decomposition of generated CH_4.

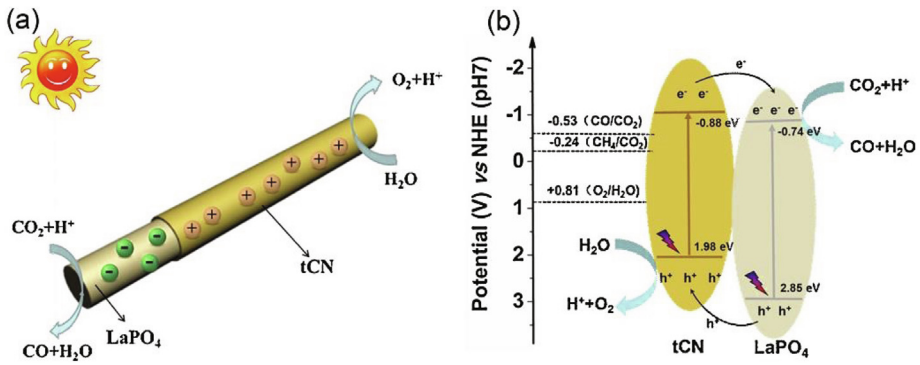

Fig. 24. Possible mechanisms of $LaPO_4$/g-C_3N_4 core–shell nanowires (cited from Ref. [168]).

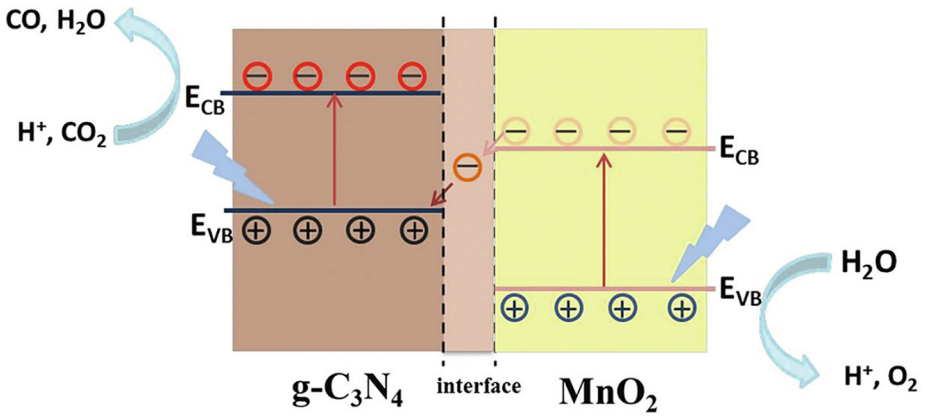

Fig. 25. Mechanism of photoreduction process in MnO_2/g-C_3N_4 (cited from Ref. [170]).

3.4. C_3N_4 based photocatalysts

Metal-free photocatalysts, for example, graphitic carbon nitride (g-C_3N_4) has been used to reduce CO_2 owing to its following features: easy and scale synthesis, narrow band gap (2.70 eV) and reasonable CB/VB edges (ca. −1.10/1.60 eV) [220,221]. However, its photocatalytic activity is poor because of the high charge recombination rate and low CO_2 adsorption ability. Naturally, a number of methods have been proposed to modify the nanostructure and surface chemical state of g-C_3N_4 to enhance its activity. Among various methods, new heterojunctions based on g-C_3N_4 and other materials (semiconductors etc.) may address the above issues.

3.4.1. Element doping with heteroatoms

Tremendous efforts have demonstrated that element doping and porous structure of g-C_3N_4 are beneficial for photocatalytic CO_2 conversion. With these in mind, several attempts have been carried out. A two-step treatment of bulk g-C_3N_4 gives birth to a kind of porous O-doped graphitic carbon nitride nanotubes (OCN-Tube) [160]. The diameters of interconnected multi-walled nanotubes in OCN-Tube range from 20 to 30 nm, and stack up together, generating hierarchically porous structures. OCN-Tube shows good photoreduction ability of CO_2 under visible light. The product is CH_3OH, and its production rate is 0.88 μmol g^{-1} h^{-1}, higher than bulk g-C_3N_4 (0.17 μmol g^{-1} h^{-1}). The hierarchical nanotube structure and O-doping are responsible for the high activity.

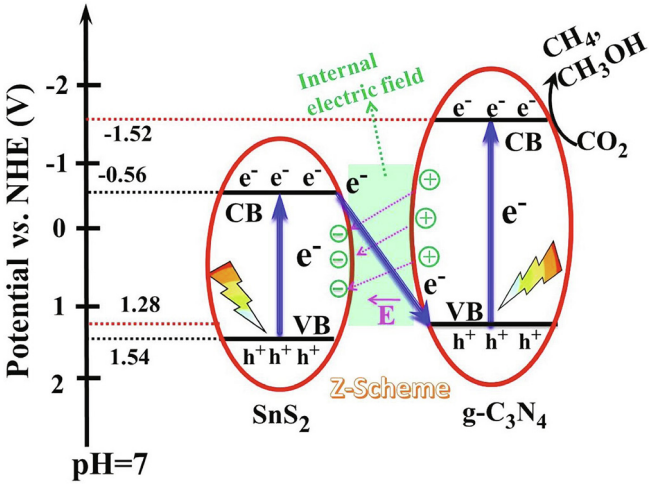

Fig. 26. Direct Z-scheme heterojunction in g-C_3N_4/SnS_2 induced by IEF (cited from Ref. [172]).

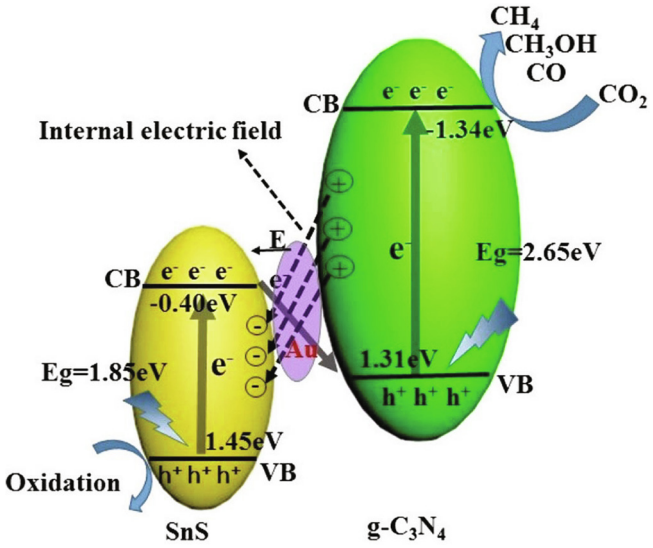

Fig. 27. Schematic diagrams of band structure and photo-generated carrier transfer of Au@g-C_3N_4/SnS irradiated by visible light (cited from Ref. [173]).

The hierarchical nanotube structure possesses higher specific surface area, enhanced light harvest and utilization efficiency, rich exposed active sites and smooth molecular diffusion pathway compared to bulk g-C_3N_4. The O-doping causes narrower band gap, enhanced CO_2 adsorption and activation and more efficient separation of charge carriers.

Inspired by the above work, mesoporous phosphorylated g-C_3N_4 (MPCN) has been obtained through treating bulk g-C_3N_4 (BCN) with concentrated phosphoric acid,[161] where PO_4^{3-} groups join the surface of this photocatalyst. Its photoreduction activity of CO_2 is higher than BCN coupling with the generation of CO and CH_4. Various characterizations, such as time-resolved photoluminescence and VB-XPS show that the Calvin cycle of PO_4^{3-} groups, fast carrier separation, large specific surface area, and high CB edge lead to the enhancement of the photocatalytic activity. The yields of CO and CH_4 can reach up to 7.7 and 14.6 μmol h^{-1}, respectively.

By means of NH_3-mediated thermal exfoliation approach, the texture of g-C_3N_4 ultra-thin nanosheets has been modified, and its surface has also been functionalized [162]. After treatment, the modified g-C_3N_4 photocatalyst possesses hierarchical structure, and has the following features: ultrathin nanosheets bringing large specific surface area and rich surface active sites as well as short charge carriers diffusion pathway; efficient charge carrier transfer

and separation; redox ability; hierarchical structures giving enhanced light adsorption, charges and molecules transfer pathway and surface amine enhancing CO_2 adsorption. The formation rates of CH_4 and CH_3OH are 10 times and 5 times than those of bulk g-C_3N_4. Hence texture modification and surface functionalization may be an efficient strategy for improving the photocatalytic activity of g-C_3N_4.

A series of Au-g-C_3N_4 (Au-CN) photocatalysts with different Au contents are synthesized [163]. The introduction of Au enhances the photoreduction activity of CO_2 obviously, and Au content can also affects the photoreduction activity of CO_2. When the mole ratio of Au/CN is 2%, the photocatalyst possesses the best catalytic activity, and the achieved yield of CH_4 is 9.1 times higher than that of pure CN after 2 h UV–Vis light irradiation. Additionally, the selectivity toward CH_4 also improves. This might be attributed to the plasmon resonance effect of Au that can promote the absorption ability of visible light, facilitate the generation of electron-hole pairs and then separate them efficiently.

3.4.2. Hybridization with metal oxides

The photoreduction efficiency of CO_2 can be further enhanced through designing the heterojunctions between g-C_3N_4 and other metal oxide based semiconductors with reasonable band edge. Up to now, many heterojunctions based g-C_3N_4 and TiO_2 have been discovered. The combination of g-C_3N_4 and Ag-TiO_2 (AgTi) gives birth to a kind of g-C_3N_4/Ag-TiO_2 (CN/AgTi) hybrid photocatalyst via a simple two-step experimental process (solvent evaporation and calcination process) [164]. The synergistic effect of g-C_3N_4, TiO_2 and Ag nanoparticles improves the conversion efficiency of CO_2. When the mass ratio of g-C_3N_4/AgTi is 8%, the yield of CH_4 and CO are 28 and 19 μmol g^{-1} within 3 h, respectively. The close interconnection between TiO_2 and g-C_3N_4 expands the light adsorption, transfers and separates photo-excited charges more effectively. The Ag nanoparticles on the surface of TiO_2 not only prevent the recombination of electron-hole pairs, but also concentrate energetic electrons on their surface. Naturally, rich energetic electrons on Ag nanoparticles take part in CO_2 reduction process, and improve the conversion activity of CO_2. Two years later, a similar work is discovered by Truc et al. [165]. They successfully dope Nb into TiO_2 lattice to decrease its band gap energy (Fig. 22). Then as-synthesized Nb-TiO_2 integrates with g-C_3N_4 to generate direct Z-scheme photocatalyst Nb-TiO_2/g-C_3N_4. The band gap energy of Nb-TiO_2 is 2.91 eV, lower than TiO_2 (3.2 eV). In direct Z-scheme photocatalyst Nb-TiO_2/g-C_3N_4, the generated electrons in the CB of Nb-TiO_2 together with produced holes in the VB of g-C_3N_4 keep electrons in the CB of g-C_3N_4 and holes in the VB of Nb-TiO_2 stable. Naturally, the system produces affluent electrons-hole pairs for CO_2 conversion. In addition, photo-excited electrons in the Nb-TiO_2/g-C_3N_4 transfer to the CB of g-C_3N_4, leading to a potential energy of 1.2 V, which could reduce CO_2 to several products (e.g., CH_4, CO and HCOOH).

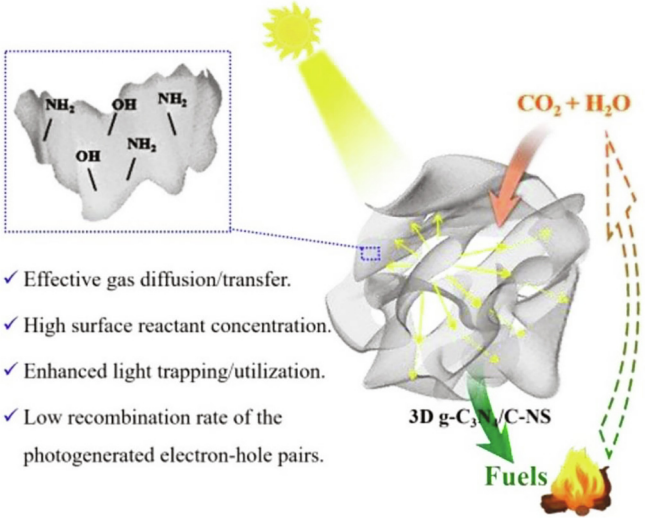

Fig. 28. The various advantages of g-C_3N_4/C-NS (cited from Ref. [177]).

Similarly, pyrolysis of urea in the presence of brookite TiO_2 quasi nanocube (BTN) gives birth to a new g-C_3N_4 nanodots (CNDs) doped brookite TiO_2 (BTN-CNDs) heterojunction [166], where the average size of g-C_3N_4 nanodots is about 2.8 nm. The heterojunction between BTN and CNDs exhibits an enhanced activity and selectivity for CH_4. The combination of BTN and CNDs brings the following advantages: i) uniformly distributed g-C_3N_4 nanodots can enhance the adsorption of reactants; ii) overlapping band structures and close contacts force the photoelectron transferring from CNDs to BTN and iii) enhanced hydroxyl/carbonate adsorption provides extra protons for CH_4 generation.

In another study, a two-step experimental process gives birth to C-TiO_{2-x}@g-C_3N_4 [167], which can reduce CO_2 to CO. Under visible-light irradiation, CO generation rate is about 12.30 mmol g^{-1} (204.96 μmol g^{-1} h^{-1}) within 60 h, the highest CO yield in the reported TiO_2-based materials. Various characterization methods reveal that C-TiO_{2-x}@g-C_3N_4 can adsorb photons and protons as well as CO_2 molecules. Additionally, this photocatalyst can separate charges and carry out a two-electron/two-step oxidative process (Fig. 23). The above factors result in the high activity.

CeO_2 has been widely used in many fields, owing to its catalytic activity induced by valence change between Ce^{3+} and Ce^{4+} [222,223]. Various CeO_2 based materials have been prepared until now. However, this kind of material has not been used for CO_2 photoreduction except one example. Li et al. synthesize mesostructured CeO_2/g-C_3N_4 nanocomposites as the photocatalyst [168], which can reduce CO_2 to CO and CH_4 irradiated by full spectrum light. A synergetic effect between m-CeO_2 and g-C_3N_4 exists and promotes the performance. Photo-generated electrons transfer from g-C_3N_4 to m-CeO_2, and are trapped by Ce^{4+}, preventing the recombination of electrons-holes. 0.590 μmol CO and 0.694 μmol CH_4 can generate in one hour. This work displays that m-CeO_2 may be a good co-photocatalyst.

$LaPO_4$ can serve as an effective photocatalyst for reducing CO_2 under the activation of high-pressure Hg lamp, due to its relatively wide band gap and poor adsorption of visible light [224]. To solve this problem, the combination of $LaPO_4$ with g-C_3N_4 may be a promising strategy. Therefore, a family of $LaPO_4$/g-C_3N_4 core–shell nanowires have been prepared through the loading of $LaPO_4$ nanorods into tubular g-C_3N_4 with the help of an in-situ hydrothermal growth method [169], and its photocatalytic activity toward CO_2 is evaluated. The coated g-C_3N_4 can enhance the light absorption and facilitate the efficient separation/transfer of charge carriers, leading to improved photocatalytic performance (Fig. 24) compared with individual g-C_3N_4 and $LaPO_4$. A maximum yield of CO is 0.433 μmol within 1 h irradiation, which might be attributed to the well-matched bands between $LaPO_4$ and g-C_3N_4.

The in-situ redox reaction between $KMnO_4$ and $MnSO_4{\cdot}H_2O$ anchored on the surface of g-C_3N_4 produces a new MnO_2/g-C_3N_4 heterojunction composite [170]. MnO_2 possesses a 2D δ-phase layered structure, and is bonded with the surface of g-C_3N_4 layers through -C-O- bonding. Notably, MnO_2/g-C_3N_4 photocatalyst can convert CO_2 into CO. The highest yield of CO is 9.6 μmol g^{-1} catalyzed by an optimized loading amount of MnO_2 under 1 h irradiation. MnO_2 shortens the band gap and enhances its light adsorption ability. Besides, the solid heterointerface between MnO_2 and g-C_3N_4 as well as matching band structure joins

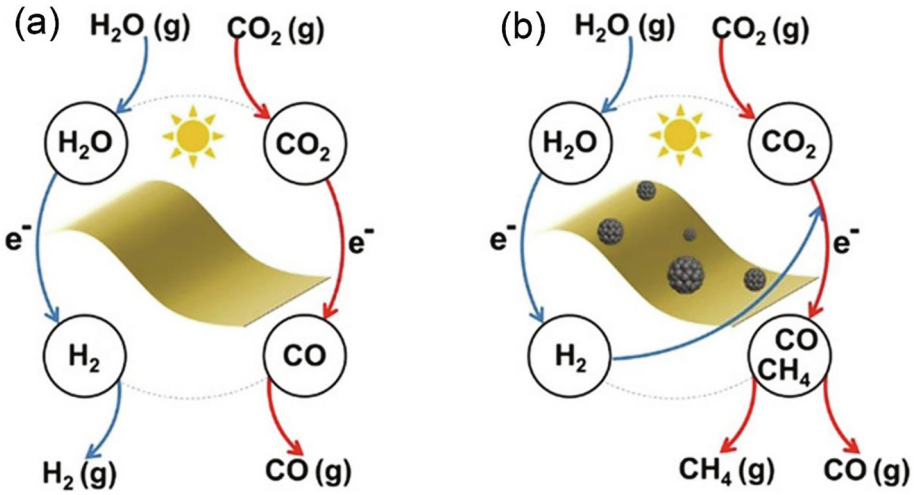

Fig. 29. Different photocatalytic pathways of (a) g-C_3N_4 and (b) CQDs/g-C_3N_4 in the presence of H_2O. The chemicals species adsorbed on the photocatalyst surface are marked using circles (cited from Ref. [179]).

together to efficiently separate the photo-induced carriers and improve its photocatalytic activity (Fig. 25).

Later, a ternary g-C_3N_4 based photocatalyst has been prepared using Ag_2CrO_4 as the photosensitizer and graphene oxide as co-photocatalyst [171]. This photocatalyst can convert CO_2 into CH_3OH and CH_4. The total formation rate is 1.03 μmol g^{-1}, and the turnover frequency is 0.30 h^{-1}, 2.3 times higher than that of original g-C_3N_4. The light absorption ability, CO_2 adsorption and charge separation is enhanced owing to the well-matched band structure and reasonable loading ratio of Ag_2CrO_4. The formation of the direct Z-scheme heterojunction is confirmed by the radical scavenging experiments and DFT calculations, which can promote the photocatalytic reaction through facilitating the charge separation and improving the redox ability. Furthermore, graphene oxide as co-photocatalyst not only accepts electrons, promotes the charge transfer, but also offers rich CO_2 adsorption and catalytic active sites.

3.4.3. Hybridization with metal sulfides

The construction of direct Z-scheme heterojunction is an available approach for improving the photocatalytic CO_2 reduction efficiency. Using $SnCl_4{\cdot}5H_2O$, L-cysteine and g-C_3N_4 as precursors, a new type of direct Z-scheme g-C_3N_4/SnS_2 heterojunction is constructed through a facile hydrothermal method [172], in which SnS_2 quantum dots with sizes of 2–3 nm are decorated on the surface of g-C_3N_4. XPS spectra and DFT calculation confirm that electrons transfer from g-C_3N_4 to SnS_2, forming interfacial internal electric fields (IEF) between them. Light irradiation induces the occurrence of Z-scheme charge transfer, where the electrons lock in SnS_2, and the holes locate in g-C_3N_4, improving photo-induced electron utilization efficiency in g-C_3N_4. The IEF-induced direct Z-scheme makes g-C_3N_4/SnS_2 to exhibit high photocatalytic performance. The appearance of intermediate HCOOH is confirmed by the in situ FTIR spectra, revealing that the product results from g-C_3N_4, conversely demonstrating the existence of Z-scheme configuration in the g-C_3N_4/SnS_2 system (Fig. 26).

Based on the same precursor, a kind of new IEF-induced Z-scheme photocatalyst Au@g-C_3N_4/SnS with yolk-shell structure is prepared using a simple template method [173]. In the Z-scheme photocatalysts, they exhibit advantages like: i) the L-cysteine with amine groups anchor on the surface of g-C_3N_4 and adsorb more CO_2 molecules; ii) the unique yolk-shell structure can increase light utilization efficiency and surface areas and iii) noble metal co-photocatalysts uniformly disperse on the surface of g-C_3N_4. Summarily, the Z-scheme structure, high CO_2 adsorption, large surface area and noble metal effect contribute to the enhanced light utilization efficiency and boosted separation and transfer of interfacial charges. Therefore, the excellent activity for CO_2 is found. Three kinds of products (CH_4, CH_3OH and CO) are observed, and their highest yields are 3.8, 5.3, and 17.1 μmol g^{-1} respectively (Fig. 27).

3.4.4. Hybridization with carbon based materials

The integration of g-C_3N_4 with carbon based materials not only increases the absorption of extra light, but also improves the conductivity of whole material, which are beneficial for CO_2 conversion. Pt co-photocatalyst is successfully doped into pre-synthesized Boron carbide/graphitic carbon nitride (B_4C/g-C_3N_4) p-n heterojunction photocatalyst by Zhang et al. [174]. An internal electric field is constructed by coupling p-type B_4C with n-type g-C_3N_4. Firstly, B_4C enhances the light harvesting ability, and promotes the formation of an internal electric field with g-C_3N_4, which can separate photo-excited electron-hole pairs more efficiently. Secondly, Pt can not only trap photo-excited electrons and transfer photoinduced charges, but also dissociate H_2, promoting the formation of CH_4 under irradiation. It is noteworthy that the CH_4 evolution rate depends on Pt contents. When B_4C and Pt mass fractions are 1/6 and 0.8%, respectively, the formation rate reaches maximum, 5 and 7 times higher than those of g-C_3N_4 and B_4C, respectively.

A reduced graphene oxide based aerogel contains three components (Pd, g-C_3N_4 and reduced graphene oxide) has been synthesized [175], and defined as Pd-g-C_3N_4/RGOA. In Pd-g-C_3N_4/RGOA, g-C_3N_4 disperses on the surface of RGOA uniformly, and connect RGOA together by means of 2D-2D π-π conjugated interaction. Materials with such packing structure can adsorb more CO_2, utilize more light energy, and separate charge carriers more efficiently. Pd not only accelerates the electron-hole pair separation, but also promotes the formation of CH_4. Finally, Pd-g-C_3N_4/RGOA exhibits a CH_4 generation rate of 6.4 μmol g^{-1} h^{-1}.

The pyrolysis of melamine and natural soybean oil gives birth to graphitic carbon nitride and carbon (H-g-C_3N_4/C) hybrid photocatalyst [176], which possesses different carbon contents. Naturally, the structure of H-g-C_3N_4/C and photoreduction of CO_2 activity are tuned by the carbon content. Compared to bulk g-C_3N_4, the textural property and conductivity of H-g-C_3N_4/C improve significantly, which promote the improvement of photoreduction activity of CO_2 with H_2O. The highest yields of CO and CH_4 are

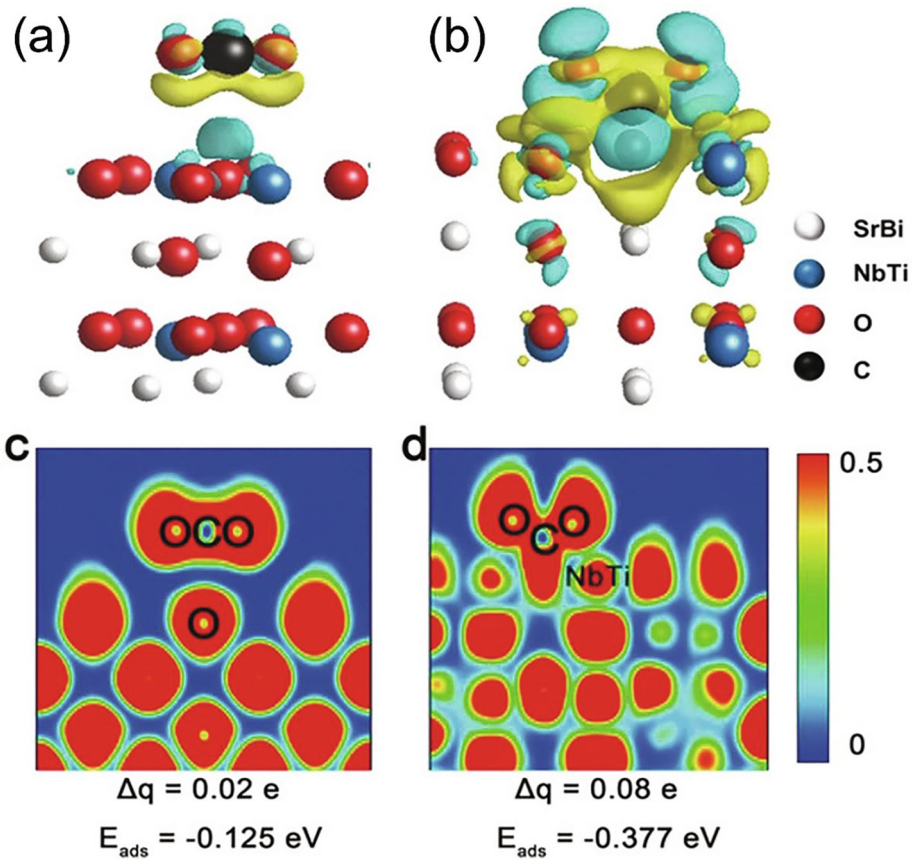

Fig. 30. Charge differences in (a) $Sr_2Bi_2Nb_2TiO_{12}$ and (b) $Sr_2Bi_2Nb_2TiO_{12}$ with OVs after CO_2 adsorption. Blue and yellow parts stand for charge accumulation and depletion in electronic location function (ELF) of (c) $Sr_2Bi_2Nb_2TiO_{12}$ and (d) $Sr_2Bi_2Nb_2TiO_{12}$ with OVs (cited from Ref. [185]).

22.60 μmol g^{-1} and 12.5 μmol g^{-1}, respectively. Employing the same precursor (melamine and natural soybean oil), the use of another different synthetic method leads to a completely different structure [177]. By means of a two-step experimental process (pyrolysis and carbothermal activation), 3D porous nanosheets based on g-C_3N_4 and carbon nanosheets are synthesized, and defined as g-C_3N_4/C-NS. g-C_3N_4/C-NS possesses crumpled morphology and hierarchical mesostructure, and exhibits high surface area and large pore volume. The structural advantages of g-C_3N_4/C-NS make it to be excellent photocatalyst. The yields of CO and CH_4 can reach up to 229 and 112 μmol g^{-1} under 7 h irradiation, respectively, about 25-times higher than that of bulk g-C_3N_4. The unique structure can improve the light adsorption/utilization, enhance CO_2 adsorption and separation of photo-generated electron-hole pairs, which results in the excellent photocatalytic performance (Fig. 28).

Carbon quantum dots (CQDs) with sp^2-hybridized carbon show unique features, for example, variable optical absorption. Recent advances display the introduction of CQDs can enhance the absorption of visible-light, separation ability of charge-carriers as well as photocatalytic activity [225]. Therefore, incorporation of CQDs is a reliable method applied in the enhancement of CO_2 conversion. Carbon nanodot (CND) is doped into protonated g-C_3N_4 (pCN), generating a heterojunction photocatalyst (CND/pCN) [178], where CND with average size of 4.4 nm disperse uniformly on the surface of pCN. When the CND content is 3 wt%, CND/pCN possesses the highest catalytic activity under simulated solar light. CH_4 and CO are the products in this process. The yields of CH_4 and CO are 29.23 and 58.82 μmol g^{-1} after 10 h under visible light irradiation, respectively. Additionally, under simulated solar light, the yields of CH_4 and CO can reach up to 37.06 μmol g^{-1} and 68.80 μmol g^{-1}, respectively. Furthermore, after four cycles, this sample can maintain high stability and durability without significant decrease of activity. This synergy between pCN and CNDs allows photoexcited electrons transferring from pCN to CND via heterojunction interfaces, demonstrated by various experimental characterizations. The data obtained from DFT results match well with our experimental results. The work function of CNDs is 5.56 eV, larger than that of pCN (4.66 eV), which suggest the electrons transfer from the CB of pCN to CNDs, preventing the recombination of electron-hole pairs.

Adopting the same strategy, nonpolar CQDs are successfully doped onto g-C_3N_4, giving birth to a heterojunction photocatalyst (CQDs/g-C_3N_4) [179]. Commonly, CQDs can enhance light absorption through reducing the band gap and absorbing electrons, and improve the separation efficiency of photocarriers. In this work, nonpolar CQDs also play other roles: enhancing CO_2 adsorption, restraining H_2 production, and changing the reduction path of CO_2 to generate CH_4 (Fig. 29). Consequently, CQDs/g-C_3N_4 only produces CO and CH_4, six times higher than that of original g-C_3N_4. Nonpolar surface modification is demonstrated to be a promising method for enhancing the CO_2 photoreduction performance.

It is a good choice that immobilizing the photocatalyst into polymeric supports generate a kind of membrane photocatalyst. The membrane photocatalyst shows several advantages: more photocatalytic sites exposed to light and reactants, avoiding photocatalyst aggregation, and ease of recovery. Barbieri group prepares an exfoliated C_3N_4 doped Nafion matrix to investigate its photocatalytic behavior in a continuous photocatalytic reactor [180]. The effects of some experimental factors, such as H_2O/CO_2 feed molar

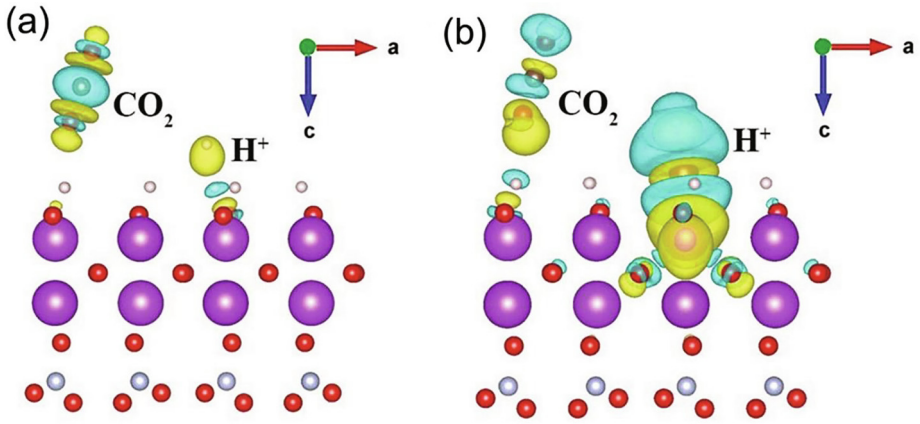

Fig. 31. Charge differences of BON (a) and BON-Br (b) after absorbing CO_2 and protons (yellow part representing charge accumulation and blue part representing depletion) (cited from Ref. [191]).

ratio and contact time are studied in detail. The species of products influenced by the above factors are also examined. The change in weight ratios for carbon/photocatalyst results in various photocatalyst production rate ranging from 5 to 47.6 μmol g^{-1} h^{-1}. The experimental result shows that a short contact time is beneficial for the generation of alcohols, while long contact time leads to the partial oxidation of alcohols and generation of HCHO. Additionally, a low H_2O/CO_2 feed molar ratio prefers to produce HCHO. When the H_2O/CO_2 feed molar ratio is 0.5, a rate of 27 μmol g^{-1} h^{-1} is obtained. When the feed molar ratio of H_2O/CO_2 is 5, the total production rate of 32.8 μmol g^{-1} h^{-1} with MeOH and EtOH selectivity of 54.6% and 45.4%, respectively. Similarly, Wang et al. propose a new idea that advanced light management is utilized to tune the photocatalytic activity of CO_2 [181]. g-C_3N_4 photocatalyst is selected as the substrate, and biodegradable transparent paper possessing an excellent light diffusivity is anchored on the surface of g-C_3N_4. It is worth mentioning that the transparent paper with incident angle-independent optical properties can manage light effectively. Fortunately, as-synthesized photocatalyst shows a higher photocatalytic activity than bare g-C_3N_4 irradiated by visible light. The enhanced catalytic activity is attributed to the effective light scattering and increased light absorption within the photocatalyst. The study provides another perspective for tuning photocatalytic activity via light management.

3.5. Bismuth based photocatalysts

Over the past few years, Bi-based photocatalysts have been proved to be an excellent photocatalyst by themselves owing to reasonable band gaps. Bi-based photocatalysts mainly contain BiOX with sillén-structure (X = Cl, Br, I), Bi_2MO_6 (M = Mo, W) with aurivillius structure, $BiVO_4$ with scheelite-structure, and so on [226–232]. If Bi-based photocatalysts are used in photoreduction of CO_2, their CB positions should be elevated. Besides, many approaches, for example, surface modification or heterojunctions have been applied to improve their charge separation efficiency and enhance the CO_2 adsorption ability. Naturally, abundant Bi-based photocatalysts have been prepared according to the above approaches.

BiOX (X = Cl, Br, I) semiconductors with layered structures as an important component of photocatalyts, have been extensively investigated in photocatalysis. In this study, Ye et al. employ thickness-ultrathin and bismuth-rich methods to improve the performance of BiOX [182]. Among them, $Bi_4O_5Br_2$ microspheres are constructed from ultrathin nanosheets (thickness of about 3.7 nm), much thinner than normal BiOBr nanosheets (65 nm). Benefiting from these two advantages, as-synthesized $Bi_4O_5Br_2$ microsphere exhibits a higher photocatalytic activity of CO_2 than BiOBr or ultrathin BiOBr. Furthermore, an interesting experimental phenomenon is presented here. Thickness-ultrathin method prefers to promote CO generation, while bismuth-rich method enhances the CH_4 generation. These results could help researchers to understand the mechanism of enhanced performances of layered bismuth-rich BiOX photocatalyst.

Oxygen vacancies strategy has been demonstrated to be an efficient approach to improve the performance of various photocatalysts. The strategy is also applicable to bismuth-based photocatalysts. Oxygen-deficient BiOBr with rich oxygen vacancies is prepared through a highly facile ethylene glycol-assisted solvothermal method [183]. Oxygen vacancies play dual roles in photocatalytic CO_2 reduction: i) adsorb and activate CO_2 and ii) separate electron-hole pairs and hamper the recombination of charge carriers. Naturally, as-prepared sample exhibits an enhanced activity, and the yield of CH_4 is 43.3 and 5.7 times higher than those of pristine BiOBr and TiO_2 (P25), respectively. Additionally, oxygen-deficient BiOBr possesses a long term durability (>50 h) under simulated solar light. After the introduction of surface oxygen vacancies, $Bi_{24}O_{31}Cl_{10}$ exhibits a better CO_2 photoreduction activity [184]. The presence of oxygen vacancies produces more carriers and enhances the separation of them. In situ FTIR analysis is used to detect the intermediate COOH*. DFT calculations reveal that oxygen vacancies can adsorb and activate CO_2, facilitating the formation of COOH*. At the same year, Aurivillius-phase $Sr_2Bi_2Nb_2TiO_{12}$ with surface oxygen vacancies (OVs) has been prepared to address the following drawbacks [185]: poor light absorption, slow charge separation and inactive surface reactive sites. In this photocatalyst, the existence of oxygen vacancies expands the light absorption range, and separates photo-induced charge carriers fast. Additionally, oxygen vacancies also adsorb more CO_2 molecules and activate them. In the gas–solid reaction system, OVs-abundant $Sr_2Bi_2Nb_2TiO_{12}$ nanosheets can produce CO with a rate of 17.11 μmol g^{-1} h^{-1}. Experimental and theoretical results reveal OVs play a key role in the performance of this photocatalyst. In theoretical calculation, the charge difference distribution as well as the electronic location function reveal that there exist stronger and more covalent interactions between the OV sites and CO_2 molecules, indicating OVs can adsorb and activate CO_2 (Fig. 30).

Recently, the effect of halogen element type and surface oxygen vacancy on photocatalytic performances has been investigated in pure Bismuth oxyhalide (BiOX, where X = F, CI, Br and I) based photocatalysts. Among all photocatalysts, BiOBr exhibits the best

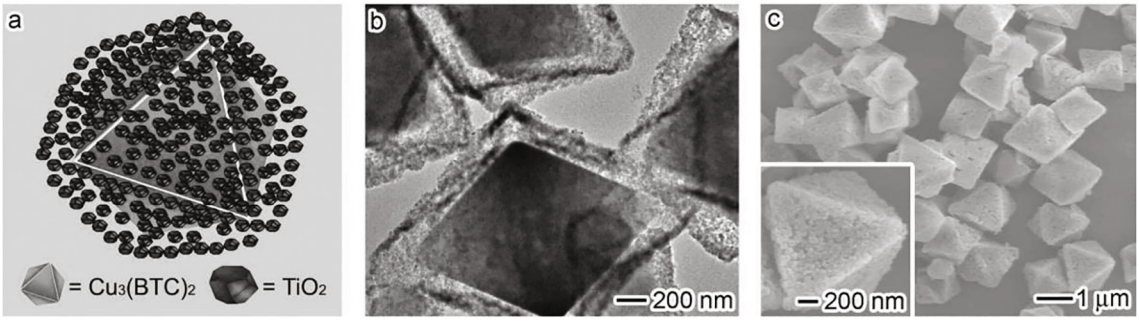

Fig. 32. (a) Structural diagram of $Cu_3(BTC)_2$@TiO_2, (b) TEM and (c) SEM images revealing the real structure and surface morphology of as-synthesized $Cu_3(BTC)_2$@TiO_2 (cited from Ref. [197]).

CO_2 photoreduction ability with a formation rate of CO (21.6 μmol g^{-1} h^{-1}) and CH_4 (1.2 μmol g^{-1} h^{-1}), respectively. Various characterization methods including isotopic tracing method, EPR, in-situ FTIR, positron annihilation lifetime (PAL) spectra as well as DFT calculation are used to explain the photoreduction activity of BiOX [186].

The combination of bismuth based photocatalysts with different materials is an effective method to enhance the photocatalytic activity, because composite photocatalysts can combine the advantages of each component. A family of Z-scheme BiOI/g-C_3N_4 photocatalysts is prepared, and their photocatalytic CO_2 activity is evaluated under visible light irradiation ($\lambda > 400$ nm) [187]. As expected, BiOI/g-C_3N_4 exhibits better performances than pure g-C_3N_4 and BiOI. The successful detection of the intermediates I_3^- ions identifies the pathway of charge transfer and the generation of Z-scheme charge transfer mode. Therefore, the appearance of **.**OH and H_2O_2, combining with the final products further clarifies the reaction mechanism. Similarly, g-C_3N_4/$Bi_4O_5I_2$ heterojunction has been assembled [188]. Introduction of g-C_3N_4 does effectively enhance photocatalytic activity through changing surface topography and electronic conductivity of this heterojunction. The photocatalytic results reveal that g-C_3N_4/$Bi_4O_5I_2$ heterojunction possesses higher activity than pure g-C_3N_4 and $Bi_4O_5I_2$. When the ratio of g-C_3N_4 and $Bi_4O_5I_2$ reaches 1.0 mol %, the photocatalytic activity of g-C_3N_4/$Bi_4O_5I_2$ is the highest, and the generation rate of CO can reach up to 45.6 μmol g^{-1} h^{-1}. The successful detection of intermediates I_3^-/I^-, superoxide radicals (O_2^-) and hydroxyl radicals (**.**OH), which confirms the existence of Z-scheme charge transfer mode in g-C_3N_4/$Bi_4O_5I_2$.

Construction of Z-scheme photocatalysts is really a good choice used for photoreduction CO_2 [189]. Monoclinic bismuth vanadate (m-$BiVO_4$) exhibits low photoreduction activity of CO_2 due to its low CB potential and short electron transfer pathway. CdS is selected to be doped into $BiVO_4$ nanosheets with controlled thickness to solve the above problem. Naturally, a series of CdS/$BiVO_4$ nanocomposites have been synthesized and evaluated their photocatalytic performance. The photocatalyst can convert CO_2 into CO and CH_4. The results show that the doped photocatalyst possesses more efficient activity than CdS and $BiVO_4$, and the thickness of doped photocatalyst influences the yields of CH_4 and CO. The thinner in nanosheet thickness, the higher activity can be achieved. The yields of CH_4 and CO (8.73 and 1.95 μmol g^{-1}) catalyzed by CdS/$BiVO_4$ with 15–30 nm thickness are higher than those of CdS/$BiVO_4$ with 55–75 nm thickness (2.98 and 1.31 μmol g^{-1}) after 5 h irradiation, respectively. The reasonable band structure of CdS and $BiVO_4$ as well as Z-scheme charge transfer mode is responsible for the improved activity.

Most of the used photocatalysts could harvest ultraviolet (UV) and/or visible (Vis) light. However, near-infrared (NIR) region is rarely explored in the spectrum. In this study, ultrathin Bi_2WO_6 nanosheets (UBW) are doped by CQDs [190], and have been used as an efficient photocatalyst (CQDs/UBW) under Vis-NIR broad spectrum, which can produce CH_4. The combination of Bi_2WO_6 nanosheets and CQDs makes the scope of absorption spectra of CQDs/UBW extend to the NIR region. When the CQD content is 1 wt%, the production rate of CH_4 is 9.5- and 3.1-times higher than pristine Bi_2WO_6 nanoplatelets (PBW) and bare UBW under visible light irradiation. The synergistic effects of CQDs and Bi_2WO_6 nanosheets are listed below: i) exposed {0 0 1} facets in ultrathin nanostructures; ii) appropriate band structure of UBW or CQDs and iii) adsorbing photo-generated electrons by CQDs and limited recombination of charge carriers.

The fast recombination of charge carriers and low activity of catalytic sites are two major problems, which limit the CO_2 photoreduction activity. Surface halogenation strategy is employed to address the above two problems using $Bi_2O_2(OH)(NO_3)$ (BON) as a substrate [191]. A series of Sillén-related layer-structured photocatalyst BON-X (X = Cl, Br and I) are prepared, where the surface halogen ions replace part of surface hydroxyls and coordinate to Bi atoms. The experimental and theoretical results reveal the surface halogen ions play dual roles in CO_2 photoreduction process: separating charges and activating the adjacent OH, which can promote the CO_2 and proton adsorption as well as CO_2 conversion. Surface hydroxyls can adsorb more CO_2 molecules and protons and are in favor of CO_2 conversion, demonstrated by DFT calculations. Theoretical results reveal strong charge interactions between CO_2 and OH, which make C═O bonds of CO_2 close to photocatalyst surface in generating intermediates *COOH to improve the CO_2 photoreduction activity (Fig. 31). Among these photocatalysts, BON-Br shows the highest CO production rate (8.12 μmol g^{-1} h^{-1}).

3.6. MOFs derived photocatalysts

Metal-organic frameworks (MOFs) have emerged as an excellent platform for realizing solar energy conversion due to their diverse and tunable structures and versatile host–guest chemistry. Metal clusters are usually considered as active sites for CO_2 reduction and organic linkers can harvest light, generate excited electrons and provide pathways for transfer of excited electrons to metal centers. Depending on their unique advantages, MOFs have been tried to reduce CO_2. For example, a Zn MOF (Zn/PMOF) based on tetrakis (4-carboxy phenyl) porphyrin (TCPP) can convert CO_2 into CH_4 under UV and visible light [185], and its generation rate is 10.43 μmol within 4 h. Besides, Zn/PMOF possesses good stability and reusability. Recently, a pyrazolyl porphyrinic based Ni-MOF (PCN-601) can serve as a superior photocatalyst for CO_2 reduction with H_2O vapor. Its robust coordination spheres of pyrazolyl groups as well as Ni-oxoclusters ensure PCN-601 possesses appreciate energy bands and fast photo-excited electron transfers. Finally, the CH_4 production rate of PCN-601 is 10.1 μmol g^{-1} h^{-1},

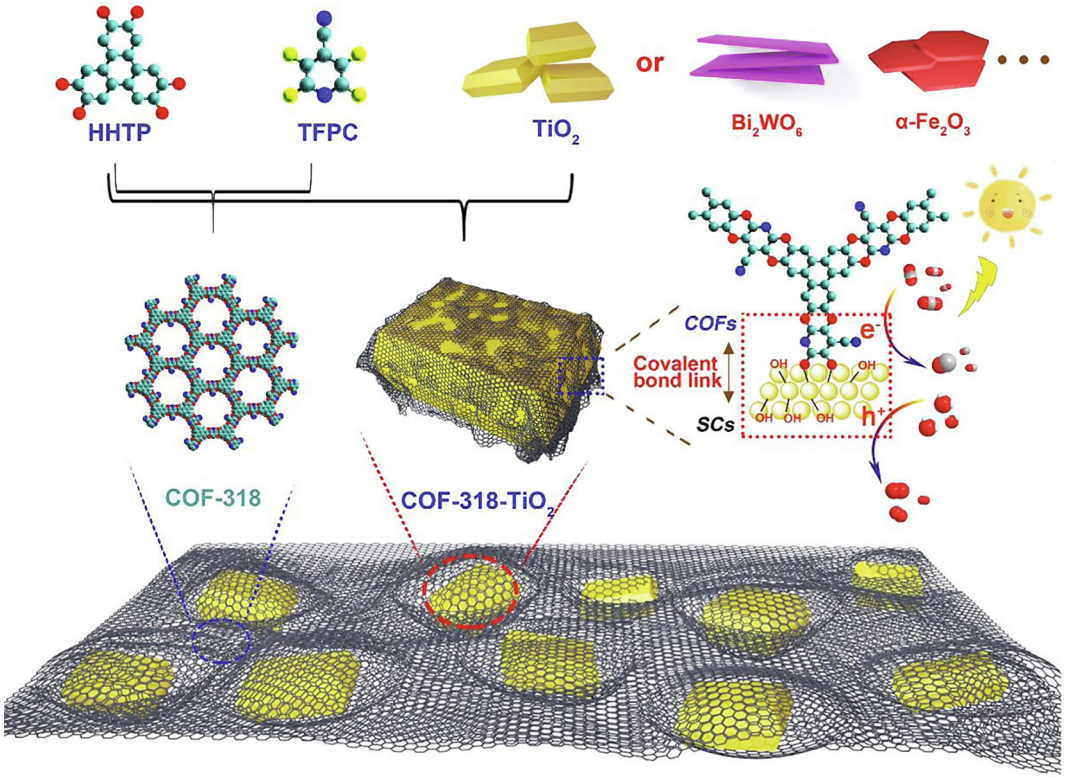

Fig. 33. Schematic diagram of the synthesis of COF-318-semiconductors via the covalent connection of COF-318 and semiconductors (cited from Ref. [211]).

exceeding those of carboxylate porphyrin based MOFs [194]. Previously reported examples indicate that the performances of individual MOFs used for CO_2 reduction are usually not very well except those constructed from porphyrin ligands. Naturally, a popular strategy is integrating MOFs with other functional materials to create new composites, which could possess better photocatalytic performances than those of individual component. Besides, some famous MOFs, for example, ZIF-8 and HKUST-1have also been used as sacrifice templates to prepare new photocatalysts.

Porous g-C_3N_4 nanotubes have been synthesized to overcome its intrinsic drawbacks, such as light harvesting, redox potential, and charge separation efficiency. To solve it, ZIF-8 nanocrystallines are combined with tubular g-C_3N_4 (TCN) to generate a kind of composite photocatalyst (TCN/ZIF-8) with the integrated advantages of each component (high CO_2 adsorption and visible-light adsorption) [195]. Well-designed photocatalysts not only expand light absorption and redox potential and separate charges efficiently, but also capture more CO_2. As a result, TCN/ZIF-8 photocatalyst can reduce CO_2 to CH_3OH, and a formation rate of 0.75 μmol g^{-1} h^{-1} is obtained under mild reaction condition. Meanwhile, the disadvantage is that low conductivity of ZIF-8 impairs the charge transfer ability of TCN/ZIF-8 photocatalyst, which limits the improvement of photocatalytic performance. Inspired by the above work, one year later, ZIFs are employed as a host to load halide perovskite (drawbacks like low CO_2 adsorption and poor stability) to prepare a composite photocatalyst [196]. A simple in situ synthetic method is used to coat zinc/cobalt-based ZIFs on the surface of $CsPbBr_3$ quantum dots, giving birth to $CsPbBr_3$@ZIF with core–shell structure. $CsPbBr_3$@ZIF possesses enhanced moisture stability, CO_2 adsorption ability, and high efficient charge separation. Additionally, Co centers in ZIF-67 can not only activate CO_2 molecules, but also speed up the charge separation. Notably, $CsPbBr_3$@ZIF exhibits an enhanced catalytic activity toward CO_2 than that of $CsPbBr_3$.

Integrating semiconductors with MOFs may create a hybrid photocatalyst with high CO_2 photoreduction efficiency, which possesses the following features: high surface area and high adsorption capability from MOFs, and good photocatalytic activity from semiconductors. So, Li et al. employ a hydrolysis method to coat TiO_2 on the pre-synthesized $Cu_3(BTC)_2$ nanocrystals (BTC = Trimesic Acid), generating $Cu_3(BTC)_2$@TiO_2 with core–shell structures (Fig. 32) [197]. Benefiting from this special structure, the photogenerated electrons transfer from TiO_2 to $Cu_3(BTC)_2$, resulting in efficient charge separation in TiO_2 and capture of energetic electrons by CO_2 adsorbed in $Cu_3(BTC)_2$. Commonly, CO_2 is easily adsorbed in $Cu_3(BTC)_2$, and reduced into CH_4. Above all, $Cu_3(BTC)_2$@TiO_2 displays enhanced activity and selectivity. It is proposed that the present work will provide a new idea for applying MOFs in photoreduction CO_2.

Different from the above work, Wang group develops a new method to prepare a composite photocatalyst based on TiO_2 and HKUST-1 [198]. They creatively employ a fast and scalable aerosol route to prepare HKUST-1 and HKUST-1/TiO_2 composites. The effects of synthetic temperature and substrate ratio on fundamental natures of the materials are studied in detail. Solvent evaporation causes the huge change of substrate ratio, and promotes the rapid formation of nucleation and crystal growth of HKUST-1. Theoretical calculations also demonstrate solvent evaporation and high heat transfer efficiency drive the process of reactions. The as-synthesized samples (HKUST-1 and HKUST-1/TiO_2) possess high crystallinity, large surface area and excellent photostability. HKUST-1/TiO_2 can maintain a large surface area after trapping TiO_2, leading to its enhanced photocatalytic efficiency. In situ DRIFTS analysis reveals that the stable and high reactant uptake of HKUST-1 plays a key role in the enhancement of photocatalytic performance. Another similar work has been covered recently. UiO-66 has been selected and explored for enriching CO_2 in order to obtain an effective CO_2 adsorption in TiO_2/UiO-66. TiO_2/UiO-

66 exhibits a hierarchical porous structure with a high CO_2 uptake of 78.9 cm^3 g^{-1}. TiO_2/UiO-66 owns similar photocatalytic efficiency under both pure CO_2 atmosphere and diluted CO_2 condition (≤2%). This interesting experimental result may result from CO_2 enrichment and abundant photocatalytic sites in TiO_2/UiO-66 [199].

In 2018, a polyoxometalate-based MOF NENU-10 is employed to integrate with Au nanoparticles [202], generating a hybrid photocatalyst Au@NENU-10. In Au@NENU-10, various components plays different roles role in photocatalysis, in which PTiW ($[PTi_2W_{10}O_{40}]^{7-}$) stores electrons and protons and serves as a reactive active center for CO_2 reduction; HKUST-1 enriches CO_2 molecules, and Au nanoparticles adsorb visible light. The combination of Au nanoparticles and PTiW promotes the fast separation of electrons-hole pairs, and the strong protonation effect of PTiW extends the lifetime of electron-coupled protons. Moreover, it should be mentioned that PTiW possesses strong protonation effect resulting from Ti = O and Ti-O-W, and causes the exposure of {1 0 0} plane of NENU-10 as well as uniform distribution of Au nanoparticles. To sum up, the above factors make Au@NENU-10 exhibit great CO_2 photoreduction activity and selectivity of products under visible light irradiation (λ > 420 nm).

Due to its highest CO_2 uptake among MOFs, CPO-27-Mg is selected to integrate with TiO_2 to obtain CPO-27-Mg/TiO_2 nanocomposite via in situ hydrothermal growth method [203]. In CPO-27-Mg/TiO_2 nanocomposite, TiO_2 nanospheres are doped both inside and outside CPO-27-Mg microcrystals. The CPO-27-Mg/TiO_2 nanocomposites exhibit increased activity, and can reduce CO_2 to CO and CH_4, because of its high uptake toward CO_2 and exposed alkaline metal sites. This work presents an effective approach for preparing a MOF/semiconductor composite photocatalyst.

The precise control synthesis of TiO_2, such as phase, shape, morphology etc. is still a huge challenge. MOFs containing Ti, for example, MIL-125, may be a good choice for acting as a sacrifice template in order to prepare TiO_2 with different phase, morphologies, size and so on. In this work, MIL-125 is selected to act as a host matrix to encapsulate pre-synthesized gold nanoparticles (GNPs) firstly, yielding GNP/NH_2-MIL-125 [204], and then is pyrolyzed to obtain gold/titania nanocomposites, defined as GNP/TiO_2, which can retain its original size and morphology of nanocrystals. The doping of GNPs on MOF derived TiO_2 exhibits significantly enhanced photocatalytic activity toward CO_2, which can convert CO_2 into CH_4. The catalytic activities of GNP/TiO_2 are better than those of TiO_2, P25 and Aurolite, due to the vital role of GNPs in the material.

Three years later, another composite photocatalyst based on TiO_2 has been reported using MIL-125 as a sacrifice template. Feng et al. use MIL-125 as the sacrifice template to prepare porous TiO_2 with mixed anatase–rutile phases [205]. Through atomic layer deposition (ALD) method, ultrathin MgO layers with different thicknesses are coated on porous TiO_2. Among these samples, TiO_2 coated with 5 layers of MgO exhibits the best performance. After the deposition of MgO, the number of Ti^{3+} species on TiO_2 surface increases and hydroxyl groups bonded with Mg appear, both of which are useful for CO_2 adsorption and photoreduction. The MgO layer deactivates the TiO_2 surface states and separates surface electron-hole pairs. A control experiment has been carried out. Another similar photocatalyst is synthesized via a conventional wet-impregnation (WI) method. The performance of the WI synthesized MgO/TiO_2 samples is lower than ALD synthesized MgO/TiO_2, because uniformly distributed MgO coating produced by ALD method can generate more surface Ti^{3+} sites than WI synthesized samples. The finding indicates that ALD coating may be a better way for improving the performance.

Photocatalysts with hierarchical, hollow structure usually exhibit a good photocatalytic performance owing to the hollow structure that can endow these materials with large surface area, high light-utilization efficiency and CO_2 adsorption ability. Therefore, this kind of photocatalyst have drawn significant attentions. Recently, Zhang group carbonizes the Ni-Zn bimetallic MOFs to generate ZnO/NiO porous hollow spheres [206]. The heterogeneous n-type ZnO and p-type NiO resulting from the decomposition of Zn-Ni MOFs are homogeneously mixed, leading to the generation of many p-n heterojunctions. The analyses of XPS spectra suggest that the photo-excited electrons produced by ZnO can transfer to NiO and internal electric field exists between the interface of ZnO and NiO. Moreover, porous hollow structure with improved CO_2 adsorption and light harvesting indeed enhances the CO_2 photoreduction activity. Therefore, the photocatalyst possesses great photoreduction CO_2 performance, and can convert CO_2 into methanol (1.57 μmol g^{-1} h^{-1}). This work sheds light on preparing new composite photocatalysts with hollow structure by means of multi-metallic organic frameworks as templates.

3.7. Non-Metal-Based photocatalysts

The discovery of polymeric carbon nitride photocatalyst has attracted researcher's interests toward metal-free photocatalysts. Now, many kinds of metal-free photocatalysts have emerged as photocatalysts for CO_2 conversion. For example, carbon fibers (CFs) have been used as photocatalysts using Ag nanoparticles as the sensitizer, and can produce CH_3OH [207]. Similarly, β-SiC with hollow spherical 3D structure is employed to reduce CO_2 with pure water, and the doped Pt acts as the co-photocatalyst [208]. The optimal sample (2.0 wt% Pt) possesses a stable CH_4 formation rate of 16.8 μmol g^{-1} h^{-1}.

Semiconductors containing Boron have served as promising metal-free photocatalysts in CO_2 photoreduction. Boron carbide (B_4C) is one kind of typical boron based photocatalyst [209]. Five different photocatalysts catalyzed by five transition metals (Fe, Co, Ni, Cu, and Zn) are synthesized. Among them, the as-synthesized photocatalyst in the presence of Ni possesses a surface area of 130.55 m^2 g^{-1} and exhibits the best performance. The performances of Ni catalyzed B_4C at different calcination temperatures are investigated in detail. They find that the crystallinity and surface area can influence the photo-generated holes and electrons, respectively. The Ni catalyzed B_4C carbonized at 950 °C exhibits the best activity. This finding reveals the crystallinity of B_4C photocatalysts may play an important role in the generation of holes and the surface area influences the production of electrons.

Covalent organic frameworks (COFs), with unique advantages have been employed for photoreduction of CO_2 [210–212]. Zhou group introduces the bromine functional group to a porphyrin-based COF (TAPBB-COF), which improves its catalytic performance obviously. The yield of TAPBB-COF is 295.2 μmol g^{-1} for 12 h, and the good recycle stability as well as selectivity is found [210]. Recently, Lan group puts forward a novel strategy to prepare hybrid photocatalysts [211]. This group creatively combines semiconductors with COFs via covalent bonds for the first time, and synthesizes a stable hybrid Z-scheme heterojunction: COF-318/316-semiconductors. A family of Z-scheme photocatalysts based on semiconductors (TiO_2, Bi_2WO_6, and α-Fe_2O_3) and COF-316/318 have been prepared (Fig. 33), and can convert CO_2 into CO. The CO formation rate can reach up to 69.67 μmol g^{-1} h^{-1}. The evidences resulting from experiments and theoretical calculations demonstrate that electrons transfer from semiconductor to COF by covalent coupling. Enriched electrons in the cyano/pyridine groups of the COF are used to reduce CO_2 and holes remaining in the semiconductor can oxidize H_2O, completing the process of photosynthesis.

4. Summary of photocatalysts

Great advances in photocatalysis have driven researchers to employ sunlight to reduce CO_2. Various photocatalysts have been designed and synthesized up to now. Summarily, photocatalysts for photoreduction CO_2 with water in solid–gas mode contain TiO_2 based photocatalysts, metal oxide based photocatalysts, metal chalcogenides/nitrides/based photocatalysts, bismuth based photocatalysts, g-C_3N_4 based photocatalysts and MOFs based photocatalysts, etc. It's a fact that all the photocatalysts described here are not suitable for the practical applications in natural sunlight, and performances of some photocatalysts are unable to be satisfied even under UV irradiation. Furthermore, most of final products focus on gaseous substances irradiated by UV or visible light, and the major products are CH_4 and CO. Other products including CH_3OH, C_2H_6, CH_3CHO, C_2H_5OH as well as HCOOH, are rarely reported, depending on the used photocatalyst. Here we will present the commonalities of each photocatalyst toward photoreduction products.

TiO_2 based materials have been applied as the photocatalysts for decades. Individual TiO_2 usually generates CH_4 and/or CO under simulated sunlight irradiation in the solid–gas mode. While metal-doping as well as hybridization with other materials might induce the generation of new products such as CH_3CHO, CH_3OH, C_2H_6 and C_2H_5OH, etc. Among them, noble metal doping or the combination with graphene materials usually achieve an efficiency enhancement in the generation of products.

Metal oxides/hydroxides based photocatalysts have been intensely investigated in photocatalysis. Various strategies like surface modification, morphology control, metal decoration, and the hybrid heterojunctions have been demonstrated to possess significant effects on the formation rates and selectivity of metal oxides/hydroxides based photocatalysts. For most of them, the C_1 compounds (e.g., CO and CH_4, etc.) are the main reduction products.

Metal chalcogenides and nitrides have been widely explored in photocatalytic hydrogen production, and are still in its infancy in the photoreduction of CO_2. Most of the modification strategies are similar as those of metal oxides. They can successfully convert CO_2 into C_1 products such as CO, CH_4 and CH_3OH.

As a kind of metal-free catalysts, C_3N_4 based photocatalysts have been extensively utilized in a variety of applications during the past decades. Various approaches have been employed to modify C_3N_4 based photocatalysts, where ternary g-C_3N_4 based photocatalysts modified by metal or metal oxides as well as hybridization with carbon materials can enhance the photocatalytic activity of g-C_3N_4 significantly. In these photocatalytic systems, the final products mostly focus on CH_4, CO or the mixture of them, while doping of metal sulfide make g-C_3N_4 produce CH_3OH.

As a family of excellent photocatalysts, bismuth based photocatalysts will naturally be applied in CO_2 photoreduction. However, they usually exhibit low performance owing to the limited CB. Therefore, surface modification and heterojunctions have been applied to improve their CO_2 photoreduction activity. The products of CO_2 photocatalysis in the solid–gas mode by bismuth based photocatalysts are generally CH_4, CO or their mixture, and the yields are usually poor. New strategies that can conquer the inert bottlenecks would be still needed to achieve high activity for bismuth based photocatalysts to produce higher-value products.

MOFs with the advantages of well-defined structures, high porosity, tunable structure and functionality have become emerging platforms to adsorb light and provide photocatalytic centers for CO_2 photocatalysis in solid–gas mode. The commonly utilized strategy is the integration of MOFs with other functional materials, which gives birth to many hybrid photocatalysts with high performance. The products are mainly focused on the C_1 compounds (e.g., CO and CH_4) and hydrocarbon products such as CH_3OH appears in a few examples. MOF-based photocatalysts are very promising for completing the key mission of the artificial photosynthesis yet are still in early stage.

Above all, the types of products resulted from the photoreduction CO_2 are closely related with the band gap and surface topography of the photocatalysts. Accurate understanding of reaction pathway for CO_2 reduction is very important in designing and synthesizing target photocatalysts to obtain desired products. For example, the tuning of CB and VB energy for TiO_2 can convert CO_2 into formic acid, methanol and methane. However, the truth of the matter is that TiO_2 possesses poor selectivity towards the product, which depends on the electrons obtained for each reaction. Although the reduction potential of producing CH_4 is more positive compared with other reactions, this conversion needs more electrons to proceed. Therefore, enough electron-hole pairs and efficient charge separations are decisive factors for photoreduction CO_2 into various products selectively.

5. Conclusions and perspectives

Although the photoreduction CO_2 into useful chemicals sheds light on the mitigating of environmental problem caused by CO_2 emissions, there is still a long way to achieve the real application of this conversion. Indeed, the photoreduction conversion of water (serving as reducing agent) and CO_2 into valuable chemical fuels is an alternative choice to address the CO_2 problem. However, the extremely slow oxidation of water limits the CO_2 reduction efficiency with H_2O, making the reduction efficiency difficult to reach the applicable target.

Up to now, there exist several common bottlenecks in this photoreduction process, and contain the following issues. i) These processes generally face low light harvesting and energy conversion efficiency, which is vital in converting photon energy into chemical energy. ii) The coupling harmful oxidation process will lead to low conversion selectivity and efficiency of CO_2 photoreduction. The spontaneous oxidation of generated products also occurs on the surface of photocatalysts in the reaction process, which needs to be avoided as much as possible. Therefore, it is necessary for photocatalysts to release the formed products quickly to minimize this harmful transformation process. iii) The low selectivity of desired products. Because the photoreduction of CO_2 is an extremely complex, multi-path and multi-product process by means of multi-electron migration, and several kinds of products may be simultaneously generated, which has a great influence on the selectivity and formation rate of product. Besides, the hydrogen evolution reaction (HER) reaction competes with the CO_2 conversion reaction. The selectivity of the desired product is closely related to the morphology of photocatalyst, especially their ability in adsorbing and activating CO_2. iv) The products are mostly focused on C_1 compounds (e.g., CO, HCOOH, CH_4, and so on), and only a few cases cover C_2 compounds (e.g., C_2H_4 and EtOH, etc.), where C_{2+} hydrocarbons would be more desirable in market value. v) The structure–property relationship and reaction mechanism in the photocatalytic process are still confused, in which the structures of some reported photocatalysts are not clear enough to evaluate the structure–activity relationship and reaction mechanism. Besides, the reaction mechanism especially the deactivation mechanism needs to be investigated very carefully to provide new guidance in designing powerful photocatalysts. Fortunately, computational calculations about the reactive pathways and the factors influencing the generation of the desired products can provide a clear planning blueprint. Eventually, experimental evidences

as well as theoretical simulations might be combined to give a complete and clear reaction mechanism for CO_2 photoreduction.

A critical issue should be addressed, and it is urgent to demonstrate whether the final product only comes from CO_2. Most of reported works have not proved that final products result from CO_2 through $^{13}CO_2$ labeling or other methods. Some investigations reveal that the introduced carbon residues indeed take part in the reduction processes and contribute to the final product yield [215]. Isotopic $^{13}CO_2$ labeling is an efficient approach to confirm the source of final products. Moreover, a control experiment in the presence of inert gas (e.g., Ar and N_2, etc.) can also verify whether the carbon residues participate in the CO_2 photoreduction.

Moreover, it is critical to design and synthesize highly efficient and selective photocatalysts that can adsorb the solar spectrum and separate charge efficiently. Band gap usually represents the adsorbing light ability of a photocatalyst. A variety of strategies have been proposed to prepare the desired photocatalysts [17,29]. The common strategies including the integration of sensitizers, non-metals or narrow band-gap semiconductors and doping metals have been applied to prepare composite photocatalysts, which might utilize both UV and visible light simultaneously [18–20,26–28]. Additionally, the syntheses of heterostructures can promote electron-hole separation, and the introduction of co-photocatalysts and/or functional groups might further enhance the photocatalytic activity and selectivity. In composite photocatalyst, it might simultaneously achieve the photo-generated electrons transferring to one component fast and photo-generated holes transporting to the other one, obtaining efficient charge separation efficiency. Furthermore, exposing desired crystal facet, introduction of surface defects, and construction of hierarchical micro/nano-structures would also be effective approaches to provide active sites for the adsorption and activation of CO_2 and enhance the light utilization and charge transfer. Various synthetic methods have been developed to precisely control the structures of photocatalysts, such as surface morphologies, hierarchical pore networks, and so on [29,31]. Additionally, the stability is also an important factor for its reusability and recoverability. The design of highly stable photocatalysts that can remain original phase, morphology and activity is essential and vital in the practical applications. The most important, the structure–property relationships between photocatalysts and products should be in-depth investigated. Theoretical calculations should combine with extensive experimental evidences to elucidate the structure–property relationship.

In summary, this review summarizes the recent developments of representative photocatalysts in photoreduction of CO_2 and conclude the major advantages and problems for them. The details of them are briefly summarized as below. For TiO_2, as a kind of typical photocatalyst, the enhancement of their performances might lie in the precise control toward the surface morphology with different exposed facets, achieving higher specific surface area, metal/non-metal doping, more exposed active sites, which might be realized through various methods like hydrothermal/solvothermal, sol–gel, template-assisted and chemical vapor deposition approaches, etc.. Other novel materials like metal oxide based photocatalysts possessing high stability, have been intensively investigated yet are still restricted by the poor efficiency of the photocatalytic reaction. Modification strategies that can control properties like the particle size, surface morphology or band structure through carefully designing the synthesis process, have been proposed. However, there are still several issues need to be paid much attention on: i) economic and simple synthetic method is most important for the preparation of photocatalysts with high performance; ii) the integration of new plasmonic materials and semiconductors give birth to heterojunctions in order to optimize the charge transfer; iii) theoretical calculation would offer a better understanding of the charge and energy transfer kinetics, thereby guiding the design of high-quality photocatalysts.

Bi-based nanomaterials generally tend to form 2D layered structures, which is favorable for photocatalytic reaction. Of course, Bi-based photocatalysts have been explored to reduce CO_2 in recent years. Most widely studied Bi-based photocatalysts for photoreduction CO_2 focus on BiOX (X = Cl, Br, I), $BiVO_4$, and Bi_2MO_6 (M = Mo, W). Other Bi-based photocatalysts, for example, $BiPO_4$, are not explored for the reduction of CO_2. The next step is to study the CO_2 photoreduction ability of other unexplored materials in the photocatalytic process. Besides, the stability should be taken into account in the development of Bi-based photocatalysts. Surface defects indeed can enhance the adsorption and activation of CO_2, however, excess surface defects will also limit the separation of charge carriers. Therefore, under long-term light irradiation, the emergence of abundant defects and the deposition of elemental Bi will actually affect the performance of Bi-based photocatalysts. The exploration of Bi-based photocatalysts has been continuously investigated, and several approaches like creating defects, Bi-rich strategy, exposing desired facets, and Z-scheme heterojunction have been applied to further develop the advantages of Bi-based photocatalysts.

g-C_3N_4, as a polymer semiconductor without metals possessing abundance, excellent chemical stability, attractive electronic structure and high redox potential, have been intensively studied as photocatalysts. However, g-C_3N_4 exhibits several intrinsic disadvantages, and various modifications towards g-C_3N_4 have been carried out in order to achieve efficient composite photocatalysts with high surface area, extended visible-light absorption, low band gap energy and efficient separation of charge carriers. Several strategies are listed below: i) tuning the surface groups of g-C_3N_4 through introducing monomers or heteroatoms or controlling the synthesis process to promote the adsorption and activation of CO_2 and ii) integration of other materials, such metal ions, metal oxides, so as to change the band structure as well as its electron distribution and its surface properties. Despite the interesting performance presented for g-C_3N_4, the investigations are still at its early stage and there are long way to go.

Compared with the above-mentioned photocatalysts, porous coordination polymers (e.g., MOFs or COFs) based photocatalysts have their intrinsic unique advantages in CO_2 photoreduction. Firstly, their porous structures enable these photocatalysts to possess high CO_2 adsorption capacity. Secondly, a variety of metal clusters and organic ligands can be applied to tune the light adsorbing ability, the number or type of photocatalytic active sites, in which the functions of porous coordination polymers can be expanded by means of post modification of inorganic metal clusters or organic linkers. Thirdly, available channels allow reactants and sacrificial agents to transfer freely to active sites to ensure timely utilization of photo-generated charges. Fourthly, various porous coordination polymers based photocatalysts are easy to be synthesized owing to their mild and simple synthetic conditions. However, porous coordination polymers based photocatalysts still face the stability challenge in long-term utilization owing to the structural collapse, which will cause irreversible decay of photocatalytic activity. Besides, powerful devices (e.g., membranes, films, foams or fibers, etc.), fabricated from the shaping of porous coordination polymers, would be more desired forms in CO_2 photoreduction, which can conquer the inert crystalline nature and enable convenient storage or transportation. Therefore, the development of highly stable and active porous coordination polymers based photocatalysts with novel processing forms is long-sought-after.

In conclusion, this review has summarized the reported literatures about CO_2 photoreduction via the solid–gas mode including the summary of their performances, reaction conditions and mech-

anistic pathway, etc.. During the past decades, various kinds of photocatalysts have been designed and explored, and more and more endeavours about CO_2 photoreduction have been made. However, the exploration of CO_2 photoreduction in the solid–gas mode is still in its infancy and the performance of reported photocatalysts are far from meeting the demand of practical applications. There are some inevitable problems such as the dispersion of photocatalyst ground powder, stability, the limited solubility or adsorption ability of CO_2 and it is hard to separate very few products from the mixed system, especially for liquid products. The development of novel solid–gas catalysis systems that can conquer these problems still need a long way to go. Besides, the CO_2 reduction rate is still too low. The catalyst activity should be improved from the current $\mu mol\ g^{-1}\ h^{-1}$ scale to $mmol\ g^{-1}\ h^{-1}$ and even $mol\ g^{-1}\ h^{-1}$, which is closely related to the the design and synthesis of efficient, sustainable and low-cost photocatalysts. To this end, the wider exploration of in-situ characterization technologies (e.g., FT-IR, XPS, EPR or TEM, etc.) is more necessary for providing precise experimental evidences of CO_2 photoreduction, such as recognition of reactive sites, capture of intermediates, inference of reaction pathway, and so on. Furthermore, detailed theoretical calculations would make the process of CO_2 photoreduction clearer and can provide more guidance for designing new and highly efficient photocatalysts. The combination of them will help in the development of more precise theoretical models and deepen our understanding of catalytic structure–property relationships specific to the designed photocatalysts. Moreover, new approaches such as chemical analysis and parallel chemical screening that can integrate the advance of computer technology would be more designed for both sample-synthesis and product analysis. In summary, the photoreduction conversion of CO_2 into valuable chemical materials through such a solid–gas mode has a profound impact on the future environment and energy, which would play a role of "killing two birds with one stone" in closing the carbon cycle and solving the environmental problems. Although CO_2 photoreduction has attracted sustained attentions and various photocatalysts have been continuously employed for CO_2 conversion, there is still a huge gap between photocatalytic performance and practical applications at current states. The past decades have achieved prosperous development all around the world in this filed, and, as we envisioned, tremendous efforts are still needed in the next decade to achieve "lab to industry" technology advance in many ways. We hope this review will provide new insights or guidance for readers to have a deep understanding of this field and promote the development of novel catalysis systems to expand the limitation of current technology.

Declaration of Competing Interest

The authors declare that they have no known competing financial interests or personal relationships that could have appeared to influence the work reported in this paper.

Acknowledgement

This work was financially supported by NSFC (No. 21871141, 21871142, 21901122, 22071109and 92061101); the Natural Science Research of Jiangsu Higher Education Institutions of China (19KJB150011) and Project funded by China Postdoctoral Science Foundation (No. 2018M632328, 2018M630572 and 2019M651873); Priority Academic Program Development of Jiangsu Higher Education Institutions and the Foundation of Jiangsu Collaborative Innovation Center of Biomedical Functional Materials.

References

[1] G.A. Ozin, Throwing New Light On The Reduction of CO_2, Adv. Mater. 27 (2015) 1957–1963.
[2] M. Pera-Titus, Porous inorganic membranes for CO_2 capture: present and prospects, Chem. Rev. 114 (2014) 1413–1492.
[3] Z. Sun, N. Talreja, H. Tao, J. Texter, M. Muhler, J. Strunk, J. Chen, Catalysis of carbon dioxide photoreduction on nanosheets: fundamentals and challenges, Angew. Chem. Int. Ed. 57 (2018) 760–762.
[4] A.D. Handoko, K.F. Li, J.W. Tang, C. Opin, Recent progress in artificial photosynthesis: CO_2 photoreduction to valuable chemicals in a heterogeneous system, Chem. Eng. J. 2 (2013) 200–206.
[5] J.D. Xiao, H.L. Jiang, Metal-organic frameworks for photocatalysis and photothermal catalysis, Acc. Chem. Res. 52 (2019) 356–366.
[6] N. Li, J. Liu, B.X. Dong, Y.Q. Lan, Polyoxometalate-based compounds for photo/electrocatalytic applications, Angew. Chem. Int. Ed. 59 (2020) 20779–20793.
[7] D.D. Li, M. Kassymova, X.C. Cai, S.Q. Zang, H.L. Jiang, Photocatalytic CO_2 reduction over metal-organic framework-based Materials, Coord. Chem. Rev. 412 (2020) 213262.
[8] L.G. Li, Y. Huang, Y.G. Li, Carbonaceous materials for electrochemical CO_2 reduction, EnergyChem 2 (2020) 100024.
[9] X.F. Li, Q.L. Zhu, MOF-based materials for photo- and electrocatalytic CO_2 reduction, EnergyChem 2 (2020) 100033.
[10] D.C. Liu, D.C. Zhong, T.B. Lua, Non-noble metal-based molecular complexes for CO_2 reduction: from the ligand design perspective, EnergyChem 2 (2020) 100034.
[11] X.R. Li, X.C. Yang, H.G. Xue, H. Pang, Q. Xu, Metal-organic frameworks as a platform for clean energy applications, EnergyChem 2 (2020) 100027.
[12] S. Wang, C. Xi, Recent advances in nucleophile-triggered CO_2-incorporated cyclization leading to heterocycles, Chem. Soc. Rev. 48 (2019) 382–404.
[13] J.F. Xie, Y.B. Wang, Recent development of CO_2 electrochemistry from Li-CO_2 batteries to Zn-CO_2 batteries, Acc. Chem. Res. 52 (2019) 1721–1729.
[14] J.L. White, M.F. Baruch, J.E. Pander, Y. Hu, I.C. Fortmeyer, J.E. Park, T. Zhang, K. Liao, J. Gu, Y. Yan, T.W. Shaw, E. Abelev, A.B. Bocarsly, Light-driven heterogeneous reduction of carbon dioxide: photocatalysts and photoelectrodes, Chem. Rev. 115 (2015) 12888–12935.
[15] W. Kim, E. Edri, H. Frei, Hierarchical inorganic assemblies for artificial photosynthesis, Acc. Chem. Res. 49 (2016) 1634–1645.
[16] T. Inoue, A. Fujishima, S. Konishi, K. Honda, Photoelectrocatalytic reduction of carbon dioxide in aqueous suspensions of semiconductor powders, Nature 277 (1979) 637–638.
[17] Y.H. Luo, L.Z. Dong, J. Liu, S.L. Li, Y.Q. Lan, W.G. Tu, Y. Zhou, Z.G. Zou, From molecular metal complex to metal-organic framework: the CO_2 reduction photocatalysts with clear and tunable structure, Coord. Chem. Rev. 390 (2019) 86–126.
[18] K. Li, B. Peng, T. Peng, Recent advances in heterogeneous photocatalytic CO_2 conversion to solar fuels, ACS Catal. 6 (2016) 7485–7527.
[19] C.L. Wang, Z.X. Sun, Y. Zheng, Y.H. Hu, Recent progress in visible light photocatalytic conversion of carbon dioxide, J. Mater. Chem. A 7 (2019) 865–887.
[20] L.F. Wei, C.L. Yu, Q.H. Zhang, H. Liu, Y. Wang, TiO_2-based heterojunction photocatalysts for photocatalytic reduction of CO_2 into solar fuels, J. Mater. Chem. A 6 (2018) 22411–22436.
[21] A. Corma, H.J. Garcia, Photocatalytic reduction of CO_2 for fuel production: possibilities and challenges, Catal. 308 (2013) 168–175.
[22] Y.C. Izumi, Recent advances in the photocatalytic conversion of carbon dioxide to fuels with water and/or hydrogen using solar energy and beyond, Chem. Rev. 257 (2013) 171–186.
[23] J. Mao, K. Li, T.Y. Peng, Recent advances in the photocatalytic CO_2 reduction over semiconductors, Catal. Sci. Technol. 3 (2013) 2481–2498.
[24] K.F. Li, X.Q. An, K.H. Park, M. Khraisheh, J.W. Tang, A critical review of CO_2 photoconversion: catalysts and reactors, Catal. Today 224 (2014) 3–12.
[25] M. Marszewski, S.W. Cao, J.G. Yu, M. Jaroniec, Semiconductor-based photocatalytic CO_2 conversion, Mater. Horiz. 2 (2015) 261–278.
[26] G. Sneddon, A. Greenaway, H.H.P. Yiu, The Potential applications of nanoporous materials for the adsorption, separation, and catalytic conversion of carbon dioxide, Adv. Energy Mater. 4 (2014) 1301873.
[27] E.V. Kondratenko, G. Mul, J. Baltrusaitis, G.O. Larrazábal, J. Pérez-Ramírez, Status and perspectives of CO_2 conversion into fuels and chemicals by catalytic, photocatalytic and electrocatalytic processes, Energy Environ. Sci. 6 (2013) 3112–3135.
[28] Y. Ma, X. Wang, Y. Jia, X. Chen, H.L. Han, Titanium dioxide-based nanomaterials for photocatalytic fuel generations, Chem. Rev. 114 (2014) 9987–10043.
[29] D. Chen, X.G. Zhang, A.F.J. Lee, Synthetic strategies to nanostructured photocatalysts for CO_2 reduction to solar fuels and chemicals, J. Mater. Chem. A 3 (2015) 14487–14516.
[30] S.W. Cao, J.X. Low, J.G. Yu, M. Jaroniec, Polymeric photocatalysts based on graphitic carbon nitride, Adv. Mater. 27 (2015) 2150–2176.
[31] S.N. Habisreutinger, L. Schmidt-Mende, J.K. Stolarczyk, Photocatalytic reduction of CO_2 on TiO_2 and other semiconductors, Angew. Chem. Int. Ed. 52 (2013) 7372–7408.
[32] G. Sahara, O. Ishitani, Efficient photocatalysts for CO_2 reduction, Inorg. Chem. 54 (2015) 5096–5104.

[33] A.D. Handoko, K.F. Li, J.W. Tang, Recent progress in artificial photosynthesis: CO_2 photoreduction to valuable chemicals in a heterogeneous system, Curr. Opin. Chem. Eng. 2 (2013) 200–206.
[34] Y.P. Yuan, L.W. Ruan, J. Barber, S.C.J. Loo, C. Xue, Hetero-nanostructured suspended photocatalysts for solar-to-fuel conversion, Energy Environ. Sci. 7 (2014) 3934–3951.
[35] N. Linares, A.M. Silvestre-Albero, E. Serrano, J. Silvestre-Albero, Garcia-Martinez, Mesoporous materials for clean energy technologies, Chem. Soc. Rev. 43 (2014) 7681–7717.
[36] H.Q. Sun, S.B. Wang, Research advances in the synthesis of nanocarbon-based photocatalysts and their applications for photocatalytic conversion of carbon dioxide to hydrocarbon fuels, Energy Fuels 28 (2014) 22–36.
[37] Q.J. Xiang, B. Cheng, J.G. Yu, Graphene-based photocatalysts for solar-fuel generation, Angew. Chem. Int. Ed. 54 (2015) 11350–11366.
[38] A.T. Najafabadi, Emerging applications of graphene and its derivatives in carbon capture and conversion: current status and future prospects, Renewable Sustainable Energy Rev. 41 (2015) 1515–1545.
[39] S. Das, W. Daud, A review on advances in photocatalysts towards CO_2 conversion, RSC Adv. 4 (2014) 20856–20893.
[40] T. Zhang, W.B. Lin, Metal-organic frameworks for artificial photosynthesis and photocatalysis, Chem. Soc. Rev. 43 (2014) 5982–5993.
[41] S. Kumar, M.Y. Wani, C.T. Arranja, J.A. Silva, B. Avula, A.J. Sobral, Porphyrins as nanoreactors in the carbon dioxide capture and conversion: a review, J. Mater. Chem. A 3 (2015) 19615–19637.
[42] P. Zhou, J.G. Yu, M. Jaroniec, All-solid-state Z-scheme photocatalytic systems, Adv. Mater. 26 (2014) 4920–4935.
[43] S. Ye, R. Wang, M.Z. Wu, Y.P. Yuan, A review on g-C_3N_4 for photocatalytic water splitting and CO_2 reduction, Appl. Surf. Sci. 358 (2015) 15–27.
[44] Y.N. Gong, W.H. Zhong, Y. Li, Y.Z. Qiu, L.R. Zheng, J. Jiang, H.L. Jiang, Regulating photocatalysis by spin-state manipulation of cobalt in covalent organic frameworks, J. Am. Chem. Soc. 142 (2020) 16723–16731.
[45] H.Q. Xu, J.H. Hu, D.K. Wang, Z.H. Li, Q. Zhang, Y. Luo, S.H. Yu, H.L. Jiang, Visible-light photoreduction of CO_2 in a metal-organic framework: boosting electron-hole separation via electron trap states, J. Am. Chem. Soc. 137 (2015) 13440–13443.
[46] H. Abdullah, M.M.R. Khan, H.R. Ong, Z. Yaako, Modified TiO_2 photocatalyst for CO_2 photocatalytic reduction: an overview, J. CO_2 Util. 22 (2017) 15–32.
[47] X.Y. He, C.L. Zhang, Recent advances in structure design for enhancing Photocatalysis, J. Mater. Sci. 54 (2019) 8831–8851.
[48] M. Cokoja, C. Bruckmeier, B. Rieger, W.A. Herrmann, F.E. Kühn, Transformation of carbon dioxide with homogeneous transition-metal catalysts: a molecular solution to a global challenge?, Angew Chem. Int. Ed. 50 (2011) 8510–8537.
[49] N. Li, J. Liu, J.J. Liu, L.Z. Dong, S.L. Li, B.X. Dong, Y.H. Kan, Y.Q. Lan, Self-assembly of phosphate-centered polyoxo-titanium cluster: discovery of new "Heteroatom Keggin Family", Angew. Chem. Int. Ed. 58 (2019) 17260–17264.
[50] M. Lu, J. Liu, Q. Li, M. Zhang, M. Liu, J.L. Wang, D.Q. Yuan, Y.Q. Lan, Rational crystalline covalent organic frameworks design for efficient CO_2 photoreduction with H_2O, Angew. Chem. Int. Ed. 58 (2019) 12392–12397.
[51] N. Li, J. Liu, J.J. Liu, L.Z. Dong, Z.F. Xin, Y.L. Teng, Y.Q. Lan, Adenine components in biomimetic metal-organic frameworks for efficient CO_2 photoconversion, Angew. Chem. Int. Ed. 58 (2019) 5226–5231.
[52] S.L. Xie, J. Liu, L.Z. Dong, S.L. Li, Y.Q. Lan, Z.M. Su, Hetero-metallic active sites coupled with strong reductive polyoxometalate for selectively photocatalytic CO_2-to-CH_4 conversion in water, Chem. Sci. 10 (2019) 185–190.
[53] M. Lu, Q. Li, J. Liu, F.M. Zhang, L. Zhang, J.L. Wang, Z.H. Kang, Y.Q. Lan, Installing earth-abundant metal active centers to covalent organic frameworks for efficient heterogeneous photocatalytic CO_2 reduction, Appl Catal B-Environ. 5 (2019) 624–633.
[54] X.X. Li, J. Liu, L. Zhang, L.Z. Dong, Z.F. Xin, S.L. Li, X.Q. Huang-Fu, K. Huang, Y.Q. Lan, Hydrophobic polyoxometalate-based metal-organic framework for efficient CO_2 photoconversion, ACS Appl. Mater. Interfaces 11 (2019) 25790–25795.
[55] Q. Huang, J. Liu, L. Feng, Q. Wang, W. Guan, L.Z. Dong, L. Zhang, L.K. Yan, Y.Q. Lan, H.C. Zhou, Multielectron transportation of polyoxometalate-grafted metalloporphyrin coordination frameworks for selective CO_2-to-CH_4 photoconversion, Natl. Sci. Rev. 7 (2019) 53–63.
[56] L.Z. Dong, L. Zhang, J. Liu, Q. Huang, M. Lu, W.X. Ji, Y.Q. Lan, Stable heterometallic cluster-based organic frameworks catalysts for artificial photosynthesis, Angew. Chem. Int. Ed. 59 (2019) 2659–2663.
[57] Z. Zhu, W.R. Huang, C. Chen, R. Wu, Preparation of Pd-Au/TiO_2-WO_3 to enhance photoreduction of CO_2 to CH_4 and CO, J. CO_2 Util. 28 (2018) 247–254.
[58] J. Jiao, Y. Wei, K. Chi, Z. Zhao, A. Duan, J. Liu, G. Jiang, Y. Wang, X. Wang, C. Han, P. Zheng, Platinum nanoparticles supported on TiO_2 photonic crystals as highly active photocatalyst for the reduction of CO_2 in the presence of water, Energy. Technol-Ger. 5 (2017) 877–883.
[59] W. Wang, D. Xu, J. Cheng, C.J. Yu, Hybrid carbon@TiO_2 hollow spheres with enhanced photocatalytic CO_2 reduction activity, J. Mater. Chem. A 5 (2017) 5020–5029.
[60] L.L. Tan, W. Ong, S.P. Chai, A.R. Mohame, Photocatalytic reduction of CO_2 with H_2O Over graphene oxide-supported oxygen-rich TiO_2 Hybrid photocatalyst under visible light irradiation: process and kinetic studies, Chem. Eng. J. 308 (2017) 248–255.
[61] T.D. Pham, B.K. Lee, Novel capture and photocatalytic conversion of CO_2 into solar fuels by metals co-doped TiO_2 deposited on PU under visible light, Appl. Catal. A-Gen. 529 (2017) 40–48.
[62] M. Tahir, B. Tahir, A.S. Amin, H. Alias, Selective photocatalytic reduction of CO_2 by H_2O/H_2 to CH_4 and CH_3OH over Cu-promoted In_2O_3/TiO_2 nanocatalyst, Appl. Surf. Sci. 389 (2016) 46–55.
[63] M.A.M. Júnior, A. Morais, A.F. Nogueira, Boosting the solar-light-driven methanol production through CO_2 photoreduction by loading Cu_2O on TiO_2-pillared $K_2Ti_4O_9$, Micropor. Mesopor. Mater. 234 (2016) 1–11.
[64] S.M. Park, A. Razzaq, Y.H. Park, S. Sorcar, Y. Park, C.A. Grimes, Hybrid Cu_xO-TiO_2 heterostructured composites for photocatalytic CO_2 reduction into methane using solar irradiation: sunlight into fuel, ACS Omega 1 (2016) 868–875.
[65] H. Huang, J. Lin, G. Zhu, Y. Wen, X. Wang, X. Fu, J. Long, A long-lived mononuclear cyclopentadienyl ruthenium complex grafted onto anatase TiO_2 for efficient CO_2 photoreduction, Angew. Chem. Int. Ed. 55 (2016) 8314–8318.
[66] N. Singhal, A. Ali, A.V.C. Pendem, U. Kumar, Efficient approach for simultaneous CO and H_2 production via photoreduction of CO_2 with water over copper nanoparticles loaded TiO_2, Appl. Catal. A-Gen. 5 (2016) 107–117.
[67] K. Kim, A. Razzaq, S. Sorcar, Y. Park, C.A. Grimes, In Hybrid mesoporous Cu_2ZnSnS_4 (CZTS)-TiO_2 photocatalyst for efficient photocatalytic conversion of CO_2 into CH_4 under solar irradiation, RSC Adv. 6 (2016) 38964–38971.
[68] L.L. Tan, W.J. Ong, S.P. Chai, A.R. Mohamed, Visible-light-activated oxygen-rich TiO_2 as next generation photocatalyst: importance of annealing temperature on the photoactivity toward reduction of carbon dioxide, Chem. Eng. J. 283 (2015) 1254–1263.
[69] T. Zhang, J. Low, K. Koh, J. Yu, T. Asefa, Mesoporous TiO_2 comprising small, highly crystalline nanoparticles for efficient CO_2 reduction by H_2O, ACS. Sustain. Chem. Eng. J. 6 (2018) 531–540.
[70] P. Kara, S. Zeng, Y. Zhang, E. Vahidzadeh, A. Manuela, R. Kisslingera, K.M. Alama, U.K. Thakura, N. Mahdia, P. Kumara, K. Shankara, High rate CO_2 photoreduction using flame annealed TiO_2 nanotubes, Appl. Catal. B-Environ. 243 (2019) 522–536.
[71] F. Fresno, P. Reñones, E. Alfonso, C. Guillén, J.F. Trigob, J. Herrero, L. Colladoa, V.A. PeñaO'Shea, Influence of surface density on the CO2 photoreduction activity of a DC magnetron sputtered TiO2 catalyst, Appl. Catal. B-Environ. 224 (2018) 912–918.
[72] M. Dilla, N.G. Moustakas, A.E. Becerikli, T. Peppel, A. Springer, R. Schlogl, J. Strunk, S. Ristig, Judging the feasibility of TiO_2 as photocatalyst for chemical energy conversion by quantitative reactivity determinants, Phys. Chem. Chem. Phys. 21 (2019) 13144–13150.
[73] F. Rechberger, M. Niederberger, Translucent nanoparticle-based aerogel monoliths as 3-dimensional photocatalysts for the selective photoreduction of CO_2 to methanol in a continuous flow reactor, Mater. Horiz. 4 (2017) 1115–1121.
[74] A. Razzaq, A. Sinhamahapatra, T.H. Kang, C.A. Grimes, J.S. Yu, Efficient solar light photoreduction of CO_2 to hydrocarbon fuels via magnesiothermally reduced TiO_2 photocatalyst, Appl. Catal. B-Environ. 215 (2017) 28–35.
[75] M.S. Akple, J. Low, S. Liu, B. Cheng, J. Yu, W. Hob, Fabrication and enhanced CO_2 reduction performance of N-self-doped TiO_2 microsheet photocatalyst by bi-cocatalyst modification, J. CO_2 Util. 16 (2016) 442–449.
[76] D.K. Lee, J. Choi, G.H. Lee, Y.H. Kim, J.K. Kang, Energy states of a core-shell metal oxide photocatalyst enabling visible light absorption and utilization in solar-to-fuel conversion of carbon dioxide, Adv. Energy Mater. 6 (2016) 1600583.
[77] T. Billo, F.Y. Fu, P. Raghunath, I. Shown, W.F. Chen, H.T. Lien, T.H. Shen, J.F. Lee, T.S. Chan, K.Y. Huang, C. Wu, M.C. Lin, J.S. Hwang, C.H. Lee, L.C. Chen, K.H. Chen, Ni-nanocluster modified black TiO_2 with dual active sites for selective photocatalytic CO_2 reduction, Small 14 (2018) 1702928.
[78] J. Jin, J. Luo, L. Zan, T. Peng, One-pot synthesis of Cu-nanocluster-decorated Brookitetio$_2$ Quasi-nanocubes for enhanced activity and selectivity of CO_2 photoreduction to CH_4, ChemPhysChem 18 (2017) 3230–3239.
[79] T. Zhang, J. Low, X. Huang, J.F. Al-Shara, J. Yu, T. Asefa, Copper-decorated microsized nanoporous titanium dioxide photocatalysts for carbon dioxide reduction by water, ChemCatChem 9 (2017) 3054–3062.
[80] B.R. Chen, V.H. Nguyen, J.C.S. Wu, R. Martinb, K. Kocb, Production of renewable fuels by the photohydrogenation of CO_2: effect of the Cu species loaded onto TiO_2 photocatalysts, Phys. Chem. Chem. Phys. 18 (2016) 4942–4951.
[81] L. Liu, C. Zhao, J.T. Miller, Y. Li, Mechanistic study of CO_2 photoreduction with H_2O on Cu/TiO_2 nanocomposites by in Situ X-ray absorption and infrared spectroscopies, J. Phys. Chem. C 121 (2017) 490–499.
[82] T.D. Pham, B.K. Lee, Novel photocatalytic activity of Cu@V co-doped TiO_2/PU for CO_2 reduction with H_2O vapor to produce solar fuels under visible light, J. Catal. 345 (2017) 87–95.
[83] M. Cheng, S. Yang, R. Chen, X. Zhu, Q. Liao, Y. Huang, Copper-decorated TiO_2 nanorod thin films in optofluidic planar reactors for efficient photocatalytic reduction of CO_2, Int. J. Hydrog. Energy. 42 (2017) 9722–9732.
[84] M. Li, M. Wang, L. Zhu, Y. Li, Z. Yan, Z. Shen, X. Cao, Facile microwave assisted synthesis of N-rich Carbon quantum dots/dual-phase TiO_2 hetero structured nanocomposites with high activity in CO_2 photoreduction, Appl. Catal. B-Environ. 5 (2018) 269–276.
[85] H. Zhao, X. Zheng, X. Feng, Y. Li, CO_2 Reduction by plasmonic Au nanoparticle-decorated TiO_2 photocatalyst with an ultrathin Al_2O_3 interlayer, J. Phys. Chem. C 122 (2018) 18949–18956.
[86] H. Xue, T. Wang, H. Gong, H. Guo, X. Fan, B. Gao, Y. Feng, X. Meng, X. Huang, J. He, Constructing ordered three-dimensional TiO_2 channels for enhanced visible-light photocatalytic performance in CO_2 conversion induced by Au nanoparticles, Chem. Asian J. 13 (2018) 577–583.

[87] S. Sorcar, Y. Hwang, C.A. Grimes, Highly enhanced and stable activity of defect-induced titiananoparticles for solar light-driven CO_2 reduction into CH_4, Mater. Today 20 (2017) 507–515.
[88] N. Li, M. Liu, B. Yang, W. Shu, Q. Shen, M. Liu, J. Zhou, Enhanced photocatalytic performance toward CO_2 hydrogenation over nanosized TiO_2-loaded Pd under UV irradiation, J. Phys. Chem. C 121 (2017) 2923–2932.
[89] M. Tasbihi, F. Fresno, U. Simon, J. Villar-Garcí, V. PérezDieste, C. Escudero, V.A. P. Shea, On the selectivity of CO_2 photoreduction towards CH_4 using Pt/TiO_2 catalysts supported on mesoporous silica, Appl. Catal. B-Environ. 239 (2018) 68–76.
[90] S. Bera, J.E. Lee, S.B. Rawal, W.I. Lee, Size-dependent plasmonic effects of Au and $Au@SiO_2$ nanoparticles in photocatalytic CO_2 conversion reaction of Pt/TiO_2, Appl. Catal. B-Environ. 199 (2016) 55–63.
[91] X. Liu, M. Ye, S. Zhang, G. Huang, C. Li, J. Yu, P.K. Wong, S. Liu, Enhanced photocatalytic CO_2 valorization over TiO_2 hollow microspheres by synergetic surface tailoring and Au decoration, J. Mater. Chem. A 6 (2018) 24245–24255.
[92] H. Cho, W.D. Kim, J. Yu, S. Lee, D.C. Lee, Molecule-driven shape control of metal co-catalysts for selective CO_2 conversion photocatalysis, ChemCatChem 10 (2018) 5679–5688.
[93] R. Long, Y. Li, Y. Liu, S. Chen, X. Zheng, C. Gao, C. He, N. Chen, Z. Qi, L. Song, J. Jiang, J. Zhu, Y. Xiong, Isolation of Cu atoms in Pd lattice: forming highly selective sites for photocatalytic conversion of CO_2 to CH_4, J. Am. Chem. Soc. 139 (2017) 4486–4492.
[94] J. Jiao, Y. Wei, Y. Zhao, Z. Zhao, A. Duan, J. Liu, Y. Pang, J. Li, G. Jiang, Y. Wang, $AuPd/3DOM\text{-}TiO_2$ catalysts for photocatalytic reduction of CO_2: High efficient separation of photogenerated charge carriers, Appl. Catal. B-Environ. 209 (2017) 228–239.
[95] Y. Wei, X. Wu, Y. Zhao, L. Wang, Z. Zhao, X. Huang, J. Liu, J. Li, Efficient photocatalysts of TiO_2 nanocrystals-supported Pt/Ru alloy nanoparticles for CO_2 reduction with H_2O: Synergistic effect of Pt-Ru, Appl. Catal. B-Environ. 236 (2018) 445–457.
[96] M.E. Aguirre, R. Zhou, A.J. Eugene, M.I. Guzman, M.A. Grela, Cu_2O/TiO_2 heterostructures for CO_2 reduction through a direct Z-scheme: protecting Cu_2O from photocorrosion, Appl. Catal. B-Environ. 217 (2017) 485–493.
[97] K. Wu, X. Dong, J. Zhu, P. Wu, C. Liu, Y. Wang, J. Wu, J. Hou, Z. Liu, X. Guo, Designing biomimetic porous celery: TiO_2/ZnO nanocomposite for enhanced CO_2 photoreduction, J. Mater. Sci. 53 (2018) 11595–11606.
[98] Y. Lia, C. Wang, M. Song, D. Li, X. Zhang, Y. Liu, TiO_{2-x}/CoO_x photocatalyst sparkles in photothermocatalytic reduction of CO_2 with H_2O steam, Appl. Catal. B-Environ. 243 (2019) 760–770.
[99] A. Meng, L. Zhang, B. Cheng, J. Yu, TiO_2-MnO_x-Pt hybrid multiheterojunction film photocatalyst with enhanced photocatalytic CO_2-reduction activity, ACS Appl. Mater. Interfaces 11 (2019) 5581–5589.
[100] M. Cheng, S. Yang, R. Chen, X. Zhu, Q. Liao, Y. Huang, Visible light responsive CdS sensitized TiO_2 nanorod array films for efficient photocatalytic reduction of gas phase CO_2, J. Mol. Catal. A-Chem. 448 (2018) 185–194.
[101] J. Low, B. Dai, T. Tong, C. Jiang, J. Yu, In situ irradiated X-ray photoelectron spectroscopy investigation on a direct Z-scheme TiO_2/CdS composite film photocatalyst, Adv. Mater. 31 (2019) 1802981.
[102] F. Xu, J. Zhang, B. Zhu, J. Yu, J. Xu, $CuInS_2$ sensitized TiO_2 hybrid nanofibers for improved photocatalytic CO_2 reduction, Appl. Catal. B-Environ. 230 (2018) 194–202.
[103] J. Zhang, J. Fu, S. Chen, J. Lv, K. Dai, 1D carbon nanofibers@TiO_2 core-shell nanocomposites with enhanced photocatalytic activity toward CO_2 reduction, J. Alloys Compd. 746 (2018) 168–176.
[104] Y. Zhao, Y. Wei, X. Wu, H. Zheng, Z. Zhao, J. Liu, J. Li, Graphene-wrapped Pt/TiO_2 photocatalysts with enhanced photogenerated charges separation and reactant adsorption for high selective photoreduction of CO_2 to CH_4, Appl. Catal. B-Environ. 226 (2018) 360–372.
[105] A. Razzaq, C.A. Grimes, Facile fabrication of a noble metal-free photocatalyst: TiO_2 nanotube arrays covered with reduced graphene oxide, Carbon 98 (2016) 537–544.
[106] S. Sorcar, J. Thompson, Y. Hwang, Y.H. Park, T. Majima, C.A. Grimes, J.R. Durrant, High-rate solar-light photoconversion of CO_2 to fuel: controllable transformation from C_1 to C_2 products, Energy Environ. Sci. 11 (2018) 3183–3193.
[107] H. Jung, K.M. Cho, K.H. Kim, H.W. Yoo, I. Ahmed Al-Saggaf, H.T. Jung Gereige, Highly efficient and stable CO_2 reduction photocatalyst with a hierarchical structure of mesoporous TiO_2 on 3D graphene with few-layered MoS_2, ACS, Sustainable Chem. Eng. 6 (2018) 5718–5724.
[108] L.Y. Lin, Y. Nie, S. Kavadiya, T. Soundappan, P. Biswas, N-doped reduced graphene oxide promoted nano TiO_2 as a bifunctional adsorbent/photocatalyst for CO_2 photoreduction: Effect of N species, Chem. Eng. J. 316 (2017) 449–460.
[109] N. Singhal, U. Kumar, Noble metal modified TiO_2: selective photoreduction of CO_2 to hydrocarbons, Mol. Catal. 439 (2017) 91–99.
[110] Q. Guo, Q. Zhang, H. Wang, Z. Liu, C. Wang, Z. Zhao, ZnO_2-promoted ZnO as an efficient photocatalyst for the photoreduction of carbon dioxide in the presence of Water, Catal. Commun. 103 (2018) 24–28.
[111] J. Guo, K. Wang, X. Wang, Photocatalytic reduction of CO_2 with H_2O vapor under visible light over Ce doped $ZnFe_2O_4$, Catal. Sci. Technol. 7 (2017) 6013–6025.
[112] S. Zhu, S. Liang, Y. Wang, X. Zhang, F. Li, H. Lin, Z. Zhang, X. Wang, Ultrathin nanosheets of molecular sieve SAPO-5: a new photocatalyst for efficient photocatalytic reduction of CO_2 with H_2O to methane, Appl. Catal. B-Environ. 187 (2016) 11–18.
[113] J.Y. Do, Y. Im, B.S. Kwak, S.M. Park, M. Kang, Preparation of basalt fiber@perovskite $PbTiO_3$ core-shell composites and their effects on CH_4 production from CO_2 photoreduction, Ceram. Int. 42 (2016) 5942–5951.
[114] S. Liu, J. Wang, J. Yu, ZIF-8 derived bimodal carbon modified ZnO photocatalysts with enhanced photocatalytic CO_2 reduction performance, RSC Adv. 6 (2016) 59998–60006.
[115] Y. Bai, L. Ye, L. Wang, X. Shi, P. Wang, W. Bai, A dual-cocatalyst-loaded $Au/BiOI/MnO_x$ system for enhanced photocatalytic greenhouse gas conversion into solar fuels, Environ. Sci. Nano 3 (2016) 902–909.
[116] C. Xin, M. Hu, K. Wang, X. Wang, Significant enhancement of photocatalytic reduction of CO_2 with H_2O over ZnO by the formation of basic zinc carbonate, Langmuir 33 (2017) 6667–6676.
[117] N. Nie, F. He, L. Zhang, B. Cheng, Direct Z-scheme PDA-modified ZnO hierarchical microspheres with enhanced photocatalytic CO_2 reduction performance, Appl. Surf. Sci. 457 (2018) 1096–1102.
[118] S. Yan, Y. Yu, Y. Cao, Synthesis of porous $ZnMn_2O_4$ flower-like microspheres by using MOF as precursors and its application on photoreduction of CO_2 into CO, Appl. Surf. Sci. 465 (2019) 383–388.
[119] M. Tahir, Hierarchical 3D VO_2/ZnV_2O_4 microspheres as an excellent visible light photocatalyst for CO_2 reduction to solar fuels, Appl. Surf. Sci. 467 (2019) 1170–1180.
[120] J. Jin, S. Chen, J. Wang, C. Chen, T. Peng, $SrCO_3$-modified brookite/anatase TiO_2 heterophase junctions with enhanced activity and selectivity of CO_2 photoreduction to CH_4, Appl. Surf. Sci. 476 (2019) 937–947.
[121] Y. Wang, M. Liu, W. Chen, L. Mao, W. Shang, Ag loaded on layered perovskite $H_2SrTa_2O_7$ to enhance the selectivity of photocatalytic CO_2 reduction with H_2O, J. Alloys Compd. 786 (2019) 149–154.
[122] S. Zhu, S. Liang, J. Bi, M. Liu, L. Zhou, L. Wu, X. Wang, Photocatalytic reduction of CO_2 with H_2O to CH_4 over ultrathin $SnNb_2O_6$ 2D nanosheets under visible light irradiation, Green Chem. 18 (2016) 1355–1363.
[123] L.B. Hoch, L. He, Q. Qiao, K. Liao, L.M. Reyes, Y. Zhu, G.A. Ozin, Effect of precursor selection on the photocatalytic performance of -indium oxide nanomaterials for gas-phase CO_2 reduction, Chem. Mater. 28 (2016) 4160–4168.
[124] T. Yan, L. Wang, Y. Liang, M. Makaremi, T.E. Wood, Y. Dai, B. Huang, A.A. Jelle, Y. Dong, G.A. Ozin, Polymorph selection towards photocatalytic gaseous CO_2 hydrogenation, Nat. Commun. 10 (2019) 2521–2531.
[125] K.H. Kim, S. Kim, B.C. Moon, J.W. Choi, H.M. Jeong, Y. Kwon, S. Kwon, H.S. Choib, J.K. Kang, Quadruple metal-based layered structure as the photocatalyst for conversion of carbon dioxide into a value added carbon monoxide with high selectivity and efficiency, J. Mater. Chem. A 5 (2017) 8274–8279.
[126] L. Wang, D.W. Bahnemann, L. Bian, G. Dong, J. Zhao, C. Wang, Two-dimensional layered zinc silicate nanosheets with excellent photocatalytic performance for organic pollutant degradation and CO_2 conversion, Angew. Chem. Int. Ed. 58 (2019) 8103–8108.
[127] J. Li, Y. Ye, L. Ye, F. Su, Z. Ma, J. Huang, H. Xie, D.E. Doronkin, A. Zimina, J.D. Grunwaldt, Y. Zhou, Sunlight induced photo-thermal synergistic catalytic CO_2 conversion via localized surface plasmon resonance of MoO_3x, J. Mater. Chem. A 7 (2019) 2821–2830.
[128] X. Wang, L. Lu, B. Wang, Z. Xu, Z. Xin, S. Yan, Z. Geng, Z. Zou, Frustrated Lewis Pairs accelerating CO_2 reduction on oxyhydroxide photocatalysts with surface lattice hydroxyls as a solid-state proton donor, Adv. Funct. Mater. 28 (2018) 1804191.
[129] J. Liang, L. Li, Synthesis of N-doped graphene-functionalized $Zn_{1.231}Ge_{0.689}N_{1.218}O_{0.782}$ solid solution as a photocatalyst for CO_2 reduction and oxidation of benzyl alcohol under visible-light irradiation, J. Mater. Chem. A 5 (2017) 10998–11008.
[130] D. Mateo, J. Albero, H. Garcı, Photoassisted methanation using Cu_2O nanoparticles supported on graphene as a photocatalyst, Energy Environ. Sci. 10 (2017) 2392–2400.
[131] D. Mateo, J. Albero, H. García, Graphene supported NiO/Ni nanoparticles as efficient photocatalyst for gas phase CO_2 reduction with hydrogen, Appl. Catal. B-Environ. 224 (2018) 563–571.
[132] Y. Jiang, J.F. Liao, H.Y. Chen, H.H. Zhang, J.Y. Li, X.D. Wang, D.B. Kuang, All-Solid-state Z-scheme $a\text{-}Fe_2O_3$/amine-RGO/CsPbBr 3 hybrids for visible-light-driven photocatalytic C_O2 reduction, Chem 6 (2020) 766–780.
[133] Y. Liang, W. Wu, P. Wang, S.C. Liou, D. Liu, S.H. Ehrman, Scalable fabrication of SnO_2/eo-GO nanocomposites for the photoreduction of CO_2 to CH_4, Nano Res. 11 (2018) 4049–4061.
[134] D. Li, S. Ouyang, H. Xu, D. Lu, M. Zhao, X. Zhang, J. Ye, Synergistic effect of Au and Rh on $SrTiO_3$ in significantly promoting visible-light-driven syngas production from CO_2 and H_2O, Chem. Commun. 52 (2016) 5989–5992.
[135] Y. Chai, L. Li, J. Lu, D. Li, J. Shen, Y. Zhang, J. Liang, X. Wang, Germanium-substituted Zn_2TiO_4 solid solution photocatalyst for conversion of CO_2 into fuels, J. Catal. 371 (2019) 144–152.
[136] M. Wang, M. Shen, X. Jin, J. Tian, M. Li, Y. Zhou, L. Zhang, Y. Li, J. Shi, Oxygen vacancy generation and stabilization in CeO_{2-x} by Cu introduction with improved CO_2 photocatalytic reduction, activity, ACS Catal. 9 (2019) 4573–4581.
[137] Y. Wang, X. Bai, F. Wang, S. Kang, C. Yin, X. Li, Nanocasting synthesis of chromium doped mesoporous CeO_2 with enhanced visible-light photocatalytic CO_2 reduction performance, J. Hazard. Mater. 372 (2019) 69–76.
[138] J. Ding, X. Liu, M. Shi, T. Li, M. Xia, X. Du, R. Shang, H. Gu, Q. Zhong, Single-atom silver-manganese catalysts for photocatalytic CO_2 reduction with H_2O to CH_4, Sol. Energ. Mat. Sol. C. 195 (2019) 34–42.

[139] P. Zhou, X. Wang, S. Yan, Z. Zou, Solid solution photocatalyst with spontaneous polarization exhibiting low recombination toward efficient CO_2 photoreduction, ChemSusChem 9 (2016) 2064–2068.

[140] M.M. Kandy, V.G. Gaikar, Enhanced photocatalytic reduction of CO_2 using CdS/Mn_2O_3 nanocomposite photocatalysts on porous anodic alumina support with solar concentrators, Renewable Energy 139 (2019) 915–923.

[141] L. Lu, B. Wang, S. Wang, Z. Shi, S. Yan, Z. Zou, La_2O_3-modified $LaTiO_2N$ photocatalyst with spatially separated active sites achieving enhanced CO_2 reduction, Adv. Funct. Mater. 27 (2017) 1702447.

[142] L. Lu, S. Wang, C. Zhou, Z. Shi, H. Zhu, Z. Xin, X. Wang, S. Yan, Z. Zou, Surface chemistry imposes selective reduction of CO_2 to CO over $Ta_3N_5/LaTiO_2N$ photocatalyst, J. Mater. Chem. A 6 (2018) 14838–14846.

[143] L. Lu, Z. Xin, X. Wang, S. Wang, H. Zhu, T. Li, Y. Gu, S. Yan, Z. Zou, KOH-modified $Ni/LaTiO_2N$ Schottky junction efficiently reducing CO_2 to CH_4 under visible light irradiation, Appl. Catal. B-Environ. 244 (2019) 786–794.

[144] M.M. Kandy, V.G. Gaikar, Continuous photocatalytic reduction of CO_2 using nanoporous reduced graphene oxide (RGO)/cadmium sulfide (CdS) as catalyst on porous anodic alumina (PAA)/aluminum support, J. Nanosci. Nanotechnol. 19 (2019) 5323–5331.

[145] X. Liu, B. Liu, L. Li, Z. Zhu, P. Chen, C. Li, Y. Gong, L. Niu, J. Liu, L. Lei, C.Q. Sund, $Cu_2In_2ZnS_5/Gd_2O_2S$: Tb for full solar spectrum photoreduction of Cr(VI) and C_O2 from UV/vis to near-infrared light, Appl. Catal. B-Environ. 249 (2019) 82–90.

[146] C. Zeng, H. Huang, T. Zhang, F. Dong, Y. Zhang, Y. Hu, Fabrication of heterogeneous-phase solid-solution promoting band structure and charge separation for enhancing photocatalytic CO_2 reduction: a case of $Zn_XCa_{1-X}In_2S_4$, ACS Appl. Mater. Interfaces 9 (2017) 27773–27783.

[147] X. Jiao, X. Li, X. Jin, Y. Sun, J. Xu, L. Liang, H. Ju, J. Zhu, Y. Pan, W. Yan, Y. Lin, Y. Xie, Partially oxidized SnS_2 atomic layers achieving efficient visible-light-driven CO_2 reduction, J. Am. Chem. Soc. 139 (2017) 18044–18051.

[148] M. Zubair, A. Razzaq, C.A. Grimesc, Cu_2ZnSnS_4 (CZTS)-ZnO: a noble metal-free hybrid Z-scheme photocatalyst for enhanced solar-spectrum photocatalytic conversion of CO_2 to CH_4, J CO_2 Util. 20 (2017) 301–311.

[149] K.M. Cho, K.H. Kim, K. Park, C. Kim, S. Kim, A.A. Saggaf, I. Gereige, H.T. Jung, Amine-functionalized graphene/CdS composite for photocatalytic reduction of CO_2, ACS Catal. 7 (2017) 7064–7069.

[150] Y. Huo, J. Zhang, K. Dai, Q. Li, J. Lv, G. Zhu, C. Liang, All-solid-state artificial Z-scheme porous $g\text{-}C_3N_4/Sn_2S_3$-DETA heterostructure photocatalyst with enhanced performance in photocatalytic CO_2 reduction, Appl. Catal. B-Environ. 241 (2019) 528–538.

[151] T.D.C. Nguyen, T.P.L.C. Nguyen, H.T.T. Mai, V.D. Dao, M.P. Nguyen, V.N. Nguyen, Novel photocatalytic conversion of CO_2 by vanadium-doped tantalum nitride for valuable solar fuel production, J. Catal. 352 (2017) 67–74.

[152] S. Wang, Y. Guan, L. Lu, Z. Shi, S. Yan, Z. Zou, Effective separation and transfer of carriers into the redox sites on Ta_3N_5/Bi photocatalyst for promoting conversion of CO_2 into CH_4, Appl. Catal. B-Environ. 224 (2018) 10–16.

[153] C.Y. Hu, J. Zhou, C.Y. Sun, M. Chen, X.L. Wang, Z.M. Su, HKUST-1 derived hollow $C\text{-}Cu_2O@xS$ nanotube/$g\text{-}C_3N_4$ composites for visible-light CO_2 photoreduction with H_2O vapor, Chem. Eur. J. 25 (2019) 379–385.

[154] H. Wang, Z. Sun, Q. Li, Q. Tang, Z. Wu, Surprisingly advanced CO_2 photocatalytic conversion over thiourea derived $g\text{-}C_3N_4$ with water vapor while introducing 200–420 nm UV light, J. CO_2 Util. 14 (2016) 143–151.

[155] Y. Wan, Y. Xu, Y. Wang, H. Qin, X. Li, Y. Zuo, S. Kang, L. Cui, Synthesis of Mo-doped graphitic carbon nitride catalysts and their photocatalytic activity in the reduction of CO_2 with H_2O, Catal. Commun. 74 (2016) 75–79.

[156] Q. Lang, W. Hu, P. Zhou, T. Huang, S. Zhon, L. Yang, J. Chen, S. Bai, Twin defects engineered Pd cocatalyst on C_3N_4 nanosheets for enhanced photocatalytic performance in CO_2 reduction reaction, Nanotechnology. 28 (2017) 484003.

[157] Z. Sun, S. Wang, Q. Li, M. Lyu, T. Butburee, B. Luo, H. Wang, J.M.T.A. Fischer, C. Zhang, Z. Wu, L. Wang, Enriching CO_2 activation sites on graphitic carbon nitride with simultaneous introduction of electron-transfer promoters for superior photocatalytic CO_2-to-fuel conversion, Adv. Sustainable Syst. 1 (2017) 1700003.

[158] F.R. Pomilla, M.A.L.R.M. Cortes, J.W.J. Hamilton, R. Molinari, G. Barbieri, G. Marcì, L. Palmisano, P.K. Sharma, A. Brown, J.A. Byrne, An investigation into the stability of graphitic C_3N_4 as a photocatalyst for CO_2 reduction, J. Phys. Chem. C 122 (2018) 28727–28738.

[159] Q. Li, Z. Sun, H. Wang, Z. Wu, Insight into the enhanced CO_2 photocatalytic reduction performance over hollow-structured Bi-decorated $g\text{-}C_3N_4$ nanohybrid under visible-light irradiation, J. CO_2 Util. 28 (2018) 126–136.

[160] J. Fu, B. Zhu, C. Jiang, B. Cheng, W. You, J. Yu, Hierarchical porous O-doped $g\text{-}C_3N_4$ with enhanced photocatalytic CO_2 reduction activity, Small 13 (2017) 1603938.

[161] L. Ye, D. Wu, K.H. Chu, B. Wang, H. Xie, H.Y. Yip, P.K. Wong, Phosphorylation of $g\text{-}C_3N_4$ for enhanced photocatalytic CO_2 reduction, Chem. Eng. J. 304 (2016) 376–383.

[162] P. Xia, B. Zhu, J. Yu, S. Cao, M. Jaroniec, Ultra-thin nanosheet assemblies of graphitic carbon nitride for enhanced photocatalytic CO_2 reduction, J. Mater. Chem. A 5 (2017) 3230–3238.

[163] H. Li, Y. Gao, Z. Xiong, C. Liao, K. Shih, Enhanced selective photocatalytic reduction of CO_2 to CH_4 over plasmonic Au modified $g\text{-}C_3N_4$ photocatalyst under UV-vis light irradiation, Appl. Surf. Sci. 439 (2018) 552–559.

[164] H. Li, Y. Gao, X. Wu, P.H. Lee, K. Shi, Fabrication of heterostructured $g\text{-}C_3N_4/Ag\text{-}TiO_2$ Hybrid photocatalyst with enhanced performance in photocatalytic conversion of CO_2 under simulated sunlight irradiation, Appl. Surf. Sci. 402 (2017) 198–207.

[165] N.T.T. Truc, L.G. Bach, N.T. Hanh, T.D. Pham, N.T.P.L. Chi, D.T. Tran, M.V. Nguyen, V.N. Nguyen, The superior photocatalytic activity of Nb doped $TiO_2/g\text{-}C_3N_4$ direct Zscheme system for efficient conversion of CO_2 into valuable fuels, J. Colloid Interface Sci. 540 (2019) 1–8.

[166] K. Li, B. Peng, J. Jin, L. Zan, T. Peng, Carbon nitride nanodots decorated brookite TiO_2 quasi nanocubes for enhanced activity and selectivity of visible-light-driven CO_2 reduction, Appl. Catal. B-Environ. 203 (2017) 910–916.

[167] J. Zhou, H. Wu, C.Y. Sun, C.Y. Hu, X.L. Wang, Z.H. Kang, Z.M. Su, Ultrasmall $C\text{-}TiO_{2x}$ nanoparticle/$g\text{-}C_3N_4$ composite for CO_2 photoreduction with high efficiency and selectivity, J. Mater. Chem. A 6 (2018) 21596–21604.

[168] M. Li, L. Zhang, M. Wu, Y. Du, X. Fan, M. Wang, L. Zhang, Q. Kong, J. Shi, Mesostructured $CeO_2/g\text{-}C_3N_4$ nanocomposites: remarkably enhanced photocatalytic activity for C_O2 reduction by mutual component activations, Nano Energy 19 (2016) 145–155.

[169] M. Li, L. Zhang, X. Fan, M. Wu, M. Wang, R. Cheng, L. Zhang, H. Yao, J. Shi, Core-shell $LaPO_4/g\text{-}C_3N_4$ nanowires for highly active and selective CO_2 reduction, Appl. Catal. B-Environ. 201 (2017) 629–635.

[170] M. Wang, M. Shen, L. Zhang, J. Tian, X. Jin, Y. Zhou, J. Shi, 2D–2D $MnO_2/g\text{-}C_3N_4$ heterojunction photocatalyst: in-situ synthesis and enhanced CO_2 reduction activity, Carbon 120 (2017) 23–31.

[171] D. Xu, B. Cheng, W. Wang, C. Jiang, J. Yu, $Ag_2CrO_4/g\text{-}C_3N_4$/graphene oxide ternary nanocomposite Z-scheme photocatalyst with enhanced CO_2 reduction activity, Appl. Catal. B-Environ. 231 (2018) 368–380.

[172] T. Di, B. Zhu, B. Cheng, J. Yu, J. Xu, A direct Z-scheme $g\text{-}C_3N_4/SnS_2$ photocatalyst with superior visible-light CO_2 reduction performance, J. Catal. 352 (2017) 532–541.

[173] M. Liang, T. Borjigin, Y. Zhang, H. Liu, B. Liu, H. Guo, Z-Scheme Au@Void@$g\text{-}C_3N_4$/SnS yolk−shell heterostructures for superior photocatalytic CO_2 reduction under visible light, ACS Appl. Mater. Interfaces 1040 (2018) 34123–34131.

[174] X. Zhang, L. Wang, Q. Du, Z. Wang, S. Ma, M. Yu, Photocatalytic CO_2 reduction over B_4C/C_3N_4 with internal electric field under visible light irradiation, J. Colloid Interface Sci. 464 (2016) 89–95.

[175] R. Zhang, Z. Huang, C. Li, Y. Zuo, Y. Zhou, Monolithic $g\text{-}C_3N_4$/reduced graphene oxide aerogel with in situ embedding of Pd nanoparticles for hydrogenation of CO_2 to CH_4, Appl. Surf. Sci. 475 (2019) 953–960.

[176] Y. Wang, X. Bai, H. Qin, F. Wang, Y. Li, X.L. Shi, F. Kang, Y. Zuo, L. Cui, Facile one-step synthesis of hybrid graphitic carbon nitride and carbon composites as high-performance catalysts for CO_2 photocatalytic conversion, ACS Appl. Mater. Interfaces 8 (2016) 17212–17219.

[177] Y. Wang, Q. Xia, X. Bai, Z. Ge, Q. Yang, C. Yin, S. Kang, M. Dong, X. Li, Carbothermal activation synthesis of 3D porous $g\text{-}C_3N_4$/carbon nanosheets composite with superior performance for CO_2 photoreduction, Appl. Catal. B-Environ. 239 (2018) 196–203.

[178] W.J. Ong, L.K. Putri, Y.C. Tan, L.L. Tan, N. Li, Y.H. Ng, X. Wen, S. Chai, Unravelling charge carrier dynamics in protonated $g\text{-}C_3N_4$ interfaced with carbon nanodots as co-catalysts toward enhanced photocatalytic CO_2 reduction: a combined experimental and first-principles DFT study, Nano Res. 10 (2017) 1673–1696.

[179] H. Feng, Q. Guo, Y. Xu, T. Chen, Y. Zhou, Y. Wang, M. Wang, D. Shen, Surface nonpolarization of $g\text{-}C_3N_4$ by decoration with sensitized quantum dots for improved CO_2 photoreduction, ChemSusChem 11 (2018) 4256–4261.

[180] F.R. Pomilla, A. Brunetti, G. Marcì, E.I.G.L. pez,· E. Fontananova, L. Palmisano, G. Barbieri, CO2 to Liquid Fuels: Photocatalytic Conversion in a Continuous Membrane Reactor, ACS Sustainable Chem. Eng. 6 (2018) 8743–8753.

[181] Y. Wang, T. Li, Y. Yao, X. Li, X. Bai, C. Yin, N. Williams, S. Kang, L. Cui, L. Hu, Dramatic enhancement of CO_2 photoreduction by biodegradable light-management paper, Adv. Energy Mater. 8 (2018) 1703136.

[182] L. Ye, X. Jin, C. Liu, C. Ding, H. Xie, K.H. Chu, P.K. Wong, Thickness-ultrathin and Bismuth-rich strategies for BiOBr to enhance photoreduction of CO_2 into solar fuels, Appl. Catal. B-Environ. 187 (2016) 281–290.

[183] X.Y. Kong, W.P.C. Lee, W.J. Ong, S.P. Chai, A.R. Mohamed, Oxygen-deficient BiOBr as a highly stable photocatalyst for efficient CO_2 reduction into renewable carbon-neutral fuels, ChemCatChem 8 (2016) 3074–3081.

[184] X. Jin, C. Lv, X. Zhou, L. Ye, H. Xie, Y. Liu, H. Su, B. Zhang, G. Chen, Oxygen vacancy engineering of $Bi_{24}O_{31}Cl_{10}$ for boosted photocatalytic CO_2 conversion, ChemSusChem 12 (2019) 1–9.

[185] H. Yu, J. Li, Y. Zhang, S. Yang, K. Han, F. Dong, T. Ma, H. Huang, Three-in-one oxygen vacancy: whole visible-spectrum absorption, efficient charge separation and surface site activation for robust CO_2 photoreduction, Angew. Chem. Int. Ed. 58 (2019) 3880–3884.

[186] X.J. Ren, M.C. Gao, Y.F. Zhang, Z.Z. Zhang, X.Z. Cao, B.Y. Wang, X.X. Wang, Photocatalytic reduction of CO_2 on BiOX: Effect of halogen element type and surface oxygen vacancy mediated mechanism, Appl. Catal. B-Environ. 274 (2020) 119063–119069.

[187] J. Wang, H.C. Yao, Z.Y. Fan, L. Zhang, J. Wang, S.Q. Zang, Z. Li, Indirect Z-scheme $BiOI/g\text{-}C_3N_4$ photocatalysts with enhanced photoreduction CO_2 activity under visible light irradiation, ACS Appl. Mater. Interfaces 8 (2016) 3765–3775.

[188] Y. Bai, L. Ye, L. Wang, X. Shi, P. Wang, W. Bai, P.K. Wong, $g\text{-}C_3N_4/Bi_4O_5I_2$ Heterojunction with I_3^-/I^- redox mediator for enhanced photocatalytic CO_2 conversion, Appl. Catal. B-Environ. 194 (2016) 98–104.

[189] Z.H. Wei, Y.F. Wang, Y.Y. Li, L. Zhang, H.C. Yao, Z.J. Li, Enhanced photocatalytic CO_2 reduction activity of Z-scheme CdS/$BiVO_4$ nanocomposite with thinner $BiVO_4$ nanosheets, J. CO_2 Util. 28 (2018) 15–25.
[190] X.Y. Kong, W.L. Tan, B.J. Ng, S.P. Chai, A.R. Mohamed, Harnessing Vis-NIR broad spectrum for photocatalytic CO_2 reduction over carbon quantum dots-decorated ultrathin Bi_2WO_6 nanosheets, Nano Res. 10 (2017) 1720–1731.
[191] L. Hao, L. Kang, H. Huang, L. Ye, K. Han, S. Yang, H. Yu, M. Batmunkh, Yi. Zhang, T. Ma, Surface-halogenation-induced atomic-site activation and local charge separation for superb CO2 photoreduction, Adv. Mater. 31 (2019) 1900546.
[192] S. Wan, M. Ou, Q. Zhong, X. Wang, Perovskite-type CsPbBr 3 quantum dots/UiO-66(N_H2) nanojunction as efficient visible-light-driven photocatalyst for C_O2 reduction, Chem. Eng. J. 358 (2019) 1287–1295.
[193] N. Sadeghi, S. Sharifnia, M.S. Arabi, A porphyrin-based metal organic framework for high rate photoreduction of CO_2 to CH_4 in gas phase, J. CO_2 Util. 16 (2016) 450–457.
[194] Z.B. Fang, T.T. Liu, J.X. Liu, S.Y. Jin, X.P. Wu, X.Q. Gong, K. Wang, Q. Yin, T.F. Liu, Rong Cao, H.C. Zhou, Boosting interfacial charge-transfer kinetics for efficient overall CO_2 photoreduction via rational design of coordination spheres on metal-organic frameworks, J. Am. Chem. Soc. 142 (2020) 12515–12523.
[195] S. Liu, F. Chen, S. Li, X. Peng, Y. Xiong, Enhanced photocatalytic conversion of greenhouse gas CO_2 into solar fuels over g-C_3N_4 nanotubes with decorated transparent ZIF-8 nanoclusters, Appl. Catal. B-Environ. 211 (2017) 1–10.
[196] Z.C. Kong, J.F. Liao, Y.J. Dong, Y.F. Xu, H.Y. Chen, D.B. Kuang, C.Y. Su, Core@Shell CsPbBr 3@Zeolitic imidazolate framework nanocomposite for efficient photocatalytic C_O2 reduction, ACS Energy Lett. 3 (2018) 2656–2662.
[197] R. Li, J. Hu, M. Deng, H. Wang, X. Wang, Y. Hu, H.L. Jiang, J. Jiang, Q. Zhang, Y. Xie, Y. Xiong, Integration of an inorganic semiconductor with a metal-organic framework: a platform for enhanced gaseous photocatalytic reactions, Adv. Mater. 26 (2014) 4783–4788.
[198] X. He, Z. Gan, S. Fisenko, D. Wang, H.M. El-Kaderi, W.N. Wang, Rapid formation of metal-organic frameworks (MOFs) based nanocomposites in microdroplets and their applications for CO_2 photoreduction, ACS Appl. Mater. Interfaces 9 (2017) 9688–9698.
[199] Y.J. Ma, Q. Tang, W.Y. Sun, Z.Y. Yao, W.H. Zhu, T. Li, J.Y. Wang, Assembling ultrafine TiO_2 nanoparticles on UiO-66 octahedrons to promote selective photocatalytic conversion of CO_2 to CH_4 at a low concentration, Appl. Catal. B-Environ. 270 (2020) 118856–118864.
[200] X. Chen, Q. Li, J. Li, J. Chen, H. Jia, Modulating charge separation via in situ hydrothermal assembly of low content Bi_2S_3 into UiO-66 for efficient photothermocatalytic CO_2 reduction, Appl. Catal. B-Environ. 270 (2020) 118915–118919.
[201] N. Li, X.C. Liu, J.J. Zhou, W.S. Chen, M.C. Liu, Encapsulating CuO quantum dots in MIL-125(Ti) coupled with g-C_3N_4 for efficient photocatalytic CO_2 reduction, Chem. Eng. J. 399 (2020) 125782–125789.
[202] S.M. Liu, Z. Zhang, X. Li, H. Jia, M. Ren, S. Liu, Ti-substituted Keggin-type polyoxotungstate as proton and electron reservoir encaged into metal-organic framework for carbon dioxide photoreduction, Adv. Mater. 5 (2018) 1801062.
[203] M. Wang, D. Wang, Z. Li, Self-assembly of CPO-27-Mg/TiO_2 nanocomposite with enhanced performance for photocatalytic CO_2 reduction, Appl. Catal. B-Environ. 183 (2016) 47–52.
[204] K. Khaletskaya, A. Pougin, R. Medishetty, C. Rösler, C. Wiktor, J. Strunk, R.A. Fischer, Fabrication of gold/titania photocatalyst for CO_2 reduction based on pyrolytic conversion of the metal-organic framework NH_2-MIL-125(Ti) loaded with gold nanoparticles, Chem. Mater. 2721 (2015) 7248–7257.
[205] X. Feng, F. Pan, H. Zhao, W. Deng, P. Zhang, H.C. Zhou, Y. Li, Atomic layer deposition enabled MgO surface coating on porous TiO_2 for improved CO_2 photoreduction, Appl. Catal. B-Environ. 238 (2018) 274–283.
[206] S. Chen, J. Yu, J. Zhang, Enhanced photocatalytic CO_2 reduction activity of MOF-derived ZnO/NiO porous hollow spheres, J. CO_2 Util. 24 (2018) 548–554.
[207] J. Ding, Y. Bu, M. Ou, Y. Yu, Q. Zhong, M. Fan, Facile decoration of carbon fibers with Ag nanoparticles for adsorption and photocatalytic reduction of CO_2, Appl. Catal. B-Environ. 202 (2017) 314–325.
[208] Y. Wang, L. Zhang, X. Zhang, Z. Zhang, Y. Tong, F. Li, J.C.S. Wu, X. Wang, Openmouthed-SiC hollow-sphere with highly photocatalytic activity for reduction of CO_2 with H_2O, Appl. Catal. B-Environ. 206 (2017) 158–167.
[209] D. Yan, J. Liu, X. Fu, P. Liu, H. Luo, Low-temperature synthesis of mesoporous boron carbides as metal-free photocatalysts for enhanced CO_2 reduction and generation of hydroxyl radicals, J. Mater. Sci. 54 (2019) 6151–6163.
[210] L.J. Wang, R.L. Wang, X. Zhang, J.L. Mu, Z.Y. Zhou, Z.M. Su, Improved photoreduction of CO_2 with water by tuning the valence band of covalent organic frameworks, ChemSusChem 13 (2020) 2973–2980.
[211] M. Zhang, M. Lu, Z.L. Lang, J. Liu, M. Liu, J.N. Chang, L.Y. Li, L.J. Shang, M. Wang, S.L. Li, Y.Q. La, Semiconductor/covalent-organic-framework Z-scheme heterojunctions for artificial photosynthesis, Angew. Chem. Int. Ed. 59 (2020) 6500–6506.
[212] K. Lei, D. Wang, M.P. Kou, Z.Y. Ma, L. Wang, L.Q. Ye, Y. Kong, A Metal-free donor-acceptor covalent organic framework photocatalyst for visible-light-driven reduction of CO_2 with H_2O, ChemSusChem 13 (2020) 1725–1729.
[213] W. Yuan, L. Cheng, Y. An, S. Lv, H. Wu, X. Fan, Y. Zhang, X. Guo, J. Tang, Laminated hybrid junction of sulfur-doped TiO_2 and a carbon substrate derived from Ti_3C_2 MXenes: toward highly visible light-driven photocatalytic hydrogen evolution, Adv. Sci. 5 (2018) 1700870.
[214] M. Ge, C. Cao, J. Huang, S. Li, Z. Chen, K. Zhang, S.S.A. Deyabd, Y. Lai, A review of one-dimensional TiO_2 nanostructured materials for environmental and energy applications, J. Mater. Chem. A 4 (2016) 6772–6801.
[215] L. Yuan, K.Q. Lu, F. Zhang, X. Fu, Y.J. Xu, Unveiling the interplay between light-driven CO_2 photocatalytic reduction and carbonaceous residues decomposition: a case study of Bi_2WO_6-TiO_2 binanosheets, Appl. Catal. B-Environ. 237 (2018) 424–431.
[216] A. Narita, X.Y. Wang, X.L. Feng, K. Mullen, New advances in nanographene chemistry, Chem. Soc. Rev. 44 (2015) 6616–6643.
[217] K.S. Novoselov, A.K. Geim, S.V. Morozov, D. Jiang, Y. Zhang, S.V. Dubonos, L.V. Grigorieva, A.A. Firsov, Electric field effect in atomically thin carbon films, Science 306 (2004) 666–669.
[218] P. Kumar, B. Sain, S.L. Jain, Photocatalytic reduction of carbon dioxide to methanol using a ruthenium trinuclear polyazine complex immobilized on graphene oxide under visible light irradiation, J. Mater. Chem. A 2 (2014) 11246–11253.
[219] W.G. Tu, Y. Zhou, Z.G. Zou, Photocatalytic conversion of CO_2 into renewable hydrocarbon fuels: state-of-the-art accomplishment, challenges, and prospects, Adv. Mater. 26 (2014) 4607–4626.
[220] X. Wang, K. Maeda, X. Chen, K. Takanabe, K. Domen, Y. Hou, X. Fu, M. Antonietti, Polymer semiconductors for artificial photosynthesis: hydrogen evolution by mesoporous graphitic carbon nitride with visible light, J. Am. Chem. Soc. 131 (2009) 1680–1681.
[221] X.C. Wang, K. Maeda, A. Thomas, K. Takanabe, G. Xin, J.M. Carlsson, K. Domen, M. Antonietti, A metal-free polymeric photocatalyst for hydrogen production from water under visible light, Nat. Mater. 8 (2009) 76–80.
[222] L. Jiang, M. Yao, B. Liu, Q. Li, R. Liu, H. Lv, S. Lu, C. Gong, B. Zou, T. Cui, B. Liu, Controlled synthesis of CeO_2/graphene nanocomposites with highly enhanced optical and catalytic properties, J. Phys. Chem. C 116 (2012) 11741–11745.
[223] M. Lei, Z.B. Wang, J.S. Li, H.L. Tang, W.J. Liu, Y.G. Wang, CeO_2 nanocubes-graphene oxide as durable and highly active catalyst support for proton exchange membrane fuel cell, Sci. Rep. 4 (2014) 7415–7420.
[224] B. Pan, S. Luo, W. Su, X. Wang, Photocatalytic CO_2 reduction with H_2O over $LaPO_4$ nanorods deposited with Pt cocatalyst, Appl. Catal. B-Environ. 168 (2015) 458–464.
[225] H. Yu, R. Shi, Y. Zhao, G.I.N. Waterhouse, L.Z. Wu, C.H. Tung, T. Zhang, Smart utilization of carbon dots in semiconductor photocatalysis, Adv. Mater. 28 (2016) 9454–9477.
[226] L. Ye, Y. Su, X. Jin, H. Xie, C. Zhang, Recent advances in BiO_X (X = Cl, Br and I) photocatalysts: synthesis, modification, facet effects and mechanisms, Environ. Sci. Nano 1 (2014) 90–112.
[227] H. Cheng, B. Huang, Y. Dai, Engineering BiO_X (X = Cl, Br, I) nanostructures for highly efficient photocatalytic applications, Nanoscale 6 (2014) 2009–2026.
[228] H. Li, J. Li, Z. Ai, F. Jia, L. Zhang, Oxygen vacancy-mediated photocatalysis of BiOCl: reactivity, selectivity and perspective, Angew. Chem. Int. Ed. 57 (2018) 122–138.
[229] J. Li, Y. Yu, L. Zhang, Bismuth oxyhalide nanomaterials: layered structures meet photocatalysis, Nanoscale. 6 (2014) 8473–8488.
[230] R. He, D. Xu, B. Cheng, J. Yu, W. Ho, Review on nanoscale Bi-based photocatalysts, Nanoscale Horiz. 3 (2018) 464–504.
[231] J. Di, J. Xia, H. Li, S. Guo, S. Dai, Bismuth oxyhalide layered materials for energy and environmental applications, Nano Energy 41 (2017) 172–192.
[232] X. Jin, L. Ye, H. Xie, G. Chen, Bismuth-rich bismuth oxyhalides for environmental and energy photocatalysis, Coord. Chem. Rev. 349 (2017) 84–101.